

**On the long pulse operation  
of a discharge pumped  
ArF excimer laser**

CIP-gegevens Koninklijke Bibliotheek, Den Haag, Nederland

Feenstra, Louw

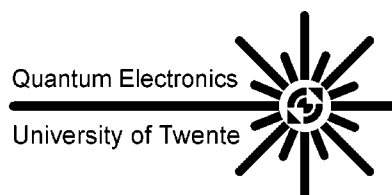
On the long pulse operation of a discharge pumped ArF excimer laser

Proefschrift Universiteit Twente, Enschede, Nederland

Met literatuuropgave en Nederlandse samenvatting

ISBN: 90-365 133 83

Trefwoorden: lasers, gasontladingen, ultraviolet, röntgenstraling



© 1999 L. Feenstra

The work described in this thesis was performed in the Quantum Electronics group of the faculty of Applied Physics of the University of Twente, P.O. Box 217, 7500 AE Enschede, the Netherlands, as a part of the research programme of the Netherlands Technology Foundation (STW).



**ON THE LONG PULSE OPERATION  
OF A DISCHARGE PUMPED  
ArF EXCIMER LASER**

**PROEFSCHRIFT**

ter verkrijging van  
de graad van doctor aan de Universiteit Twente,  
op gezag van de rector magnificus,  
prof. dr. F.A. van Vught,  
volgens besluit van het College voor Promoties  
in het openbaar te verdedigen  
op vrijdag 10 september 1999  
te 13:15 uur.

door  
**Louw Feenstra**  
geboren op 2 december 1970  
te Groningen

*Dit proefschrift is goedgekeurd door de promotor,*  
prof. dr ir W.J. Witteman  
*en de assistent promotor,*  
dr P.J.M. Peters

*Voor mijn ouders  
Aan Ermioni*

Hierbij bedank ik iedereen die, op welke wijze ook,  
heeft bijgedragen aan het onderzoek  
en het tot stand komen van dit proefschrift.

# Contents

<b>1</b>	<b>Introduction</b>	<b>1</b>
1.1	Structure of this thesis . . . . .	1
1.2	Historical overview . . . . .	2
1.3	The operation of a laser . . . . .	3
1.4	Basic design of a laser . . . . .	5
1.5	Lasing parameters . . . . .	6
1.6	Excimer lasers . . . . .	8
1.7	Why long pulse excimer lasers? . . . . .	8
	References . . . . .	9
<b>2</b>	<b>Theoretical considerations</b>	<b>13</b>
2.1	The ArF laser . . . . .	13
2.2	Discharge formation and stability . . . . .	17
	References . . . . .	22
<b>3</b>	<b>The X-ray source</b>	<b>25</b>
3.1	Experimental set-up . . . . .	26
3.2	Characterisation of the X-ray source . . . . .	30
3.3	Pre-ionisation electron density measurements . . . . .	32

---

References . . . . .	37
<b>4 Excitation circuits and modes of operation</b>	<b>39</b>
4.1 Charge-Transfer mode . . . . .	40
4.2 Church mode . . . . .	42
4.3 Swing mode . . . . .	44
4.4 Resonant Overshoot mode (with a rail gap) . . . . .	45
4.5 Intermezzo: Saturable inductors . . . . .	47
4.6 Resonant Overshoot mode (with a saturable inductor) . . . . .	50
4.7 Switch mode . . . . .	53
4.8 Other modes . . . . .	55
4.9 Three-electrode operation . . . . .	55
References . . . . .	57
<b>5 Short pulse operation</b>	<b>59</b>
5.1 Experimental set-up . . . . .	60
5.2 Electrical behaviour . . . . .	63
5.2.1 Rail gap switched circuits . . . . .	64
5.2.2 Magnetically-switched resonant overshoot mode . . . . .	65
5.2.3 Comparison of the resonant overshoot mode with different switches	67
5.2.4 X-ray triggered mode . . . . .	69
5.2.5 Three-electrode circuit . . . . .	70
5.3 Pre-ionisation timing effects . . . . .	71
5.3.1 Rail gap switched circuits . . . . .	72
5.3.2 Ferrite switched resonant overshoot mode . . . . .	79
5.4 Influence of the pumping power . . . . .	81
5.5 Conclusions . . . . .	85
References . . . . .	86



<b>6 Intermediate pulse length operation and modelling</b>	<b>89</b>
6.1 Experimental set-up . . . . .	90
6.2 Experimental results . . . . .	92
6.3 Kinetic modelling . . . . .	96
6.3.1 Calculated results . . . . .	97
6.4 Comparison between experimental and calculated results . . . . .	103
6.5 Conclusions . . . . .	107
References . . . . .	110
<b>7 Long pulse operation</b>	<b>113</b>
7.1 Experimental set-up . . . . .	113
7.2 Experimental results and discussion . . . . .	115
7.2.1 Dependency on the pre-ionisation timing . . . . .	116
7.2.2 Dependency on the gas composition . . . . .	119
7.2.3 Dependency on the pumping power . . . . .	129
7.3 Conclusions . . . . .	131
References . . . . .	133
<b>8 Design considerations for future devices</b>	<b>135</b>
8.1 Design parameters . . . . .	135
8.2 Further study . . . . .	137
<b>A The mini-marx generator</b>	<b>139</b>
References . . . . .	141
<b>B Description of the kinetic model</b>	<b>143</b>
B.1 Kinetic model . . . . .	144
B.2 Solving the Boltzmann equation . . . . .	145

---

B.3 Parallel resistor model of a gas discharge . . . . .	147
B.4 Rate equations . . . . .	148
References . . . . .	151
<b>Summary</b>	<b>153</b>
<b>Samenvatting</b>	<b>157</b>
<b>Curriculum vitae</b>	<b>161</b>
<b>List of publications</b>	<b>163</b>

# Chapter 1

## Introduction

### 1.1 Structure of this thesis

The research documented in this thesis concerns an X-ray pre-ionised, gas discharge excited argon fluorine excimer laser. In the introduction (Chapter 1) some basic laser theory is reviewed briefly, starting with a short historical overview. In the second chapter the theoretical implications for the studied ArF laser are dealt with in some more detail.

Next, the experimental set-up is discussed. The X-ray source, used to pre-ionise the laser gas mixture, is discussed in chapter 3. In chapter 4 the operation of the different electric circuits used in the research is explained.

The results of the research are presented in the chapters 5, 6 and 7. Chapter 5 concerns an investigation of the operation characteristics of the laser, using different excitation circuits. In chapter 6 a modification of the experimental set-up is studied both experimentally and theoretically. The generation of the long laser pulses mentioned in the title of this thesis is discussed in chapter 7.

In chapter 8 the main conclusions of the research are summarised in the form of design considerations for future lasers operating in the same regime as the one studied in this work.

In a gas discharge pumped excimer laser a number of factors are inherently intertwined. The basic factors determining the pulse length are the discharge quality,

the gas kinetics and several set-up properties, such as the electric circuitry and the mirror reflection. The discharge quality is primarily determined by the pre-ionisation of the gas, the pumping circuit parameters, the gas kinetics and set-up properties, e.g. the electrode design. The gas kinetics are determined by the natural properties of the gases themselves, the number densities of the ingredients and the energies of the particles, as determined by the discharge parameters. The gas kinetics have an effect on the discharge behaviour, which in its own right has an effect on the gas kinetics. It is therefore inevitable that within our experiments some parameters are varied simultaneously, which increases the difficulties in understanding the observed results.

## 1.2 Historical overview

Laser research has a long and eventful history. Its starting point is usually considered to be the 1917 paper by Albert Einstein in which he explained the interaction between radiation and matter [1], see also section 1.3. However, it lasted until 1953 before Gordon, Zeiger and Townes realised the worlds first device to make use of stimulated emission of radiation, an  $\text{NH}_3$  microwave amplifier operating at a frequency of 24 MHz [2]. Their invention was called a *maser*, which is the acronym of: microwave amplification by stimulated emission of radiation. In 1958 Schawlow and Townes speculated that the operating range of masers could be extended to shorter wave lengths if a ‘leaking’ resonant cavity was constructed around the emitting medium [3]. Using the partially silvered end-faces of a ruby-rod, Maiman proved this theory by constructing the first *laser*, oscillating at  $\lambda = 694 \text{ nm}$  [4]. In the word laser ‘light’ replaces the word ‘microwave’ of the ‘maser’. (Later on the word ‘laser’ also was transferred into a verb, both in the form of ‘to lase’ and ‘to laser’.)

The first continuous gas laser was the He:Ne laser, operating in the infrared region,  $\lambda = 1.15 \mu\text{m}$  [5]. This was also the first gas discharge laser. The now well-known and frequently used visible red line of the He:Ne laser,  $\lambda = 632.8 \text{ nm}$ , was found one year later [6].

The research of lasers and masers was rewarded in 1964 with the Nobel prize in physics, shared by Townes, Basov and Prokhorov [7].

In the meantime, in 1960, Houtermans discussed the possibilities of lasing between an excited state and a repulsive lower state, such as is found in noble gases [8]. Indeed, in 1971 Basov and coworkers demonstrated the first excimer laser,  $\text{Xe}_2^*$ , with  $\lambda = 172 \text{ nm}$  [9]. ‘Excimer’ is a contraction of the words ‘excited dimer’, a class

of molecules which exist only in an excited state. The following milestone was the construction of the first ‘exciplex’ (excited complex) laser, XeBr\*,  $\lambda = 282$  nm, by Searles and Hart in 1975 [10]. The ArF laser is one of this last class of laser. The first electron beam excited ArF laser was built by Hoffman et al. in 1976 and half a year later a gas discharge pumped ArF laser was realised by Burnham and Djeu [11].

Until now discharge pumped ArF lasers were only operated with fairly short pulses, up to 25 ns. In this work we report on the next step in the ArF laser research: the extension of the pulse length beyond 100 ns.

### 1.3 The operation of a laser

There is a vast number of papers written on the properties of lasers and lasing, e.g. see Siegman [12] and, in Dutch, Stijns [13]. Here we will limit ourselves to some basic facts about light and lasing so as to give a rough guideline for the following discussions, without attempting to be exhaustive.

The basics of the operation of a laser are contained in the word itself and the historical overview above shows some steps needed to construct a laser.

Light, or microwave radiation, is somehow amplified through the process of stimulated emission, introduced by A. Einstein. He considered a collection of identical particles, each having two different energy levels  $E_1$  and  $E_2$ ,  $E_2 > E_1$ , with populations  $N_1$  and  $N_2$ . The energy difference between these levels corresponds to a radiation frequency  $\nu_{12}$  according to:

$$\Delta E_{12} = E_2 - E_1 = h\nu_{12}. \quad (1.1)$$

The particles can gain or lose the energy difference  $\Delta E_{12}$  via three different processes, see figure 1.1:

- *Absorption*, with coefficient  $B_{12}$ , which depends on the radiation field energy density  $\rho$  at  $\nu = \nu_{12}$  and the population of the lower energy level, or:  $dN_2/dt = B_{12}\rho(\nu_{12})N_1$ .
- *Spontaneous emission*, with coefficient  $A_{21}$ , which only depends on the population of the upper energy level, or:  $dN_2/dt = A_{21}N_2$ .
- *Induced or Stimulated emission*, with coefficient  $B_{21}$ , which depends on the radiation field and the population of the upper level, or:  $dN_2/dt = B_{21}\rho(\nu_{12})N_2$ .

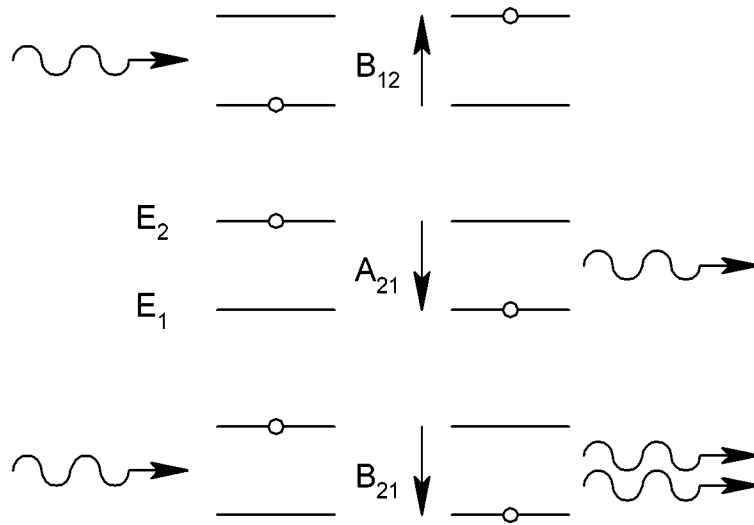


Figure 1.1: A schematic representation of the absorption (upper diagram), the spontaneous emission (middle diagram) and the stimulated emission (lower diagram) of radiation by a two-level atom.

In thermal equilibrium the lower level is more densely populated than the upper level. In order to generate radiation a higher population of the upper level than of the lower level is needed, the so-called ‘population inversion’. This takes energy which has to be pumped into the medium.

It is clear that the two-level system of the above example cannot sustain lasing, since the upper level population fills up the lower level upon emitting radiation, thus re-establishing the thermal equilibrium. In order to sustain lasing a third level is needed with an energy  $E_3 < E_1$ . The lifetime of the population of the lower level should be shorter than that of the upper level. In that case the lasing process proceeds as follows: a particle is pumped from the lowest level to the upper laser level, from which it relaxes to the lower laser level by emitting a photon. The particle then quickly returns to the lowest state via some other relaxation mechanism, so that the cycle can start anew.

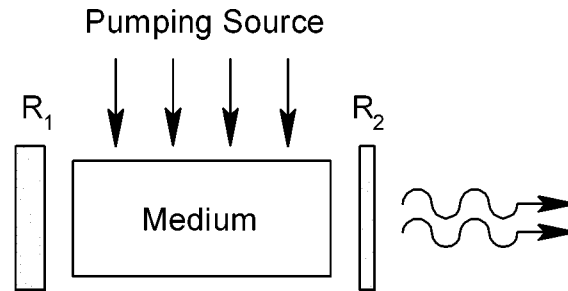


Figure 1.2: Schematic drawing of a laser. A laser consists of an emitting medium, a pumping source and an optical resonator. The resonator is formed by two mirrors with reflection coefficients  $R_1$  and  $R_2$ , respectively.

## 1.4 Basic design of a laser

A laser basically consists of three parts, see figure 1.2:

- An emitting medium.
- A pumping source.
- A resonator, formed by a set of mirrors.

The emitting medium may consist of gases, liquids or solids. Lasers have even been built with edible media [12]. The pumping source can be anything from another light source to high energy electrons and chemical reactions, or even as far-fetched as nuclear energy [14] or the shock waves from explosions [15].

The first ArF laser was realised by using electron beam pumping by Hoffman, Hays and Tisone in 1976 [16]. Half a year later the first paper on a discharge pumped ArF laser was published by Burnham and Djeu [11]. Discharge excited devices have many advantages (and some drawbacks) over electron beam pumped devices;

- The electron beam is generated in a vacuum, while the laser gas mixture has a pressure of several bar. The two vessels are separated by a thin foil. The electrons have to penetrate the foil which causes losses. The foil is a weak link in the system, reducing the reliability of the device.

- In a discharge laser solid electrodes can be used with relatively low voltages, compared with an e-beam set-up.
- In discharge pumped lasers there is no need for a very thin high-pressure/vacuum separation that can break down.
- High power discharges in halogen containing gas mixtures are inherently unstable, see section 2.2, thus continuous operation is impossible. E-beam devices have pulse repetition rates of up to 100 Hz, while discharges can be run at several kHz.
- The electron energy in a discharge is lower than that of an e-beam pumped device, resulting in a lower formation efficiency of the  $\text{ArF}^*$ -molecule. The efficiency of an e-beam pumped ArF laser can be up to 8 % [17,18], while that of a discharge pumped system is less than 4 % [19].

As has been indicated before, stimulated emission is dependent on the present radiation field  $\rho(\nu)$ . A higher radiation field thus increases the contribution of the stimulated emission to the field. The function of the laser mirrors is to reflect the radiation back into the medium, so that the irradiance can increase even further. However, there is a maximum irradiance inside the resonator, the value of which is determined by the specific properties of the medium. A laser always starts from the ‘noise’ of the spontaneous emission, which is then increased by the optical feedback from the resonator. To obtain the laser beam one of the mirrors is only partly reflecting, transmitting the rest. When the reflection of the mirrors is too low, so that the optical feedback is not high enough, lasing is impossible, even when a high degree of population inversion has been reached. All energy is then lost in spontaneous emission and other possible relaxation mechanisms of the upper laser level.

## 1.5 Lasing parameters

Consider a medium in which population inversion has been established, between two resonator mirrors with reflection coefficients  $R_1$  and  $R_2$  respectively. The irradiance  $I_\nu$  of a monochromatic and collimated beam passing through the medium grows by stimulated emission with distance  $x$  according to:

$$I_\nu(x) = I_\nu(0) e^{(\alpha-\gamma)x}, \quad (1.2)$$



where  $\alpha$  is a gain coefficient that depends on the pumping power  $P_{\text{in}}$  and on the population inversion.  $\gamma$  is the summation of all optical losses inside the medium, except for the intended outcoupling losses at the mirrors. The irradiance grows according to equation 1.2 until an equilibrium is reached between the depopulation of the upper laser level by the stimulated emission and the production rate of the population inversion. This is called gain saturation.

Optical losses which contribute to  $\gamma$  are:

1. Absorption and scattering at mirrors and windows.
2. Diffraction losses at mirrors and windows.
3. Absorption of laser-radiation by the lower laser level which is re-emitted in other directions by spontaneous emission.
4. Absorption by other gas mixture components.
5. Absorption and scattering by inhomogeneities in the discharge.

For a complete cavity round-trip through a resonator of length  $L$  we find the power gain  $G$ :

$$G = \frac{I_{\text{initial}}}{I_{\text{final}}} = R_1 R_2 e^{(\alpha - \gamma)2L} \quad (1.3)$$

When  $G > 1$  the irradiance grows, when  $G < 1$  it decreases. The threshold condition for lasing is thus  $G = 1$ , so that the threshold gain coefficient is:

$$\alpha_{\text{th}} = \gamma - \frac{1}{2L} \ln(R_1 R_2). \quad (1.4)$$

Since  $\alpha$  depends on the pumping power  $P_{\text{in}}$ , it is clear that the effective pumping power must be high enough to overcome all optical losses. The effective pumping power is defined as the part of the supplied energy that is actually used in the pumping process, which can be a very small part, e.g. due to electrical losses in the set-up. The critical effective pumping power is given by

$$P_{\text{th}} = \frac{8\pi h}{c^2} \alpha_{\text{th}} \nu^3 \Delta\nu, \quad (1.5)$$

where  $\Delta\nu$  is the bandwidth of the radiation field. Since  $\nu = c/\lambda$ , it can be seen from equation 1.5 that the necessary pumping power rapidly increases with a decreasing laser wavelength.

Species	He	Ne	Ar	Kr	Xe
F	-	(108)	193	248	351
Cl	-	-	175	222	308
Br	-	-	(161)	206	282
I	-	-	-	(185)	(253)

Table 1.1: The wavelengths (in nm) of the main observed optical transitions in di-atomic rare gas halogen excimer molecules. Numbers in brackets indicate that only fluorescence has been observed at that wavelength. Data taken from refs. [20–23].

## 1.6 Excimer lasers

Excimer lasers are lasers in which the lasing species is an excited molecule that has a repulsive (or very weakly bound) lower state. Once the molecule has undergone the radiative transition from the upper to the lower laser state, it almost immediately disintegrates, thus preventing the build-up of a significant population of the lower laser level. Therefore, the laser output power depends on the production rate of the excited molecules that make up the upper laser level, and not on the depopulation rate of the lower laser level, as is the case with other lasers.

Most excimer molecules used in lasers are di-atomic rare gas-halogen complexes. Therefore they were originally called ‘exciplex’ lasers. The catchword excimer laser is now used commonly for all real excimer lasers, exciplex lasers and even several halogen lasers, such as the molecular fluorine laser (with  $\lambda_{F_2} = 157$  nm), although the latter does have a bound lower state.

An overview of different rare gas-halide excimer lasers and their wavelengths is given in table 1.1.

## 1.7 Why long pulse excimer lasers?

Excimer lasers can be very powerful lasers with large beam diameters at short wavelengths, see also chapter 2. A short wavelength means a high photon energy. These properties make excimer lasers ideally suitable for applications such as nano-lithography, a variety of surgeries, i.e. eye, ear, mucosal surgery etc. as well as dentistry, surface-ablation studies, X-ray plasma generation and fast cutting and drilling of large

numbers of small holes in metals and composites, e.g. for use in turbine-blades and aircraft wings. Nowadays memory chips can be readily processed with details below  $0.13\ \mu\text{m}$  using ArF lasers [24].

However, these applications need a high beam quality, which means a low divergence of the beam and a narrow spectral bandwidth of the radiation. The properties of the laser beam are mainly determined by the resonator properties. When the radiation field inside the resonator starts from the optical noise of the spontaneous emission it has a large number of degrees of freedom. After several round trips inside the resonator only those spectral and spatial modes that fit the resonator are amplified enough to sustain lasing, while the other modes die out. The result is a narrower bandwidth and a decreased divergence, which allows for better transportation of the beam over long distances and a better focusability of the beam for small-size applications.

For pulsed lasers the combination of the resonator set-up and the pulse duration is a decisive parameter for the beam quality; longer pulses can generate better quality beams. An extensive treatment of different aspects of the beam quality of a long-pulse XeCl excimer laser can be found in the PhD-thesis of R.M. Hofstra, ref. [25].

Other factors of importance are that using long pulses reduces the damaging of optics, since such processes as compaction and colour centre formation are related to the incident intensity. Long laser pulses equally facilitate the transportation of optical signals through fibers. It has also been shown that long excimer laser pulses are very interesting for the generation of long X-ray pulses for the *in vivo* study of bacteria [26]. Furthermore, long pulse operation lowers stresses on the electrical components of the set-up, as may be seen from a comparison between the results of chapter 4 and chapter 7.

## References

- [1] **A. Einstein**, *Zur Quantentheorie der Strahlung*, Physik. Zeitschr. **18**, 121–128 (1917). (In German).
- [2] **J.P. Gordon, H.J. Zeiger and C.H. Townes**, *The maser - new type of microwave amplifier, frequency standard, and spectrometer*, Phys. Rev. **99** (4), 1264–1274 (1955).
- [3] **A.L. Schawlow and C.H. Townes**, *Infrared and optical masers*, Phys. Rev. **112** (6), 1940–1949 (1958).
- [4] **T.H. Maiman**, *Stimulated optical radiation in ruby*, Nature **187**, 493–494 (1960).
- [5] **A. Javan, jr. W.R. Bennett and D.R. Herriott**, *Population inversion and continuous optical maser oscillation in a gas discharge containing a He:Ne mixture*, Phys. Rev. Lett. **6**, 106–110 (1961).

- [6] **A.D. White and J.D. Rigden**, *Continuous gas maser operation in the visible*, Proc. IRE **50**, 1697 (1962).
- [7] **C.H. Townes, N.G. Basov and A.M. Prokhorov**, Nobel Prize in Physics 1964; “For the invention of the maser and the laser”. The text of the Presentation Speech can be read at: <http://nobel.sdsc.edu/laureates/physics-1964-press.html>.
- [8] **F.G. Houtermans**, *Über Maser-Wirkung im optischen Spektralgebiet und die Möglichkeit absolut negativer Absorption für einige Fälle von Molekülspektren (Licht-Lawine)*, Helv. Phys. Acta **33**, 933–940 (1960). (In German).
- [9] **N.G. Basov, V.A. Danilychev and Y.M. Popov**, *Stimulated emission in the vacuum ultraviolet region*, Sov. J. Quantum Electron. **1** (1), 18–22 (1971). [Kvantovaya Elektron. **1** (1), 29–34 (1971)].
- [10] **S.K. Searles and G.A. Hart**, *Stimulated emission at 281.8 nm from  $XeBr^+$* , Appl. Phys. Lett. **27** (4), 243–245 (1975).
- [11] **R. Burnham and N. Djeu**, *Ultraviolet-preionized discharge-pumped lasers in  $XeF$ ,  $KrF$  and  $ArF$* , Appl. Phys. Lett. **29** (11), 707–709 (1976).
- [12] **A.E. Siegman**, *Lasers*, University Science Books, Mill Valley, CA, USA (1986).
- [13] **E. Stijns**, *Lasers: een inleiding voor het universitair en technisch hoger onderwijs*, VUB-Press, Brussels, Belgium (1991). (In Dutch).
- [14] **E.P. Magda**, *Review: powerful nuclear pumped lasers*, In: XII International Symposium on Gas Flow and Chemical Lasers and High-Power Laser Conference, A.S. Boreisho and G.A. Baranov, eds., Proceedings of SPIE **3574**, 93–103 (1998).
- [15] **N.G. Basov, B.A. Vyskubenko, E.M. Zemskov, V.S. Zuev, V.M. Kazansky, V.A. Katulin, G.A. Kirillov, S.B. Kormer, O.Yu. Nosach and S.A. Sukharev**, *High-energy explosively pumped photodissociation lasers*, In: XII International Symposium on Gas Flow and Chemical Lasers and High-Power Laser Conference, A.S. Boreisho and G.A. Baranov, eds., Proceedings of SPIE **3574**, 398–402 (1998).
- [16] **J.M. Hoffman, A.K. Hays and G.C. Tisone**, *High-power UV noble-gas-halide lasers*, Appl. Phys. Lett. **28** (9), 538–539 (1976).
- [17] **P.J.M. Peters and H.M.J. Bastiaens**, *High-energy density  $ArF^*$  laser excited by a coaxial electron beam*. Poster WK31 at the Conference on Lasers and Electro-Optics, San Francisco, CA, USA, (1998).
- [18] **A.M. Boïchenko, V.I. Derzhiev, A.G. Zhidkov and S.I. Yakovlenko**, *Kinetic model of an  $ArF$  laser*, Sov. J. Quantum Electron. **22** (5), 444–448 (1992). [Kvantovaya Elektron. **19**, 486–491 (1992)].
- [19] **D. Lo, A.I. Shchedrin and A.V. Ryabtsev**, *The upper energy limit of a self-sustained discharge-pumped  $ArF$  laser*, J. Phys. D: Appl. Phys. **29**, 43–49 (1996).
- [20] **Ch.A. Brau**, *Rare gas halogen excimers*, In: Excimer lasers, Ch.K. Rhodes, ed., Topics in Applied Physics **30**, ch. 4, 87–137, Springer Verlag, Berlin, 2nd enlarged edition, (1984).

- 
- [21] **R.W. Waynant**, *A discharge-pumped ArCl superfluorescent laser at 175.0 nm*, Appl. Phys. Lett. **30** (5), 234–235 (1977).
- [22] **R.W. Waynant**, *Inert-gas halide VUV lasers*, Sov. J. Quantum Electron. **8** (8), 1002–1004 (1978). [Kvantovaya Elektron. **5**, 1767–1770 (1978)].
- [23] **J.T. Verdeyen**, *Laser electronics*, Prentice Hall, New Jersey, 2nd edition (1989).
- [24] **H. Morimoto and H. Ohtsuka**, *Present status of ArF lithography development and mask technology*, In: Photomask and X-Ray Mask Technology V, N. Aizaki, ed., Proceedings of SPIE **3412**, 338–340 (1999).
- [25] **R.M. Hofstra**, *On the optical performance of the long pulse XeCl\* excimer laser*, PhD thesis, University of Twente, Enschede, The Netherlands (1999).
- [26] **S. Bollanti, P. Di Lazarro, F. Flora, G. Giordano, T. Letardi, G. Schina, C.E. Zheng, L. Filippi, L. Palladino, A. Reale, G. Taglieri, D. Batani, A. Mauri, M. Belli, A. Scafati, L. Reale, P. Albertano, A. Grilli, A. Faenov, T. Pikuz and R. Cotton**, *Long-duration soft X-ray pulses by XeCl laser driven plasmas and applications*, J. X-ray Sci. and Techn. **5**, 261–277 (1995).



## Chapter 2

# Theoretical considerations

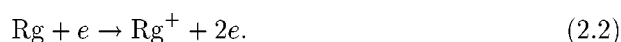
In this chapter we first shed some light on the theoretical background of the ArF-lasing process in a discharge pumped laser. In the second part several qualities of the discharge plasma are discussed.

### 2.1 The ArF laser

In a gas discharge the electric energy is transferred to the gas via the discharge electrons, which are accelerated by the electric field. The low energy electrons merely heat up the gas via elastic collisions with the heavy atoms and molecules. The electrons in the high energy tail of the electron energy distribution function can excite rare gas atoms via inelastic collisions:



where Rg denotes a rare gas atom. Only a rather small fraction (a few per cent) of the electrons contribute to the direct ionisation of the rare gases [1]:

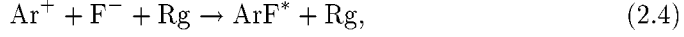


Most ions are formed by step-wise ionisation via the excited states.

The  $\text{ArF}^*$  molecule is formed by three main processes: the so-called ‘harpooning’ reaction between an excited argon atom and molecular fluorine



and the two ionic recombination processes



and



In an e-beam pumped ArF laser Maeda et al. [2] found that the contribution of the harpooning process to the formation of  $\text{ArF}^*$  molecules increases when the average electron temperature in the gas decreases. Nagai et al. [3] found that in the first stages of a gas discharge the harpooning process has a larger contribution to the formation than later in the discharge, where ionic recombination becomes more important. In their model of an ArF laser discharge, with He as buffer gas and at a total gas pressure of 2.53 bar, Akashi et al. [4] used the following efficiencies for the formation channels of the ArF molecule: 79.9 % of the  $\text{ArF}^*$  molecules is assumed to be formed by harpooning [Eq. 2.3], 19.1 % by ionic recombination between  $\text{Ar}^+$  and  $\text{F}^-$  [Eq. 2.4] and 1.0 % by ionic recombination between  $\text{Ar}_2^+$  and  $\text{F}^-$  [Eq. 2.5]. Boïchenko et al. found that the equilibrium between the harpooning and the ionic recombination processes in the laser differs with the used buffer gas [5].

Since in a long-pulse laser the used voltages, and thus the electric fields, are lower than in a short-pulse laser, the mean electron energy in a long-pulse laser is less than in a short pulse laser. We may therefore assume that the contribution of the harpooning process is larger in a long pulse laser than in a short pulse laser.

The  $\text{ArF}^*$  molecule exists in two very closely lying upper states, the *B* and the *C* state [6, 7]. The mixing between the two states is sufficient for both states to be treated as a single state with a lifetime of 4.2 ns [6]. The lower level states, *A* and *X*, are also strongly mixed. Therefore, the radiative transitions between the upper level states and the lower level can be seen as a continuum without a structure [1,6,8]. The accordingly simplified energy level diagram of the  $\text{ArF}^*$  molecule and the radiating transition is shown in figure 2.1.

Although ArF lasing has been observed in e-beam devices in mixtures of only the active ingredients Ar and  $\text{F}_2$ , e.g. see refs. [2,5,9], in discharge excited lasers usually only a few percents of these gases are used in the buffer gases He and/or Ne. The ArF laser has been operated with  $\text{NF}_3$  as the fluorine donor [8], but generally  $\text{F}_2$  is used.

A schematic diagram of the kinetic reactions in an ArF laser discharge of Ar,  $\text{F}_2$  and Ne is shown in figure 2.2. The energy flow in a gas mixture with a He buffer is equivalent, although the rate equations and the energies of the species differ somewhat [6].



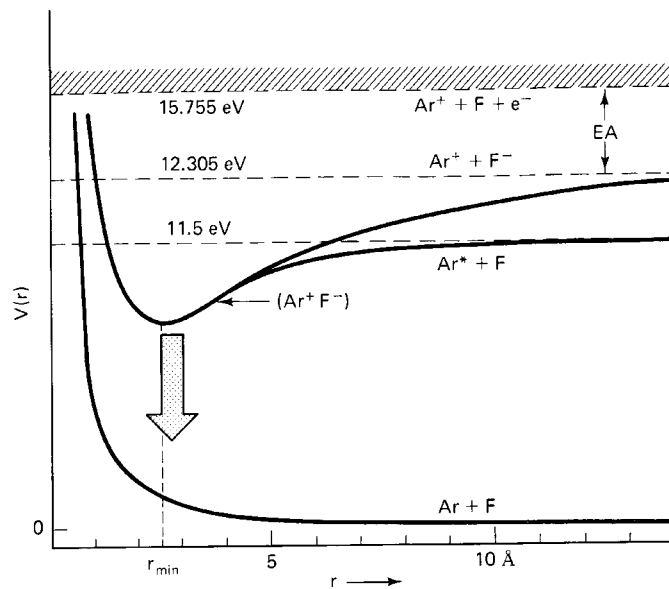


Figure 2.1: Energy level diagram of the  $\text{ArF}^*$  excimer, showing the main formation channels and the radiative transition to the repulsive lower level. The upper level consists of the B (upper curve) and C (lower curve) states which may be treated, at low internuclear spacing, as a single state. The lower level states A and X can also be considered a single state.  $r$ : Internuclear spacing.  $V(r)$ : Energy. EA: Electron affinity. Taken from Verdeyen, ref. [1].

In appendix B a number of kinetic reactions for the case of using He as the buffer gas is given. These reactions are used for the modelling of the laser in chapter 6.

The main formation channels are indicated with bold arrows in figure 2.2. From the figure it can be seen that several reactions are taking place in the discharge which channel energy away from the formation processes or which quench the  $\text{ArF}^*$  molecule itself. The most effective mechanisms of these are the quenching by  $\text{F}_2$  and by electrons [5].

Besides these reactions the generated 193 nm photons are absorbed in the discharge by

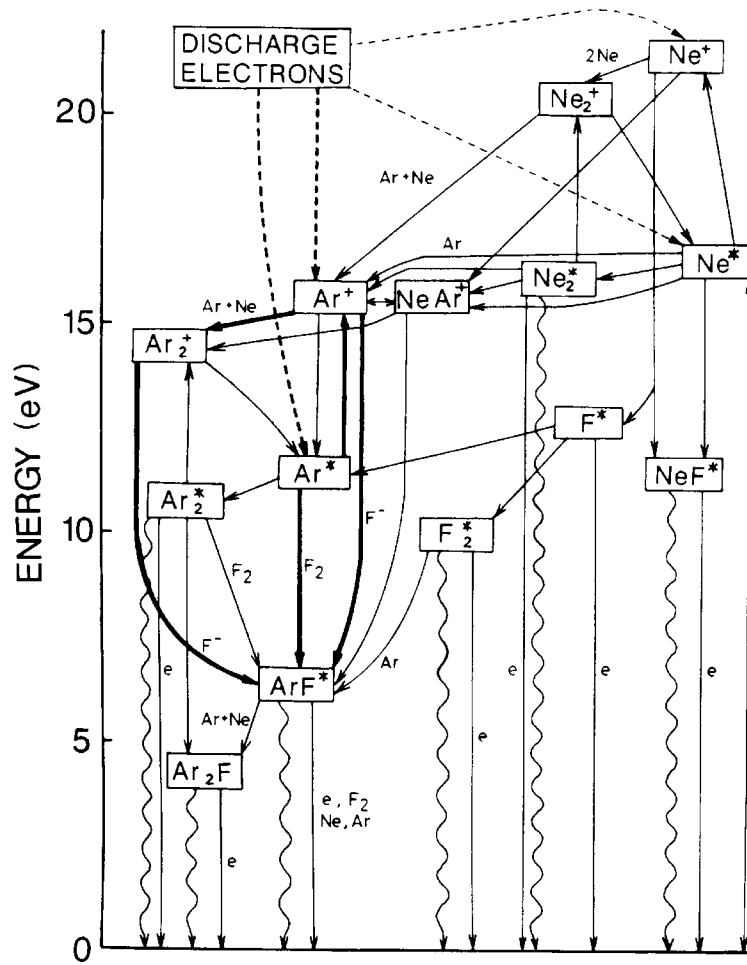


Figure 2.2: Energy level diagram of an ArF discharge with Ne as the buffer gas. The diagram remains valid for the case of He as the buffer gas, although the energy levels of He are somewhat different from those of Ne. Taken from Ohwa and Obara, ref. [6].

$F^-$  and  $Ar^*$ , as well as by all rare gas dimers  $Rg_2^*$  in the mixture and by  $Ar_2F^*$  [3–5,10], although the latter reaction results in the reformation of an  $ArF^*$  molecule. Trace impurities of organic molecules also strongly absorb the ultra violet photons.

Discharge pumped ArF lasers radiate at a wavelength of  $193.3 \pm 0.5$  nm, which means a photon energy of  $\sim 6.4$  eV [8,11–14]. The peak intensity wavelength is found to shift to longer wavelengths with increasing pressure. In the first observation of ArF radiation by Golde [15], in an after-glow experiment at a total gas pressure of a few torr, the measured wavelength was even as low as  $\lambda = 190.0 \pm 0.6$  nm.

Within the spectrum of the ArF radiation strong absorption bands are present from the Schumann-Runge bands of  $O_2$  [8,11,12,14,16,17]. The large effect of the  $O_2$  absorption is shown by Greene and Brau [16], who reported a two-fold output increase of their laser after the removal of  $O_2$  from the optical path inside the resonator. The absorption from  $F^-$  ions in the discharge has also been found in the radiation spectrum [3].

However, the effects of absorption of the radiation by impurities can be decreased by purification of the gas mixture and a thorough passivation of the laser vessel [12,17–19].

## 2.2 Discharge formation and stability

Discharges can roughly be divided in two: on the one hand streamer- or arc-like discharges, such as arcs and lightnings, and on the other hand glow-discharges that fill large volumes with a homogeneous plasma.

An arc-like discharge starts when a free electron is accelerated by a strong electric field, gaining enough kinetic energy to ionise the gas molecules and atoms with which it collides. The electrons that are freed in these collisions are accelerated as well, thus resulting in a self-increasing electron avalanche. Since the electrons move much faster than the ions, a cone-like wake of positive ions is formed behind the negatively charged electron cloud, see figure 2.3. This positive wake can attract other electron clouds and the result is a more or less narrow conductive channel which can carry large amounts of current. The electrons starting the small attracted streamers can be the result of UV-ionisation by the head of the primary avalanche [20,21].

However, this type of discharge cannot fill a large volume completely. For large scale homogeneous discharges it is necessary to pre-ionise the gas so as to form a homogeneous electron density distribution, from which a large number of electron

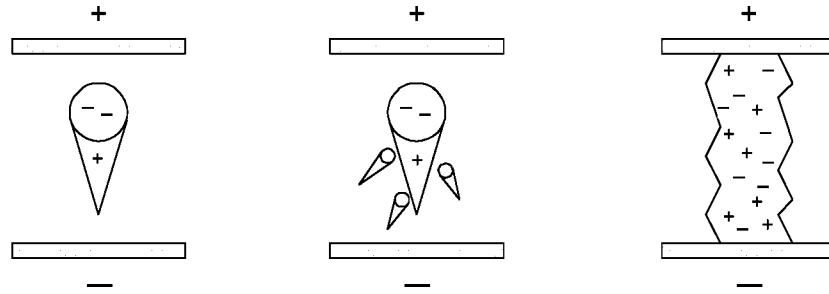


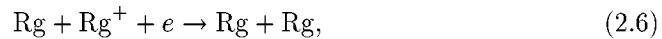
Figure 2.3: The growth of an electron avalanche into a streamer- or arc-discharge. Left: Moving electron cloud with a cone-shaped wake of positive ions. Centre: Small avalanches are attracted to the large ion-cone. Right: A conducting channel between the two electrodes is formed.

avalanches can start simultaneously. The resulting overlapping electron clouds and ion-cones forms a homogeneous plasma, see figure 2.4.

Several authors have discussed the theoretical criteria for a minimum pre-ionisation electron density to ensure a good discharge homogeneity, e.g. see [20–22]. In the calculations of Levatter and Lin, ref. [21], an average minimum pre-ionisation electron density of approximately  $10^8 \text{ cm}^{-3}$  is found by assuming a minimum overlap of the avalanche heads after a certain multiplication time. However, when the electrode voltage rise time is very short the pre-ionisation electron density should be higher than  $10^8 \text{ cm}^{-3}$  and with a long voltage rise time a lower electron density can be allowed.

In order to start a discharge, the pre-ionisation electron density must be multiplied to the discharge level of  $\sim 10^{14} \text{ cm}^{-3}$  [23] by the electric field.

Once the electron density has become high enough, the ionisation becomes equal to the electron losses. The main electron loss processes are the ionic recombination in the form of a three-body collision process:



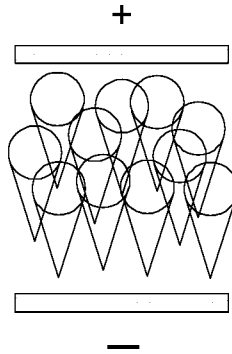


Figure 2.4: The effect of a homogeneous pre-ionisation electron density: the electron clouds and the ion-cones overlap, yielding a homogeneous charge carrier density and thus a homogeneous discharge plasma.

and the dissociative electron attachment to fluorine:



Since the attachment to fluorine occurs at a rate of  $10^{-9} \text{ cm}^3/\text{s}$  [24], which is much faster than the ionic recombination, we can write

$$\frac{dn_e}{dt} = \{\alpha(E) - \beta(E)\} n_e v_d(E), \quad (2.8)$$

where  $n_e$  is the number of electrons,  $\alpha(E)$  is the electric field dependent first Townsend ionisation coefficient for the gas mixture,  $\beta(E)$  is the electron attachment coefficient of fluorine of equation 2.7 and  $v_d(E)$  is the drift velocity of the electrons in the electric field. The attachment rate coefficient of fluorine rapidly decreases with increasing electron energy [24, 25].

From this discussion it can be seen that for a given electric field the discharge plasma can reach a steady state, determined by the electron balance 2.8. A discharge in its steady state has a low impedance, which is more or less inversely proportional to the discharge current. The high electron density in such a discharge makes it a very efficient tool for the formation of excimer molecules.

If the excitation circuit allows so, the discharge can be operated at a steady state voltage  $V_{SS} \propto E_{SS}$ , which is determined by the electron balance 2.8 and by the qualities of the experimental set-up. However, if the local discharge properties at one point are somewhat different from the rest of the discharge, the local  $E_{SS}$  may be slightly different from that of the surrounding plasma. If, for instance, the fluorine concentration at one point is lower than in the surrounding region, the electron loss due to attachment is decreased causing a local electron excess, which leads to an increase of the local field, that causes a higher ionisation rate, which causes a higher electron density, that cannot be balanced by the attachment to fluorine . . . And so on and so forth. This process is called halogen depletion [26] or an Operating Point Instability [27]. Thus, the instability grows with an increasing speed until a plasma filament is formed that bridges the electrode gap and forms a short-circuiting arc. The same runaway loop occurs if the local electric field is slightly higher than the surrounding field, for instance at a small protrusion from the electrode [28].

At the boundary of the cathode the number of electrons is governed by the field emission properties of the cathode material. Usually the cathode emission characteristics prevent it from supplying enough electrons to sustain the discharge at the steady state field, so that a positively charged cathode layer is formed. The current in the cathode layer is then initially carried by the positive ions, which bombard the cathode with enough energy to create hot spots in which the electron emission is greatly enhanced. Later in the discharge almost all current is supplied to the discharge via the cathode hot spots.

The hot spot formation and density on the cathode has been attributed to several factors [4, 10, 28–37],

- The cathode roughness; electrode protrusions increase the local field strength and thus the field emission of electrons.
- The cathode material; the field emission is determined by the work function of the cathode material.
- The rise time of the current through the discharge; a faster current density rise yields more and smaller hot spots.
- The discharge gas; the kinetic energy with which the positive ions strike the cathode determines the electrode temperature.
- The condition of the upper cathode layer; contamination of the cathode changes the emission properties.

- The pre-ionisation electron density; a higher electron density yields more and smaller hot spots.
- The breakdown voltage of the discharge; a higher breakdown voltage yields more and smaller hot spots.
- The irradiance of the laser light on the cathode; according to Akashi et al. [10] the photo-ionisation and the photo-detachments processes influence the cathode sheet homogeneity.

Using highly polished copper electrodes, Dreiskemper et al. [30] have shown that high current density carrying hot spot-free discharges do exist, leading them to the conclusion that hot spots are *always* triggered by electrode surface inhomogeneities. In their hot spot-free discharges a bright cathode sheet is formed, which can be thought of as one huge single hot spot, covering the entire electrode surface homogeneously.

Since discrete hot spots are local density fluctuations in the electric field, they have a profound impact on the stability of the discharge. Hot spots are the main starting point for plasma filaments growing into the discharge [27, 29–32, 34, 37]. On photographs of XeCl and KrF laser discharges in these references filaments protruding from cathode hot spots may be seen that end in cup-like features which spread out into the homogeneous part. These filaments grow further into the discharge until either the current pulse ends or until they have bridged the electrode gap, forming a short-circuiting arc. If the voltage reverses over a discharge, because of oscillations in the excitation circuit, the process occurs at the other electrode as well [32]. This increases the chances of short-circuiting when opposite streamers connect. Therefore discharges tend to arc more easily when the direction of the current is reversed during the discharge.

To minimise the chances of the formation of instabilities due to electric field inhomogeneities, several authors have developed analytical expressions for the design of electrodes which cause minimum electrical field distortions by the electrode boundaries, see for instance refs. [38–40].

However, discharge instabilities arise from other small-scale inhomogeneities as well. Even the hot spot-free discharges of Dreiskemper et al. [30] show filamentary structures, which might have grown into arcs if not the current pulse had ended. The authors suggest the filamentation to be a consequence of an insufficient pre-ionisation, which is supported by the results of modelling by Akashi et al. [28].

## References

- [1] **J.T. Verdeyen**, *Laser electronics*, Prentice Hall, New Jersey, 2nd edition (1989).
- [2] **M. Maeda, T. Nishitarumizu and Y. Miyazoe**, *Formation and quenching of excimers in low-pressure rare-gas/halogen mixtures by e-beam excitation*, Jpn. J. Appl. Phys. **18** (3), 439–445 (1979).
- [3] **S. Nagai, M. Sakai, H. Furuhashi, A. Kono, T. Goto and Y. Uchida**, *Effects of  $F^-$  ions and  $F_2$  molecules on the oscillation process of a discharge-pumped ArF excimer laser*, IEEE J. Quantum Electron. **34** (1), 40–46 (1998).
- [4] **H. Akashi, Y. Sakai and H. Tagashira**, *Modelling of a self-sustained discharge-excited ArF excimer laser*, J. Phys. D: Appl. Phys. **27**, 1097–1106 (1994).
- [5] **A.M. Boichenko, V.I. Derzhiev, A.G. Zhidkov and S.I. Yakovlenko**, *Kinetic model of an ArF laser*, Sov. J. Quantum Electron. **22** (5), 444–448 (1992). [Kvantovaya Elektron. **19**, 486–491 (1992)].
- [6] **M. Ohwa and M. Obara**, *Theoretical evaluation of the buffergas effects for a self-sustained discharge ArF laser*, J. Appl. Phys. **63** (5), 1306–1312 (1988).
- [7] **H.H. Michels, R.H. Hobbs and L.A. Wright**, *The electronic structure of ArF and Ar<sub>2</sub>F*, Chem. Phys. Lett. **48** (1), 158–161 (1977).
- [8] **Yu.A. Kudryavtsev and N.P. Kuzmina**, *Excimer gas-discharge tunable ArF laser*, Appl. Phys. **13**, 107–108 (1977).
- [9] **M. Rokni, J.H. Jacob, J.A. Mangano and R. Brochu**, *Formation and quenching kinetics of ArF\**, Appl. Phys. Lett. **31** (2), 79–82 (1977).
- [10] **H. Akashi, Y. Sakai and H. Tagashira**, *Modelling of a self-sustained discharge-excited ArF excimer laser: the influence of photo-ionization and photodetachment by laser light on the discharge development*, J. Phys. D: Appl. Phys. **28**, 445–451 (1995).
- [11] **R. Burnham and N. Djeu**, *Ultraviolet-preionized discharge-pumped lasers in XeF, KrF and ArF*, Appl. Phys. Lett. **29** (11), 707–709 (1976).
- [12] **T.R. Loree, K.B. Butterfield and D.L. Barker**, *Spectral tuning of ArF and KrF discharge lasers*, Appl. Phys. Lett. **32** (3), 171–173 (1978).
- [13] **R.C. Sze and T.R. Loree**, *Experimental studies of a KrF and ArF discharge laser*, IEEE J. Quantum Electron. **14** (12), 944–950 (1978).
- [14] **J. Ringling, O. Kittelmann, F. Noack, U. Stamm, J. Kleinschmidt and F. Voss**, *High-repetition-rate high-power femtosecond ArF laser source*, Opt. Lett. **19** (20), 1639–1641 (1994).
- [15] **M.F. Golde**, *Interpretation of the oscillatory spectra of the inert-gas halides*, J. Mol. Spectr. **58**, 261–273 (1975).
- [16] **A.E. Greene and C.A. Brau**, *Theoretical studies of UV-preionized transverse discharge KrF and ArF lasers*, IEEE J. Quantum Electron. **14** (12), 951–957 (1978).



- [17] **T. Saito and S. Ito**, *Gas contaminant effect in a discharge-excited ArF excimer laser*, Appl. Phys. B **66**, 579–583 (1998).
- [18] **T. Saito, S. Ito and A. Tada**, *Long lifetime operation of an ArF-excimer laser*, Appl. Phys. B **63**, 229–235 (1996).
- [19] **S. Ito, T. Saito and A. Tada**, *A new gas purifier for ArF excimer lasers*, Rev. Sci. Instrum. **67** (3), 658–661 (1996).
- [20] **A.J. Palmer**, *A physical model on the initiation of the atmospheric-pressure glow discharges*, Appl. Phys. Lett. **25** (3), 138–140 (1974).
- [21] **J.I. Levatter and S.C. Lin**, *Necessary conditions for the homogeneous formation of pulsed avalanche discharges at high gas pressures*, J. Appl. Phys. **51** (1), 210–222 (1980).
- [22] **N. Brenning, I. Axnäs, J.O. Nilsson and J.E. Eninger**, *High-pressure pulsed avalanche discharges: formulas for required preionization density and rate for homogeneity*, IEEE Tr. Plasma Sci. **25** (1), 83–88 (1997).
- [23] **S. Nagai, H. Furuhashi, A. Kono, Y. Uchida and T. Goto**, *Measurement of temporal behaviour of electron density in a discharge-pumped ArF excimer laser*, IEEE J. Quantum Electron. **34** (8), 942–948 (1998).
- [24] **P.J. Chantry**, *Negative ion formation in gas lasers*, In: Applied Atomic Collision Physics, E.W. McDaniel and W.L. Nighan, eds., volume 3, Gas Lasers, 35–70, Academic Press, New York, NY, (1982).
- [25] **K.J. Nygaard, S.R. Hunter, J. Fletcher and S.R. Foltyn**, *Electron attachment in dilute fluorine-helium mixtures*, Appl. Phys. Lett. **32** (6), 351–353 (1978).
- [26] **J. Coutts and C.E. Webb**, *Stability of transverse self-sustained discharge-excited long-pulse XeCl lasers*, J. Appl. Phys. **59** (3), 704–710 (1986).
- [27] **M.J. Kushner**, *Microarcs as a termination mechanism of optical pulses in electric-discharge-excited KrF excimer lasers*, IEEE Tr. Plasma Sci. **19** (2), 387–399 (1991).
- [28] **H. Akashi, Y. Sakai and H. Tagashira**, *Modelling of a micro-streamer initiation and development of ArF excimer laser discharges*, Aust. J. Phys. **50**, 655–669 (1997).
- [29] **R. Dreiskemper, G. Schröder and W. Böttcher**, *Light emission during cathode sheath formation in preionized high-pressure glow discharges*, IEEE Tr. Plasma Sci. **23** (2), 180–187 (1995).
- [30] **R. Dreiskemper and W. Böttcher**, *Current filamentation of strongly preionized high pressure glow discharges in Ne/Xe/HCl mixtures*, IEEE Tr. Plasma Sci. **23** (6), 987–995 (1995).
- [31] **M. Makarov**, *Effect of electrode processes on the spatial uniformity of the XeCl laser discharge*, J. Phys. D: Appl. Phys. **28**, 1083–1093 (1995).
- [32] **M. Makarov and Yu. Bychkov**, *The dynamics of XeCl discharge contraction*, J. Phys. D: Appl. Phys. **29**, 350–363 (1996).

- 
- [33] **M. Makarov, J. Bonnet and D. Pigache**, *High efficiency discharge-pumped XeCl laser*, Appl. Phys. B **66**, 417–426 (1998).
  - [34] **R.S. Taylor**, *Preionization and discharge stability study of long optical pulse duration UV-preionized XeCl lasers*, Appl. Phys. B **41**, 1–24 (1986).
  - [35] **O. Uteza, Ph. Delaporte, B. Fontaine, B. Forestier, M. Sentis and I. Tassy**, *Influence of cathode roughness on discharge homogeneity of a high-pulse repetition frequency long-pulse XeCl laser*, Appl. Phys. B **67**, 185–191 (1998).
  - [36] **T. Müller**, *Zeitliche Entwicklung und Filamentierung von KrF<sup>\*</sup>-Lasergasentladungen*, PhD thesis, Technische Hochschule Darmstadt, Darmstadt, Germany (1992). (In German).
  - [37] **J.C.M. Timmermans**, *Double discharge XeCl-laser*, PhD thesis, University of Twente, Enschede, The Netherlands (1995).
  - [38] **T.Y. Chang**, *Improved uniform-field electrode profiles for TEA laser and high-voltage applications*, Rev. Sci. Instrum. **44** (4), 405–407 (1973).
  - [39] **E.A. Stappaerts**, *A novel analytical design method for discharge laser electrode profiles*, Appl. Phys. Lett. **40** (12), 1018–1019 (1982).
  - [40] **G.J. Ernst**, *Uniform-field electrodes with minimum width*, Opt. Comm. **49** (4), 275–277 (1984).

## Chapter 3

# The X-ray source

In section 2.2 the necessity of pre-ionisation of the laser gas mixture has been pointed out. In this chapter we describe, after a short introduction, the experimental set-up of the X-ray source and the results of some experiments which characterise the source.

Pre-ionisation may be done by several methods:

- Injection of electrons.
- Injection of other particles, e.g.  $\alpha$ -particles.
- Irradiation with UV radiation.
- Irradiation with X-rays.

All methods have their specific advantages and disadvantages.

Pre-ionisation of excimer lasers is usually performed by UV radiation, either from a corona discharge behind a screen electrode or, more often, from spark-plugs next to the discharge area, see also chapter 4. The advantage of UV pre-ionisation is its relative simplicity. The main drawback is that the pre-ionisation usually is not very homogeneous as the penetration depth of the radiation is rather low, and the source of the radiation inhomogeneous;

- If the pre-ionisation is done by sparkplugs, the UV is generated from a number of localised sources.

- In the case of behind-the-screen UV-pre-ionisation the radiation has to pass a mesh electrode, which blocks part of the radiation.

During the discharge a screen- or a mesh electrode disturbs the discharge homogeneity as well, because of its non-uniformity. Furthermore, the debris of the sparkplugs or of the corona source contaminates the discharge gas.

Pre-ionisation by X-rays does not have these disadvantages. X-ray photons have a high energy and a large penetration depth. An additional advantage is that an X-ray source may be constructed to irradiate the discharge volume through a solid laser electrode, leading both to a more homogeneous pre-ionisation density and a more homogeneous electric field in the discharge volume. The X-ray source may even be built separate from the laser head and the discharge system, if the two are separated by a window which is transparent for the X-rays. The X-ray pre-ionisation can be collimated rather easily, in order to pre-ionise only the discharge area and not the entire gas volume. This increases the efficiency of the pre-ionisation and of the entire laser [1].

It has been shown that sharp boundaries can be allowed when defining the pre-ionisation window [2], and that the intensity profile of the laser beam can be controlled by detailed manipulation of the pre-ionisation density [3]. Furthermore, with sharply defined discharge boundaries flat electrodes may be used, instead of profiled electrodes that are more difficult to make, more expensive and less effective in the use of the optical gain volume [4–6].

Therefore, X-rays have been chosen as the pre-ionisation method for our ArF-laser.

### 3.1 Experimental set-up

The X-ray source consists of a high voltage cathode from which electrons are accelerated towards an anode. When the electrons strike the anode they are decelerated, producing the X-rays.

We used a corona-plasma cathode [7,8] to generate a high voltage, high density plasma from which electrons can be drawn easily. The cathode consists of a 62 cm long glass tube, with an outer diameter of 10 mm and a thickness of 1.5 mm. The tube is covered with a 58 cm long, 50  $\mu\text{m}$  thick brass foil, see Fig 3.1. A 0.1 mm diameter tungsten wire is wound around the tube and the brass foil. In the foil a window of approximately  $56 \times 1 \text{ cm}^2$  width is cut, so that the wire is in contact with the

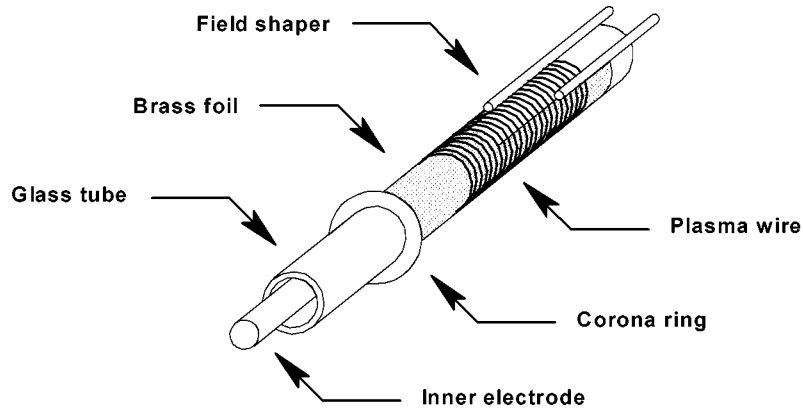


*Figure 3.1: A cut-away overview of the corona-plasma cathode. The inner electrode is placed inside a glass tube. The tube is almost completely covered with a brass foil. The foil ends with corona rings and it is wound with a tungsten wire. The window in the brass foil is framed along its entire length by field shaping rods (only partially shown). During the operation a high voltage pulse is applied to the brass foil and the wires. The inner electrode is connected to the ground via a separate capacitor.*

glass. The foil is ended with 5 mm thick corona rings. Along the entire length of the foil two brass rods of 5 mm diameter are soldered, aligned with the edges of the window. Inside the glass tube is a brass rod of the same length as the foil, serving as an internal electrode so that the entire structure acts as a cylindrical capacitor. The rod is pushed against the top of the glass tube by a narrow strip of mylar underneath it. The entire structure rests on two PVDF supports at an anode-cathode distance of 10 mm, see figure 5.1 on page 60.

During the operation of the corona-plasma cathode the foil is pulse charged to a negative high voltage, while the inner electrode remains at a lower potential. This causes high field gradients around the wires generating a corona, from which electrons are drawn towards the glass. Upon striking the glass the electrons create a plasma from which electrons are expelled towards the anode, see figure 3.2. The brass rods along the window help focussing the electron beam.

The internal brass rod is grounded via a capacitor  $C_{\text{div}}$ . The resulting capacitive

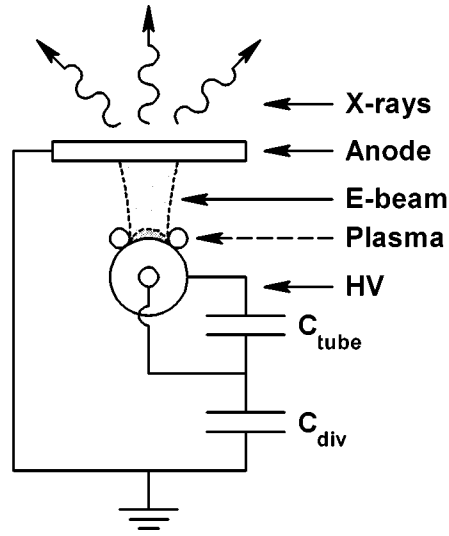


Figure 3.2: Schematic set-up of the X-ray source. The corona tube, with a natural capacitance  $C_{tube}$  is charged to a negative high voltage. The inner electrode is capacitively connected to the ground via a capacitor  $C_{div}$ . The anode is grounded directly. At the window in the brass foil a plasma is created, from which an electron beam is expelled towards the anode where the X-rays are generated. The X-rays are transmitted through the anode.

division with the capacitance of the glass tube lowers the voltage difference across the glass compared to a directly grounded inner electrode, which reduces the risk of a breakdown through the glass, thus extending the lifetime of the cathode considerably [7].

The voltage difference across the glass tube  $V_{tube}$  is given by:

$$V_{tube} = V_{foil} \frac{C_{div}}{C_{div} + C_{tube}}, \quad (3.1)$$

where  $V_{foil}$  is the voltage applied to the foil. The natural capacitance of the cathode

can be estimated using

$$C_{\text{tube}} = 2\pi\epsilon_0\epsilon_{\text{glass}} \frac{l}{\ln\left(\frac{r_{\text{out}}}{r_{\text{in}}}\right)}. \quad (3.2)$$

Where  $\epsilon_0$  is the dielectric permittivity of free space and  $\epsilon_{\text{glass}}$  the relative permittivity of the glass. Taking  $l = 58$  cm,  $r_{\text{out}} = 5$  mm,  $r_{\text{in}} = 3.5$  mm,  $\epsilon_0 = 8.85 \cdot 10^{-12}$  F/m and  $\epsilon_{\text{glass}} = 5$  [9], we find  $C_{\text{tube}} = 452$  pF.

$C_{\text{div}}$  is made of three 0.2 nF, 40 kV max. capacitors in series, so  $C_{\text{div}} = 67$  pF. Thus  $V_{\text{tube}} = 0.13 \cdot V_{\text{foil}}$ . Since  $V_{\text{foil}} = V_X$ , the X-ray driving voltage, and  $V_X \approx 70$  kV,  $V_{\text{tube}} \approx 9$  kV, which is high enough to generate a corona plasma [10].

The corona plasma, from which the electrons are drawn, grows towards the anode during the high voltage pulse with a velocity  $v_p$ , therefore the voltage pulse must be shorter than  $d_0/v_p$  to prevent a short-circuiting of the source. The plasma surface acts as a virtual cathode, whose area  $A_p$  is determined by the cathode area  $A_{\text{cath}}$ , the anode area  $A_{\text{an}}$ , the inter-electrode distance  $d_0$  and by the plasma velocity  $v_p$  [11]:

$$A_p = \frac{v_p}{d_0} (A_{\text{an}} - A_{\text{cath}}) t + A_{\text{cath}}. \quad (3.3)$$

The current through the plasma  $I_X(t)$  is space-charge limited according to the Child-Langmuir law,

$$I_X(t) = \frac{4}{9}\epsilon_0 \sqrt{\frac{2e}{m}} \frac{V_X^{3/2}}{(d_0 - v_p t)^2} A_p, \quad (3.4)$$

in which  $e$  and  $m$  are the electron charge and mass respectively,  $V_X$  is the cathode voltage and  $A_p$  is the effectively emitting electrode area, given by equation 3.3.

Once the electrons strike the surface of the anode they are decelerated, producing X-rays. The emitted X-ray spectrum consists of material-specific frequencies, but the most important factor is the continuous Bremsstrahlung, with an energy spectrum between 0 and  $eV_X$  according to

$$E_X(\epsilon) = \alpha \int_0^{d_0/v_p} \frac{I_X(t)}{eA_{\text{an}}} Z(eV_X - \epsilon) dt, \quad (3.5)$$

where  $\epsilon$  is the X-ray photon energy,  $\alpha = 1.13 \cdot 10^{10} \text{ J}^{-1}$  [11] and  $Z$  is the atom number of the material of the cathode. The total emitted X-ray energy is given by

$$E_X = \int_0^{\epsilon V_X} E(\epsilon) d\epsilon, \quad (3.6)$$

which means that

$$E_X \propto I_X V_X^2 \propto V_X^{7/2}. \quad (3.7)$$

Since the emitted X-ray energy is not only proportional to the atomic number  $Z$  of the anode material but to the transmission characteristics of the anode as well, we use a thin ( $20 \pm 5 \mu\text{m}$ ) tungsten layer ( $Z_W = 74$ ) as the decelerating target material. The tungsten layer is flame-sprayed on an aluminium sheet, which has a low X-ray absorption ( $Z_{Al} = 13$ ). The anode doubles as a pressure window between the vacuum of the X-ray source and the high pressure of the gas mixture inside the laser chamber. In the 1 cm thick aluminium anode a  $60 \times 2 \text{ cm}^2$  groove is milled down to 1 mm thickness to minimise the absorption of the X-rays, whilst at the same time keeping the structure strong enough to withstand the pressure difference, e.g. see figure 5.1. The tungsten layer on the underside of the anode only covers the area of the groove in the upper side.

## 3.2 Characterisation of the X-ray source

The X-ray source is operated with a mini-marx generator, equal to the one delivering the pre-pulse. The mini-marx is described in appendix A. The cathode voltage is measured with a resistive probe [11, 12].

The X-ray intensity is measured with a NE102A fast plastic scintillator, consisting of polyvinyl toluene. The scintillating block of  $1 \times 2 \times 2 \text{ cm}^3$  is wrapped in  $50 \mu\text{m}$  thick aluminium foil for shielding and the visible light is measured via an optical fiber with a Hamamatsu R763 photomultiplier inside the measuring Faraday cage.

Typical wave forms of the measured cathode voltage  $V_X$  and the X-ray intensity are shown in figure 3.3. Since the X-ray intensity profile closely follows the cathode voltage signal  $V_X$ , the voltage signal can be used as an accurate indicator of the X-ray source performance.



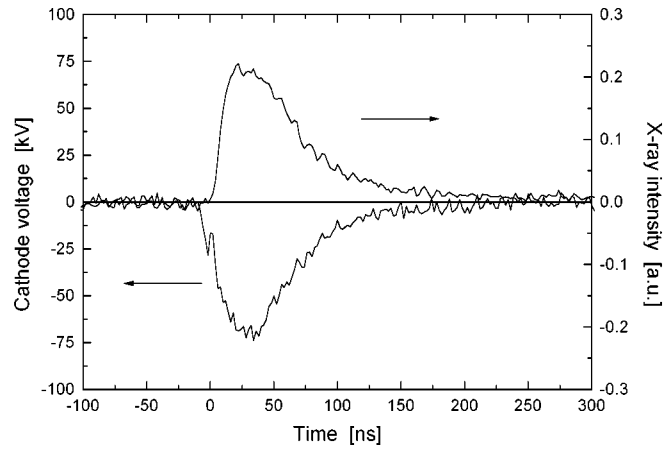


Figure 3.3: Typical wave forms of the X-ray source. Upper trace: X-ray intensity (photomultiplier signal). Lower trace: The cathode voltage  $V_X$ . Mini-marx charging voltage  $V_{XP} = 28$  kV.

When using the X-source the chamber is continuously pumped with a turbo-molecular pump, resulting in a pressure inside the source of approximately  $3 \cdot 10^{-6}$  mbar. Although a higher pressure inside the source can be beneficial for high repetition rate operation of the source [7], a pressure of  $\gtrsim 1 \cdot 10^{-4}$  mbar caused the voltage and current signals of the source to oscillate, indicating a plasma closure inside the source.

The longitudinal X-ray intensity profile was measured at charging voltages of the mini-marx of 20 kV and 25 kV, with the scintillator placed flat inside the groove of the X-ray anode to fix its transverse position. The transverse intensity profile was measured on top of the laser anode, with the scintillator placed upright to obtain a better spatial resolution. The results are shown in figure 3.4.

From figure 3.4 it can be seen that the longitudinal profile of the source has a variation of less than 6 percent along a length of 50 cm. However, the local average intensity is slightly lower at the right side of the profile than on the left side. This is probably caused by a slight unparallelism of the X-ray source electrodes. The transverse

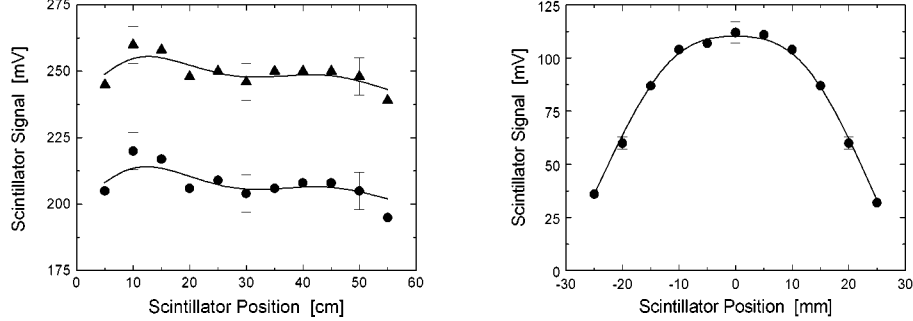


Figure 3.4: The X-ray intensity profile. Left panel: The longitudinal profile, measured on top of the X-ray source anode. ▲:  $V_{XP} = 25$  kV. ●:  $V_{XP} = 20$  kV. Right panel: The transverse profile, measured on top of the laser anode, relative to the optical axis.  $V_{XP} = 20$  kV.

intensity profile has a 2 cm wide top with a variation of less than 5 % and smoothly decaying edges.

The X-ray dosage has been measured with Physiotechnie SEQ6 pyro-electric pen dosimeters. The X-ray dose is found to be 90 mRad directly on top of the X-ray source anode and 25 mRad at the discharge volume at a mini-marx charging voltage of 25 kV.

### 3.3 Pre-ionisation electron density measurements

To measure the electron density generated by the X-ray pulse in the laser gas mixture we used the laser chamber as a charge collector [5, 8, 11]. The laser electrodes are incorporated in a current loop with a storage capacitor  $C_{stor}$  and a measuring resistor  $R_{meas}$ , see figure 3.5. The laser cathode is charged continuously by a *positive* DC-voltage. For the sake of clarity, we will continue to refer to the electrode as the laser cathode, although it acts as an anode during these experiments.

When the X-ray pulse is fired, the resulting electrons in the gas mixture in the laser

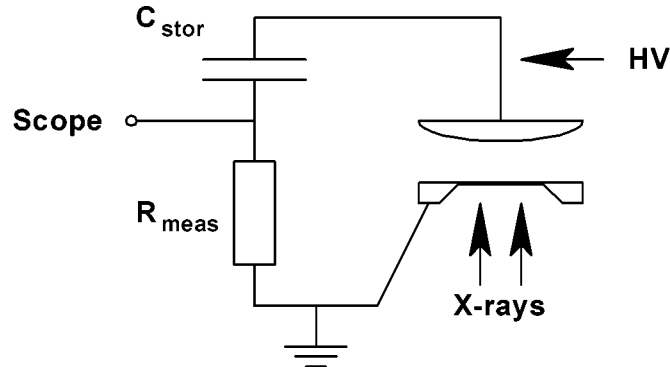


Figure 3.5: The experimental set-up for the pre-ionisation electron density measurement. *HV*: Charging circuit.  $C_{\text{stor}}$ : Storage capacitor, 2.7 nF.  $R_{\text{meas}}$ : Measuring resistor, 1 M $\Omega$ . Scope: Oscilloscope in Faraday cage.

chamber move towards the laser cathode under the influence of the applied electrical field. This results in a current that may be monitored by the voltage across the resistor  $R_{\text{meas}}$ .

The capacitor  $C_{\text{stor}}$  is merely used to separate the oscilloscope from the high voltage of the laser cathode. The minimum capacitance is determined by the expected number of generated electrons; it must be high enough to prevent the voltage across the laser electrodes from being influenced by the pre-ionisation electron current. An estimated pre-ionisation electron density of  $10^8 \text{ cm}^{-3}$  in a volume of  $100 \text{ cm}^3$  and allowing a voltage difference of 10 V yields  $C_{\text{stor}} > 1 \text{ nF}$ . In our set-up  $C_{\text{stor}} = 2.7 \text{ nF}$ .

The  $RC$ -time of the measuring circuit must be much shorter than the electron transition time, which is expected to be several  $\mu\text{s}$  [5,11]. The capacitance of the measuring circuit is the replacement value of  $C_{\text{stor}}$  and the parallel parasitic capacitance of the set-up, which is approximately 40 pF. Using a  $50 \Omega$  terminated standard coaxial cable for the measurements thus ensures a sufficiently fast response.

The measuring circuit of  $C_{\text{stor}}$  and  $R_{\text{meas}}$  was fitted inside a metal box for electrical shielding.

The generated electron density may be accurately measured if the electron transition time is much longer than the pre-ionisation pulse length and if the electron losses due

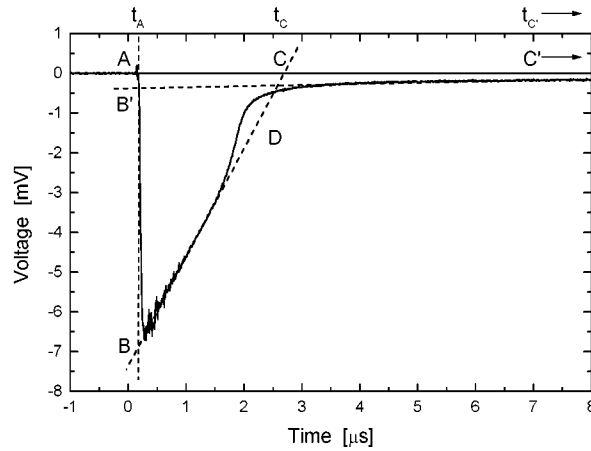


Figure 3.6: Voltage pulse showing several properties of a pre-ionisation electron density measurement. 4 bar Ar.  $V_{XP} = 28$  kV. Laser cathode voltage  $V_{cath} = 3.0$  kV.

to ionic recombination or electron attachment can be neglected. The electron losses may be balanced to a certain extent by applying a sufficient voltage difference across the pre-ionised region. However, care must be taken to prevent electron avalanching, see section 2.2. In the case of a properly tuned system the measured voltage wave form has a triangular shape, whose area corresponds to the number of generated electrons according to equation 3.7. Superimposed on the signal is a longer pulse with a lower amplitude, generated by the current which is carried by the slow moving ions. Both voltage pulses have the same area, since the number of charge-carriers must be equal.

The wave form shown in figure 3.6 shows several properties of the measurement:

- The near instantaneously applied pre-ionisation (at this time scale).
- The triangular shape of the electron current pulse  $\triangle ABC$ .
- The triangular shape of the ionic current pulse  $\triangle AB'C'$ .

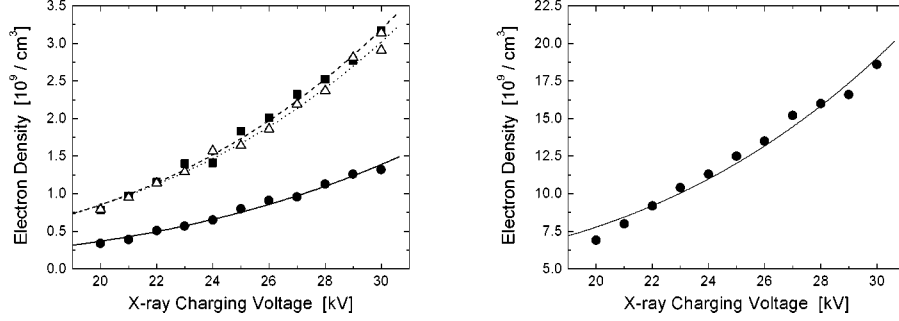


Figure 3.7: The generated electron densities in noble gases and noble gas mixtures at 4 bar total pressure. Left panel:  $\blacksquare$ : He:Ar = 95.0:5.0.  $\triangle$ : He:Ne:Ar = 92.5:5.0:2.5.  $\bullet$ : Pure He. Right panel:  $\bullet$ : Pure Ar. The curves are  $V_X^{7/2}$  fits through the data, see equation 3.7. Note the different vertical scales. Charging voltage  $V_{XP} = 28$  kV Collector voltage  $V_{coll} = 2.0$  kV.

- The drift velocity of the electrons  $d_{el}/(t_C - t_A)$ , with  $d_{el}$  the electrode separation.
- The drift velocity of the ions  $d_{el}/(t_{C'} - t_A)$ .
- A deviation of the triangular shape of the electron pulse near point  $D$ , due to electron losses that are insufficiently balanced by the applied voltage difference.

The pre-ionisation effectiveness of the X-ray pulse depends on the attenuation of the radiation, which can be described by a Lambert-Beer type law [11]:

$$E(\epsilon, x) = E(\epsilon, 0) e^{-\mu(\epsilon)x} \quad (3.8)$$

where  $E(\epsilon, 0)$  is the incident radiant energy of photons with energy  $\epsilon$ ,  $E(\epsilon, x)$  is the remaining photon energy after a travelled distance  $x$  through the absorbing medium and  $\mu(\epsilon)$  is the total linear energy absorption of the medium for photons with energy  $\epsilon$ . For a mixture consisting of several components the resulting mass attenuation

Gas	$W$ [eV]
He	46.0
Ne	36.8
Ar	26.4
Kr	24.1
Xe	21.9

Table 3.1: The radiant energy losses  $W$  of the ionisation of the noble gases. Data taken from ref. [13].

coefficient can be estimated via the mixture rule:

$$\frac{\mu(\epsilon)}{\rho} = \sum_i f_i \frac{\mu_i(\epsilon)}{\rho_i} \quad (3.9)$$

with  $\rho_i$  the total density of the component  $i$  and  $f_i$  its weight fraction.

The radiant energy losses for the creation of an electron-ion pair for the noble gases are given in table 3.1.

The behaviour predicted by the mixture rule [Eq. 3.9] and by the Child-Langmuir law [Eq. 3.7] can be found in figure 3.7, which shows the generated electron density in several noble gases and noble gas mixtures. It is clear from the figure that in pure argon ten times more electrons are produced than in helium and that a small addition of a heavy noble gas in He indeed increases the generated electron density considerably. The gas mixture of He:Ne:Ar = 92.5:5.0:2.5 corresponds to the noble gas composition of the laser gas mixture used in the experiments of chapter 5.

Since the attachment of the electrons to fluorine occurs at a time scale of a few ns [14] it is interesting to calculate the effective pre-ionisation electron density when fluorine is present in the gas mixture. Neglecting diffusion and recombination, the temporal evolution of the electron density  $n_e$  may be described by

$$\frac{dn_e}{dt} = S_0 - \beta n_e n_{F_2} \quad (3.10)$$

where  $S_0$  is the electron production rate of the X-ray source,  $\beta$  is the attachment rate and  $n_{F_2}$  is the fluorine concentration in the gas mixture [2,15]. Taking  $S_0$  to be constant, we obtain

$$n_e = \frac{S_0}{\beta n_{F_2}} \left(1 - e^{-\beta n_{F_2} t}\right). \quad (3.11)$$

From figures 3.3 and 3.7 we may approximate  $S_0 \approx 3 \cdot 10^9 / 150 = 2 \cdot 10^{16} \text{ cm}^{-3} / \text{ns}$  for the He:Ne:Ar mixture. Taking  $\beta = 10^{-9} \text{ cm}^3 / \text{s}$  [14,16] and a fluorine concentration of 6 mbar (as in chapter 5) we get  $1/\beta n_{\text{F}_2} \approx 6 \text{ ns}$ . Thus the effective pre-ionisation electron density generated by the X-ray source in that case is  $S_0/\beta n_{\text{F}_2} \approx 1.2 \cdot 10^8$ .

For the case of chapter 7 we take 1 mbar  $\text{F}_2$  and we assume a generated electron density of  $n_e \approx 1 \cdot 10^{10} \text{ cm}^{-3}$  for the case of a gas mixture without fluorine. This yields  $S_0 \approx 1 \cdot 10^{10} / 150 = 6.7 \cdot 10^{16} \text{ cm}^{-3} / \text{ns}$  and  $1/\beta n_{\text{F}_2} \approx 37 \text{ ns}$ , giving an effective pre-ionisation electron density of  $S_0/\beta n_{\text{F}_2} \approx 2.5 \cdot 10^9$ .

## References

- [1] **M.M. Turner**, *Relations between preionization density distribution, electrode design, and efficiency in high-pressure discharge-excited gas lasers*, Appl. Phys. Lett. **63** (21), 2866–2868 (1993).
- [2] **R.S. Taylor**, *Preionization and discharge stability study of long optical pulse duration UV-preionized XeCl lasers*, Appl. Phys. B **41**, 1–24 (1986).
- [3] **M.S. Pronko**, *Controlling output gain uniformity by spatial variation of the x-ray preionization in a large-aperture discharge-pumped KrF amplifier*, IEEE J. Quantum Electron. **30** (9), 2147–2156 (1994).
- [4] **F.A. van Goor, W.J. Witteman, J.C.M. Timmermans, J. van Spijker and J. Couperus**, *High average power XeCl laser with x-ray pre-ionization and spiker-sustainer excitation*, In: High-power gas and solid state lasers, M. Bohrer, T. Letardi, D. Schuöcker and H. Weber, eds., Proceedings of SPIE **2206**, 30–40 (1994).
- [5] **J.C.M. Timmermans**, *Double discharge XeCl-laser*, PhD thesis, University of Twente, Enschede, The Netherlands (1995).
- [6] **R.M. Hofstra**, *On the optical performance of the long pulse XeCl\* excimer laser*, PhD thesis, University of Twente, Enschede, The Netherlands (1999).
- [7] **S.J. Scott**, *Development of a long life, 2 kHz repetition rate X-ray preionizer*, Appl. Phys. B **56**, 201–208 (1993).
- [8] **F.A. van Goor**, *Fast rise time x-ray pre-ionization source using a corona plasma cathode*, J. Phys. D: Appl. Phys. **26**, 404–409 (1993).
- [9] **G. Verkerk, J.B. Broens, W. Kranendonk, F.J. van der Puijl, J.L. Sikkema and C.W. Stam**, eds., *BINAS, Informatieboek VWO/HAVO voor het onderwijs in de natuurwetenschappen*, Wolters-Noordhoff, Groningen, The Netherlands (1986). (In Dutch).
- [10] **R.S. Taylor and K.E. Leopold**, *Pre-preionization of a long optical pulse magnetic-spiker sustainer XeCl laser*, Rev. Sci. Instrum. **65** (12), 3621–3627 (1994).

- 
- [11] **J.W. Gerritsen**, *High-efficiency operation of an x-ray preionized avalanche discharge XeCl laser*, PhD thesis, University of Twente, Enschede, The Netherlands (1989).
  - [12] **M. Trentelman**, *Gas discharge excited XeF laser*, PhD thesis, University of Twente, Enschede, The Netherlands (1993).
  - [13] **K. Midorikawa, M. Obara and T. Fujioka**, *X-ray preionization of rare-gas-halide lasers*, IEEE J. Quantum Electron. **20** (3), 198–205 (1984).
  - [14] **P.J. Chantry**, *Negative ion formation in gas lasers*, In: Applied Atomic Collision Physics, E.W. McDaniel and W.L. Nighan, eds., volume 3, Gas Lasers, 35–70, Academic Press, New York, NY, (1982).
  - [15] **M. Steyer and H. Voges**, *Parametric study of x-ray preionized high-pressure rare gas halide lasers*, Appl. Phys. B **42**, 155–160 (1987).
  - [16] **K.J. Nygaard, S.R. Hunter, J. Fletcher and S.R. Foltyn**, *Electron attachment in dilute fluorine-helium mixtures*, Appl. Phys. Lett. **32** (6), 351–353 (1978).



## Chapter 4

# Excitation circuits and modes of operation

When designing an excitation circuit for a discharge pumped laser several factors are important;

- A homogeneous multiplication of the pre-ionisation electron density.
- A high voltage for the breakdown of the discharge.
- A short current rise time.
- A high total current density.
- The pumping voltage should be matched to  $V_{SS}$  during the stable phase of the discharge.
- A high energy efficiency.
- As little current ringing as possible after the discharge.
- Reliable and reproducible operation.
- A good optical quality.

Some of these factors depend on the geometrical properties of the discharge unit, most are depending on the excitation circuit.

In order to operate a gas discharge laser a homogeneous electrical gas discharge has to be created. To do so, voltages of several tens of kilovolts, and currents of up to tens of kiloamperes must be switched rapidly and reproducibly, preferably at several hundreds of pulses per second. This calls for special switches.

The simplest form of a high voltage switch is a spark-gap. It consists of two conductors, placed a short distance apart in a gas. When a high voltage difference is applied over the gap, the gas breaks down in one or more arcs, allowing high currents to pass. The switching parameters of a spark gap can be manipulated by the shape of the electrodes, the interelectrode gap, and the type and pressure of the gas between the electrodes.

However, since the triggering of a spark gap relies on the formation of arcs, which is a statistical process, spark gaps inherently show a time jitter in their switching. The electrode material also erodes from sputtering at each shot. This makes spark gaps unfit for operation at a high repetition rate and unsuitable if a high reliability is needed. For these purposes saturable inductors are a better choice.

In this chapter an overview is given of different circuits and modes of operation for the excitation of a gas discharge pumped laser. In the first few sections, circuits based on spark-gap switches are described. Then, after a short introduction to the properties of saturable inductors, several circuits operating with saturable inductors are treated.

In chapter 5 the experimental results of the circuits are discussed.

## 4.1 Charge-Transfer mode

The simplest way to pump a laser gas discharge is by discharging a capacitor through a pre-ionised gas in a so-called charge-transfer system.

A rather efficient form of the charge transfer circuit is shown in figure 4.1 [1]. It is operated by pulse charging the storage capacitor  $C_{\text{stor}}$  by some main circuit. The voltage on  $C_{\text{stor}}$  causes the spark-plugs  $S$ , which are positioned alongside the laser electrodes, to break down into arcs. This allows a current from  $C_{\text{stor}}$  to charge the pulse capacitor  $C_{\text{P}}$  while at the same time pre-ionising the discharge volume by the UV radiation produced by the spark plugs. If the voltage on  $C_{\text{P}}$  is high enough, this causes the pre-ionised gas between the laser electrodes to break down. After the gas breakdown the laser is excited by the energy stored on  $C_{\text{P}}$ .

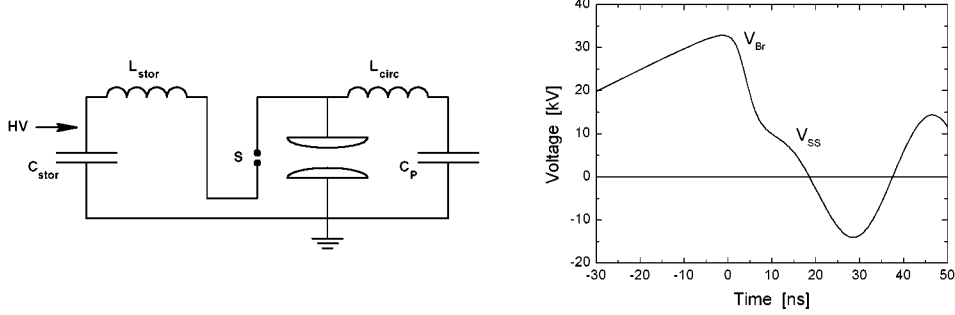


Figure 4.1: The automatically UV-spark pre-ionised charge transfer circuit and the resulting voltage pulse. *HV*: Charging circuit.  $C_{\text{stor}}$ : Storage capacitor.  $L_{\text{stor}}$ : Self-inductance of the storage circuit. *S*: Spark gap switch. The UV-radiation produced by the sparks pre-ionises the discharge volume.  $L_{\text{circ}}$ : Self-inductance of the discharge circuit.  $C_{\text{P}}$ : Pulse capacitor.  $V_{\text{br}}$ : Breakdown voltage of the laser.  $V_{\text{SS}}$ : Steady state voltage.

With this circuit the pre-ionisation always starts at the same time, i.e. at the breakdown of the spark gaps and the onset of the voltage pulse on the electrodes. This results in a predictable operation of the laser, but it inhibits further optimisation of the system.

Gas discharges are preferably operated at the steady state, as defined by equation 2.8 in section 2.2. In that case the voltage across the discharge can be considered constant at  $V_{\text{SS}}$  during the first half cycle of the  $LC$  oscillation of the current through the discharge [2, 3]. The current through the discharge may be written as:

$$I = \sqrt{\frac{C_{\text{P}}}{L_{\text{circ}}}} (V_{\text{C}} - V_{\text{SS}}) \sin\left(\frac{t}{\sqrt{L_{\text{circ}}C_{\text{P}}}}\right). \quad (4.1)$$

Where  $V_{\text{C}}$  is the charging voltage of the pulse capacitor  $C_{\text{P}}$ , and  $L_{\text{circ}}$  is the self-inductance of the discharge circuit. If initially  $V_{\text{C}} = 2V_{\text{SS}}$ , the capacitor  $C_{\text{P}}$  is empty after the first half current oscillation and all electrical energy is transferred to the gas discharge.

However, the breakdown voltage of the discharge gap for optimum operation of such a circuit is much higher than  $2V_{SS}$ . The main disadvantage of the charge transfer circuit is therefore that a single circuit is used to break down the discharge as well as to sustain the laser. Thus, the circuit must be charged with a too high voltage for an efficient transfer of the pumping power to the gas, while the excessively high voltage favours the growth of instabilities as well. Thus, only relatively inefficient, short pulses of  $\tau \lesssim 20$  ns (FWHM) are generated. Nevertheless, the pumping power of this type of laser can be very high, because the self-inductance  $L_{\text{circ}}$  of the discharge circuit can be made very low.

Increasing the capacitance of  $C_P$  causes a longer current pulse, but a longer charging time as well. A longer voltage rise allows more time for the growth of instabilities in the discharge volume. Thus, the discharge quality is reduced, causing a worse performance of the laser.

If the pre-ionisation of the gas mixture is done by an external source,  $C_P$  can be charged before the gas is pre-ionised. When the pre-ionisation pulse is applied the laser gas mixture breaks down in the same manner as described above. If the pre-ionisation is done by X-rays, this operation mode is called the X-ray triggered mode, for obvious reasons.

## 4.2 Church mode

Some lasers make use of the current from the storage capacitor to deliver additional energy to the discharge and so to lengthen the discharge pulse, e.g. see refs. [4, 5]. If the self-inductance of the circuit between the discharge and the storage capacitor is very low,  $C_{\text{stor}}$  can become the main power supply for the discharge instead of  $C_P$  [4]. Especially if  $C_P$  is much smaller than  $C_{\text{stor}}$ , the current from  $C_{\text{stor}}$  to  $C_P$  after the closing of the switch  $S$  causes a short, high voltage overshoot on  $C_P$ . This voltage pulse breaks down the discharge, which is then sustained at a lower voltage by  $C_{\text{stor}}$ , so that the pulse capacitor  $C_P$  has become merely a peaking capacitor.

The advantage of this circuit is that the laser can be operated near voltage matching during the entire pulse, if the circuit parameters such as the capacitances and the inductances are properly chosen.

Such a circuit, using a triggerable switch and X-ray pre-ionisation, is shown in figure 4.2 together with the resulting voltage pulse. The circuit has been called the “church” mode circuit, after the shape of the voltage pulse. The storage capacitor

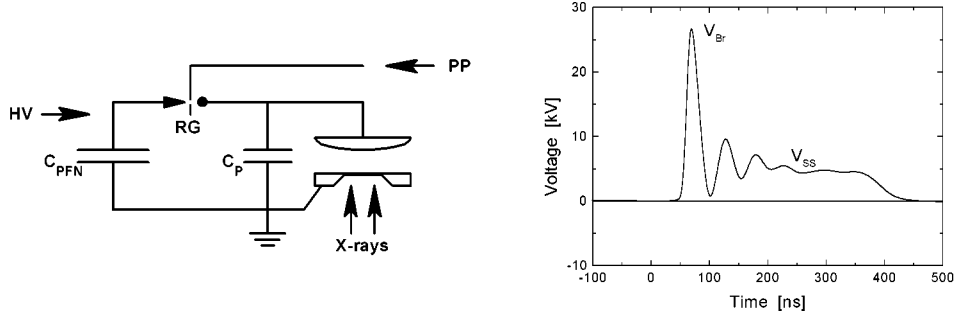


Figure 4.2: The church mode circuit and the resulting voltage pulse. *HV*: Charging circuit.  $C_{\text{PFN}}$ : Pulse Forming Network. *RG*: Rail gap switch with trigger electrode.  $C_{\text{P}}$ : Peaking capacitor. *PP*: Pre-pulse.  $V_{\text{br}}$ : Breakdown voltage of the laser.  $V_{\text{SS}}$ : Steady state voltage.

is built in the form of a Pulse Forming Network (PFN). The switch is a triggerable multi spark rail gap, which is a low inductive spark gap designed to break down in several arcs along its entire length. In our set-up the rail gap is 60 cm long and it usually breaks down in more than ten arcs. The rail gap is operated by applying a high voltage pre-pulse on the trigger electrode inside the rail gap, which causes the rail gap to break down. The current from the PFN to the peaking capacitor then causes the voltage overshoot on  $C_{\text{P}}$  which breaks down the discharge.

However, the PFN voltage  $V_{\text{PFN}}$  needs to be sufficiently high so that the voltage overshoot can cause the breakdown of the laser gas. Since the overshoot voltage is caused solely by the PFN, the maximum voltage is restricted to  $2V_{\text{PFN}}$ . Generally the breakdown voltage of a gas is more than 4 times its steady state voltage, therefore  $V_{\text{PFN}}$  must be considerably higher than the voltage matching value of  $2V_{\text{SS}}$ , which means that this circuit, too, is not ideal.

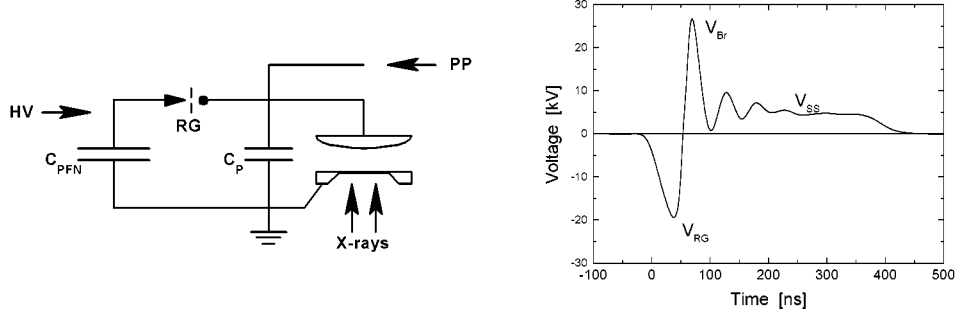


Figure 4.3: The swing mode circuit and the resulting voltage pulse. *HV*: Charging circuit.  $C_{\text{PFN}}$ : Pulse Forming Network. *RG*: Rail gap switch with (unused) trigger electrode.  $C_{\text{P}}$ : Peaking capacitor. *PP*: Pre-pulse.  $V_{\text{RG}}$ : Breakdown voltage of the rail gap.  $V_{\text{br}}$ : Breakdown voltage of the laser.  $V_{\text{SS}}$ : Steady state voltage.

### 4.3 Swing mode

A large difference between the maximum of the voltage overshoot value and  $V_{\text{PFN}}$  can be attained when the rail gap is triggered passively, by means of a high voltage pre-pulse on the peaking capacitor which is delivered by a separate circuit, see figure 4.3 [6]. The pre-pulse is to be applied when the PFN has been fully charged to  $V_{\text{PFN}}$ , either by a continuous source or by a high voltage pulse.

The pre-pulse voltage  $V_{\text{pre}}$  causes a voltage difference of  $V_{\text{PFN}} + V_{\text{pre}}$  across the rail gap, causing it to break down at  $V_{\text{RG}}$ . Because of the large difference between the capacitances of  $C_{\text{P}}$  and  $C_{\text{PFN}}$  the PFN is seen by the peaking circuit as a closed ground-connection. The pre-pulse thus causes a resonant voltage ringing of the peaking circuit, which is superimposed on the PFN voltage  $V_{\text{PFN}}$ . The resonant oscillation has a natural amplitude of  $V_{\text{RG}}$ , thus the maximum voltage on  $C_{\text{P}}$  increases with  $V_{\text{PFN}}$  to  $V_{\text{RG}} + V_{\text{PFN}}$ , which is higher than the laser breakdown voltage  $V_{\text{br}}$ . After the breakdown the discharge is sustained by the current from the PFN. This operation mode has been called the “swing” mode, after the voltage over-swing on the peaking capacitor.

The PFN voltage, the pre-pulse voltage and the rail gap breakdown voltage can be adjusted to match both the laser breakdown voltage and the steady state voltage of the laser discharge. It should be noted that the rail gap breakdown voltage difference is  $V_{\text{PFN}} + V_{\text{RG}}$ , while the peaking capacitors are merely charged to  $V_{\text{RG}}$  by the pre-pulse.

The breakdown voltage of the rail gap  $V_{\text{RG}}$  should be lower than the breakdown voltage of the laser  $V_{\text{br}}$ ; otherwise the laser would be operated in a charge transfer mode with the peaking capacitor, charged by the pre-pulse generator.

However, if the breakdown voltages of the switch and that of the laser are perfectly tuned, the discharge can be ignited by the pre-pulse *and* be sustained by the PFN. In that case the rail gap must break down a little later than the laser discharge, and the peaking circuit must contain sufficient energy to sustain the discharge until the moment the PFN can take matters over. This operation mode is called the “switch” mode, after the switching of the direction of the current through the discharge from the current from  $C_{\text{P}}$  to that of the PFN. Due to the inherently erratic behaviour of a spark gap, it proved nearly impossible to operate the laser in the rail gap-switched switch mode in our set-up. However, with a saturable inductor switch the switch mode is a rather straightforward technique, see section 4.7.

#### 4.4 Resonant Overshoot mode (with a rail gap)

The “resonant overshoot” mode voltage pulse is originally a consequence of the use of saturable inductors, see section 4.6 below. However, simulating the switching behaviour of a saturable inductor proved to be possible by connecting a discrete inductor in parallel with a voltage dependent switch, in the shape of the rail gap. Since the change between different rail gap switched modes takes only a few minutes, while changing between the rail gap and the saturable inductor costs several hours, there is no significant degradation in the laser gas mixture when the rail gap circuits are used and the laser needs not to be re-filled. Thus a good comparison between the different excitation modes with a minimum variation in the other experimental circumstances is allowed.

Basically, the rail gap switched resonant overshoot mode is a modified form of the swing mode, see section 4.3. Comparing the rail gap switched resonant overshoot circuit, shown in Fig. 4.4, with that of the swing mode, figure 4.3, shows that the main difference between the two circuits is the inductor  $L_{\text{RG}}$  bridging the rail gap.

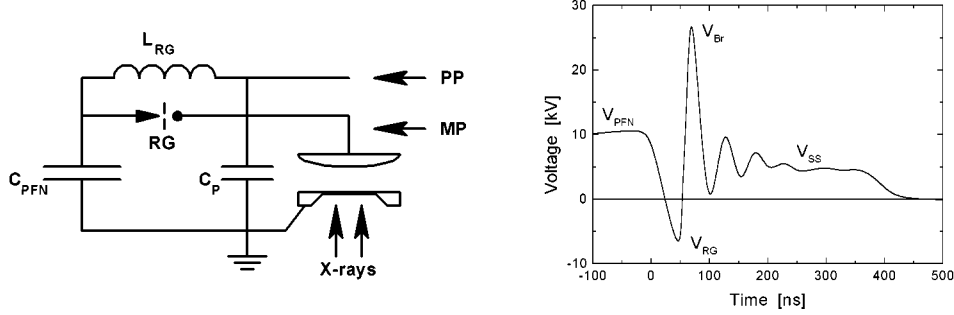


Figure 4.4: The rail gap switched resonant overshoot mode circuit and the resulting voltage pulse.  $C_{\text{PFN}}$ : Pulse Forming Network.  $\text{RG}$ : Rail gap switch with (unused) trigger electrode.  $L_{\text{RG}}$ : Inductor, bridging the rail gap.  $C_{\text{P}}$ : Peaking capacitor.  $\text{PP}$ : Pre-pulse.  $\text{MP}$ : Main pulse, PFN charging pulse. The main pulse can also be applied directly to the PFN, as in the swing mode.  $V_{\text{PFN}}$ : PFN charging voltage.  $V_{\text{RG}}$ : Breakdown voltage of the rail gap.  $V_{\text{br}}$ : Breakdown voltage of the laser.  $V_{\text{SS}}$ : Steady state voltage.

The inductance of  $L_{\text{RG}}$  is chosen so that the oscillation time of the  $\text{CLC}$  circuit of  $C_{\text{PFN}}$ ,  $L_{\text{RG}}$  and  $C_{\text{P}}$  is much larger than the charging time of the peaking capacitor by the pre-pulse, but at the same time it is much shorter than the charging of the PFN. This means that the slow pulse charging of the PFN to  $V_{\text{PFN}}$  is being transferred to the peaking capacitor, causing a simultaneous charging of  $C_{\text{P}}$  and the laser electrodes to  $V_{\text{PFN}}$ , see the voltage pulse in figure 4.4. On the other hand, the characteristics of the charging of  $C_{\text{P}}$  by the pre-pulse circuit are virtually unaltered.

The operation of the resonant overshoot circuit is equivalent to that of the swing mode; once the PFN is fully charged, the pre-pulse is fired, causing the rail gap to break down at  $V_{\text{RG}}$ . The peaking circuit subsequently starts its oscillation with an amplitude of  $V_{\text{RG}}$  on top of  $V_{\text{PFN}}$ , fed by the current from the PFN. The laser breaks down at  $V_{\text{br}}$ , and the discharge is then sustained by the main current from the PFN, flowing through the rail gap. The inductance of  $L_{\text{RG}}$  is much higher than that of the closed rail gap; thus it has no noticeable effect on the current pulse. In a properly tuned circuit it makes no difference in the operation of the laser on which side of  $L_{\text{RG}}$



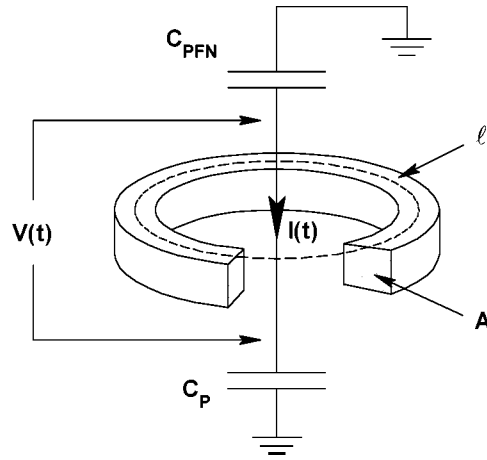


Figure 4.5: Schematic cut-away cross-sectional diagram of a conductor passing through a toroidal core of a saturable magnetic material.  $C_{\text{PFN}}$ : Pulse Forming Network.  $C_{\text{P}}$ : Peaking capacitor.  $V(t)$ : Voltage difference.  $I(t)$ : Current through conductor.  $\ell$ : Magnetic path length.  $A$ : Core cross-sectional area.

the PFN charging circuit is connected.

If the breakdown voltage of the rail gap can be made high enough, it is theoretically possible to operate this circuit also in the switch mode, as explained in sections 4.3 and 4.7. However, with our set-up this proved impossible.

## 4.5 Intermezzo: Saturable inductors

The above described excitation modes rely on spark gaps for the switching of the main current to the laser. Spark gaps have the advantage of a good electrical isolation up to very high voltages and the ability to carry very large currents with very short rise times. However, their triggering is inherently erratic and the electrodes erode with each spark. Therefore spark gaps are not suitable for use at high pulse repetition rates.

For the high pulse repetition rate operation of lasers magnetic switches in the form of

saturable inductors may be used. Saturable inductors, however, do not physically isolate circuit parts. Their operation relies on them acting as a variably sized inductance, thus restraining currents or allowing them to pass.

Consider a core of a magnetic material with a varying voltage  $V(t)$  across it, e.g. the voltage difference between the PFN and the peaking capacitors, see figure 4.5 [2, 7]. The voltage across the core generates a rate of change of the magnetic flux  $\Phi$  linking  $N$  current loops around the core according to Faraday's law

$$V(t) = N d\Phi/dt. \quad (4.2)$$

The total magnetic flux  $\Phi$  is defined as the integral of the magnetic flux density  $B$  over the surface of the core  $A$ ,

$$\Phi = \int_A B \cdot dS. \quad (4.3)$$

Combining equations 4.2 and 4.3 gives:

$$V(t) = -N \frac{d}{dt} \int_A B \cdot dS \quad (4.4)$$

or:

$$\int V(t) dt = -N \int_A B \cdot dS. \quad (4.5)$$

Thus, for a given  $V(t)$ ,

$$V(t) \Delta t = N \Delta B A, \quad (4.6)$$

which means that a voltage difference  $V(t)$ , applied during a time  $\Delta t$  across a core with surface area  $A$ , causes a flux density swing of  $\Delta B$  per current loop around the core. In other words: a voltage difference  $V(t)$  can be kept across a saturable core with surface area  $A$  during a time  $\Delta t$ , determined by the number of current loops around the core  $N$  and the available flux swing  $\Delta B$ .

The magnetic flux density  $B$  in a core with a mean path length  $\ell$  is related to the current through the core  $I(t)$  via the magnetic permeability  $\mu_r$ , relative to the permeability of free space  $\mu_0 \equiv 4\pi \cdot 10^{-7}$  H/m:

$$B = \mu_r \mu_0 N I(t) / \ell = \mu_r \mu_0 H, \quad (4.7)$$

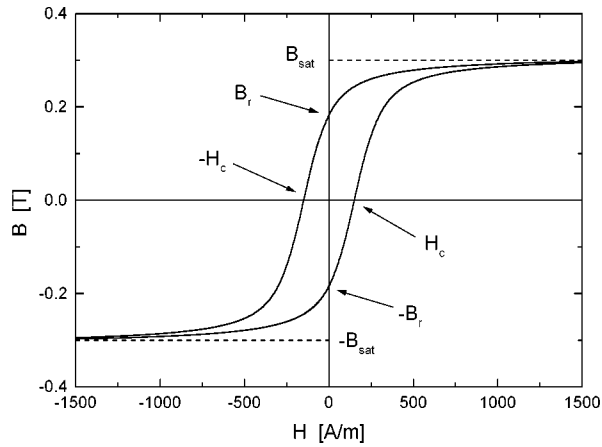


Figure 4.6: Schematic  $BH$ -curve or hysteresis loop of the Ceramic Magnetics CMD 5005 high frequency ferrite.  $H_c$ : Coercive field strength.  $B_r$ : Remanent magnetic field.  $B_{sat}$ : Saturation field.

with  $H$  the applied magnetic field strength.

The value of  $\mu_r$  of a saturable inductor be found from the slope of the  $BH$ -curve or hysteresis loop. The, somewhat simplified, hysteresis loop of the Ceramic Magnetics CMD 5005 high frequency ferrite, which is used in our set-up, is shown in figure 4.6. In the figure the remanent magnetic field for the case of zero current,  $B_r = 0.17$  T, the saturated magnetic field for the case of a high current,  $B_{sat} = 0.3$  T, and the coercive field which must be applied to completely demagnetise the core,  $H_c = 150$  A/m, are indicated.

Combining equations 4.6 and 4.7 with figure 4.6 we can see that the maximum voltage difference that can be kept across the ferrites is determined not only by the behaviour of voltage pulse  $V(t) \Delta t$ , but also by the starting point of the core on the hysteresis loop.

If there is no initial current, the magnetic field inside the core is either  $+B_r$  or  $-B_r$ . Applying a voltage difference across the core causes a small leak-current through the

core. This results in a small  $H$  field, which forces a  $B$  field inside the ferrites, following the hysteresis loop. This allows a little more current to be transported through the core, thus causing a self-increasing effect.

The sign of the voltage difference and the initial state of the core therefore determine whether the available flux-swing is  $B_{av} = (B_{sat} - B_r)$  or  $B_{av} = (B_{sat} + 2B_r)$ .

The self-inductance of a circuit containing a saturable inductor,  $L_{sat.ind}$ , is at all times given by:

$$L_{sat.ind} = \mu_r(t)L_{geom} + L_{rest} \quad (4.8)$$

where  $\mu_r(t)$  is the magnetic permeability of the core at the time  $t$ ,  $L_{geom}$  is the geometrical self-inductance of the core and  $L_{rest}$  is the self-inductance of the remainder of the circuit under consideration. This means that the self-inductance of a saturable core is always a factor  $\mu_r$  higher than its purely geometrical value. In order to keep the geometrical self-inductance of the circuit at a minimum, a long and narrow “racetrack” geometry with a single current loop is used in excimer lasers, optimising the ratio between the area of the current loop and its width.

## 4.6 Resonant Overshoot mode (with a saturable inductor)

In the ferrite-switched resonant overshoot mode circuit the switch between the PFN and the peaking circuit is formed by a saturable inductor  $L_{sat}$ , consisting of ferrites in a racetrack geometry, see figure 4.7. Although the switching behaviour of a saturable inductor is different from that of a rail gap [Sec. 4.5], the operation of the ferrite-switched resonant overshoot mode is equivalent to that of the rail gap-switched resonant overshoot circuit, see section 4.4; once the PFN has been charged, a pre-pulse of opposite polarity to the PFN voltage is applied to the peaking capacitors to break down the switch. The resulting voltage overshoot on the peaking capacitor breaks down the laser gas discharge at a voltage  $V_{br}$ . The discharge is subsequently sustained by the current from the PFN.

The switching voltage of the ferrites is determined by the amount of ferrites used in the switch and the initial setting of the switch.

The voltage pulse of the ferrite-switched resonant overshoot mode and the magnetic core dynamics are shown in figure 4.8. The letters in both panels of figure 4.8 correspond with each other.

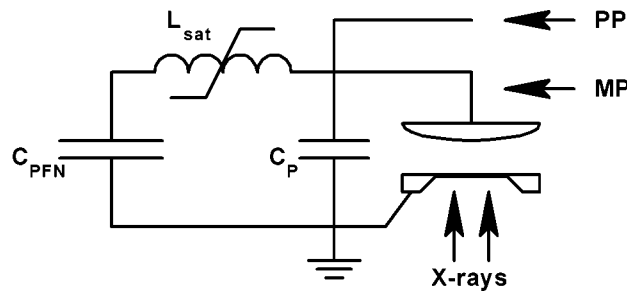


Figure 4.7: The ferrite-switched resonant overshoot mode circuit.  $C_{\text{PFN}}$ : Pulse Forming Network.  $L_{\text{sat}}$ : Saturable inductor (ferrite).  $C_{\text{P}}$ : Peaking capacitor. PP: Pre-pulse. MP: Main pulse, PFN charging pulse.

The PFN is initially charged by a current flowing through the ferrites into the PFN. When the PFN has been fully charged to  $V_{\text{PFN}}$ , the charging current is nearly zero and the magnetic field of the ferrites is set to  $-B_{\text{T}}$ , see position *A* in figure 4.8. The pre-pulse, of opposite polarity to the PFN voltage, generates a voltage difference across the ferrites, which causes the core to move along the  $BH$  curve in the direction of the arrow. At position *B* the inductance of the core for currents flowing from the PFN in the direction of the peaking capacitor is substantially lowered: the switch is closed and the voltage on the peaking capacitor increases again. The current from the PFN to  $C_{\text{P}}$  forces the ferrites further into saturation at position *C*. However, at that point the voltage on the peaking capacitor increases over  $V_{\text{PFN}}$ , which forces the ferrites away from the saturation at *C* to a position *D* at the crest of the voltage where the laser breaks down. At the breakdown of the discharge the voltage on  $C_{\text{P}}$  drops severely, once again becoming lower than  $V_{\text{PFN}}$ , so that the ferrites move back into saturation and the current from the PFN to the laser can increase again, see position *E*. During the operation of the discharge pulse at the steady state voltage  $V_{\text{SS}}$  the ferrites are forced deep into saturation, see position *F*.

The use of saturable inductors for the switching of excimer lasers has its drawbacks. The circuit parameters and the behaviour of the discharge are inextricably intertwined; the current through the laser determines the inductance and the impedance of the switch, which governs the rise time of the current. Both have an influence on the discharge properties, such as its operating voltage and impedance. Also, the in-

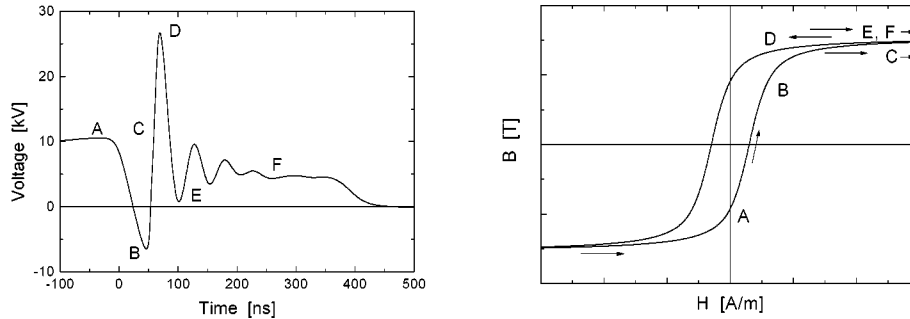


Figure 4.8: The voltage pulse and the properties of the magnetic core of a ferrite switched resonant overshoot mode pulse. The meaning of the letters, which correspond with each other in both figures, is explained in the text.

ductance of the closed switch remains always some three times the geometrical value so that pumping energy is lost. Besides, the inductor does not electrically separate circuit parts, so that extra care must be taken in the design of the circuit. Moreover, during the charging of the PFN miniature electron avalanches may already have been formed, so that the discharge homogeneity may be negatively influenced.

An additional problem may be caused by the following effect: after the pulse the ferrites return to the remanent field at  $B_r$ . Thus, when the next pulse starts, the PFN-charging current is blocked by the ferrites. The result being an initial increase of the voltage on the peaking capacitors until the ferrites are sufficiently saturated to allow the charging of the PFN. When the charging pulse rises too fast, the first voltage peak on  $C_P$  may reach such a level as to cause a spontaneous breakdown of the discharge gap. This not only prevents a 'normal' pulse but it can also damage the set-up.

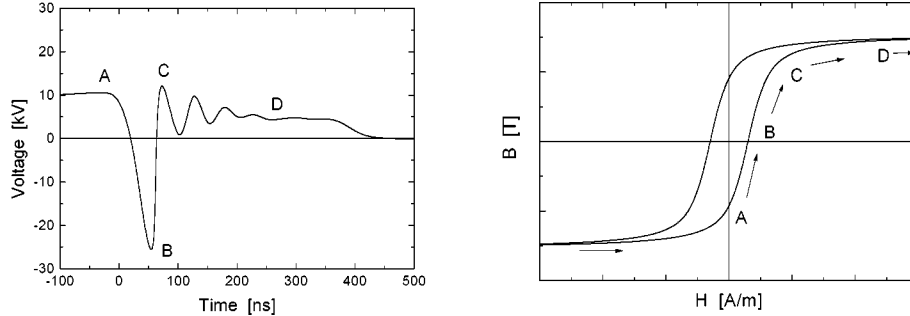


Figure 4.9: The voltage pulse and the properties of the magnetic core of a switch mode pulse. The meaning of the letters, which correspond with each other in both figures, is explained in the text.

## 4.7 Switch mode

Using the same basic circuit as the saturable inductor-switched resonant overshoot mode, the laser may also be operated in the so-called “switch” mode. In that case the amount of ferrite in the switch and the properties of the pre-pulse are to be chosen in such a way that the ferrites only saturate *after* the pre-pulse has ignited the laser gas discharge, so that the laser discharge is started without the use of a voltage overshoot, see also section 4.3.

Although the switch mode voltage pulse resembles the resonant overshoot mode pulse somewhat, the behaviour of the magnetic core is different. The voltage pulse and the core dynamics for the switch mode are shown in figure 4.9.

The PFN is initially charged by a current flowing through the magnetic core into the PFN. When the PFN has been fully charged to  $V_{\text{PFN}}$ , the charging current is nearly zero and the magnetic field of the ferrites is set to  $-B_r$ , see position *A* in figure 4.9. The pre-pulse, of opposite polarity to the PFN voltage, generates a voltage difference across the ferrites, which causes the core to move along the  $BH$  curve in the direction of the arrow. At position *B* the pre-pulse causes the breakdown of the laser gas, so that a current starts flowing from the peaking circuit through the discharge. However,

the ferrites still block the flow of a current out of the PFN. During the first stages of the discharge the voltage on  $C_P$  therefore remains lower than  $V_{\text{PFN}}$ , which causes the ferrites to move along the hysteresis loop to a low core inductance for currents flowing from the PFN so that the switch is closed at position  $C$ . The current from the PFN further sustains the laser at the steady state voltage  $V_{\text{SS}}$ , while forcing the ferrites deep into saturation at position  $D$ .

One of the main differences between the operation of the resonant overshoot mode and the switch mode is that in the switch mode the ferrites traverse the hysteresis loop only in one direction, which decreases energy losses in the ferrites.

Comparing the switch mode with the resonant overshoot mode shows several advantages and disadvantages of both modes. In the resonant overshoot mode the voltage difference across the switch is reversed at the moment of breakdown, which means that there is some time delay between the start-up of the main discharge current and the breakdown of the laser. This time delay is absent in the switch mode.

Although in the switch mode the voltage difference over the saturable inductor is always in the same direction when the pre-pulse has been applied, the laser discharge starts with an electric field of opposite polarity to that of the PFN. Thus the current through the discharge reverses its direction, which causes hot spots to appear at both electrodes [8,9]. This may enhance the formation of discharge instabilities. This effect does not occur in the resonant overshoot mode.

In the switch mode the pre-pulses causes the breakdown of the laser. Thus, the large voltage difference between the laser breakdown voltage and the PFN voltage, usually  $\sim -6V_{\text{SS}}$  and  $\sim +2V_{\text{SS}}$ , respectively, must be switched by the ferrites, which means that a large amount of ferrite is necessary. In the resonant overshoot mode the voltage difference is usually only  $\sim -4V_{\text{SS}}$  and  $\sim +2V_{\text{SS}}$ , respectively, since the breakdown of the laser gas is caused by the voltage overshoot and not solely by the pre-pulse. Therefore less ferrite can be used, which means a lower inductance of the switch and thus the possibility of a higher pumping power than with the switch mode. On the other hand, the current rise time in the switch mode may be shorter than with the resonant overshoot mode, since the current through the switch only flows in one direction.

In addition, the reduced amount of ferrites in the resonant overshoot mode causes less energy losses, which is particularly interesting for high pulse repetition rate operation of the laser. The energy loss reduction by a single pass along the ferrites in the switch mode cannot make up for the increased loss due to the larger volume as compared to the resonant overshoot mode.



## 4.8 Other modes

There are several other spiker-sustainer modes possible, whose differences depend on the used voltages and polarities in combination with the amount of magnetic material and the number of separate cores. For instance, the “diode” mode [10], the modified overshoot mode [7, 11] and the “charge” mode [12] all generate a voltage spike of the same polarity as the PFN voltage without a pre-pulse of the opposite polarity, although all in different ways. A same-polarity pre-pulse has the large advantage that the current through the laser can flow in only one direction, hence the name “diode” mode. A disadvantage is that at the moment of the laser breakdown the saturable cores are set in the wrong direction, i.e. with a low inductivity for current flowing *into* the PFN, which causes a delay between the breakdown of the laser and the onset of the main current. This start-up delay gives time for small-scale inhomogeneities to develop, thus causing a worse discharge quality. In these cases the effect is much stronger than in the resonant overshoot mode.

## 4.9 Three-electrode operation

One additional mode to operate a discharge pumped laser using a separate pre-pulse and main pulse is worth mentioning: the so-called middle-electrode circuit [13–15]. It uses the laser gas discharge itself as the main switch between the peaking circuit and the PFN. Thus, there is no additional energy loss in a switch and the entire system may be constructed with a very low self-inductance.

In this circuit the laser head is fitted with a third electrode, between the other two. In figure 4.10 an X-ray pre-ionised set-up is shown, together with the voltage pulse across the outer electrodes and the voltage pulse on the middle electrode. The PFN is attached directly to the outer electrodes, the pre-pulse generator is connected to the middle electrode. The middle electrode is either connected to the outer electrodes by small peaking capacitors  $C_P$  or it is left floating. The charging of the PFN, and thus of the outer electrodes, causes the middle electrode to be charged to the voltage of the equipotential plane it represents.

Once the PFN has been charged, both discharge volumes between the electrodes are pre-ionised. A trigger pulse, which can be of either polarity, is then applied to the middle electrode, which causes a breakdown in one of the two discharge gaps, see figure 4.10 for a set-up with the pre-pulse having the opposite polarity of the PFN voltage. The voltage on the middle electrode then starts to oscillate, which causes

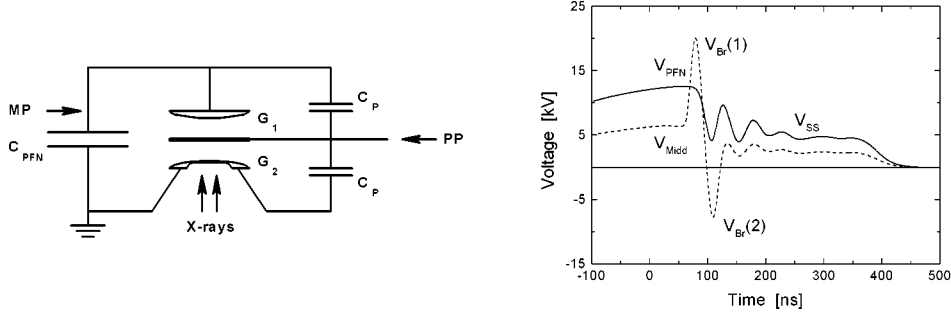


Figure 4.10: The three-electrode excitation circuit and the resulting voltage pulses. MP: Main pulse.  $C_{\text{PFN}}$ : Pulse Forming Network.  $G_{1,2}$ : Discharge gaps.  $C_P$ : Peaking capacitor. PP: Pre-pulse. Drawn line: PFN voltage. Dashed line: Voltage at middle electrode.  $V_{\text{PFN}}$ : PFN charging voltage.  $V_{\text{Midd}}$ : Voltage at middle electrode.  $V_{\text{br}}(1,2)$ : Breakdown voltages of the discharge gaps.  $V_{\text{SS}}$ : Steady state voltage of the total discharge.

the other discharge gap to break down, equivalent to the operating modes described above. Both halves of the discharge are subsequently sustained by the current from the PFN, which also passes through the middle electrode.

The optical output of this type of laser is a special case; two independent beams can be generated, or one single beam with a dark region in it. The most interesting set-up, however, is the use of one discharge-half as a master-oscillator and the other discharge-half as a self-timed amplifier [13, 15].

Lasers operating according to this excitation principle have already proven to be rather simple and rugged devices, capable of high repetition rates, e.g. see refs. [13–15].

Because of the absence of an additional switch, with the resulting self-inductance, the three-electrode laser has a very high potential for obtaining lasing in difficult gas mixtures that require high pumping powers. Using this set-up the influence of the self-inductance of the circuit on the laser-parameters may be studied across a larger region than is the case with other circuits, which might shed some light on the (im-)possibilities of these gases with other excitation circuits.

## References

- [1] **A.J. Kearsley, A.J. Andrews and C.E. Webb**, *A novel pre-ionization technique for discharge excited rare gas halide lasers*, Opt. Comm. **31** (2), 181–184 (1979).
- [2] **J.C.M. Timmermans**, *Double discharge XeCl-laser*, PhD thesis, University of Twente, Enschede, The Netherlands (1995).
- [3] **R.M. Hofstra**, *Simulatie en optimalisatie van een XeCl excimeer laser*, Master's thesis, University of Twente, Enschede, the Netherlands (1994). (In Dutch).
- [4] **F.A. van Goor, W.J. Witteman, J.C.M. Timmermans, J. van Spijker and J. Couperus**, *High average power XeCl laser with x-ray pre-ionization and spiker-sustainer excitation*, In: High-power gas and solid state lasers, M. Bohrer, T. Letardi, D. Schuöcker and H. Weber, eds., Proceedings of SPIE **2206**, 30–40 (1994).
- [5] **A.A. Zhupikov and A.M. Razhev**, *Excimer ArF laser with an output energy of 0.5 J and He buffer gas*, Quantum Electron. **27** (8), 665–669 (1997). [Kvantovaya Elektron. **24** (8), 683–687 (1997)].
- [6] **W.H. Long, M.J. Plummer and E.A. Stappaerts**, *Efficient discharge pumping of an XeCl laser using a high-voltage prepulse*, Appl. Phys. Lett. **43** (8), 735–737 (1983).
- [7] **R.S. Taylor and K.E. Leopold**, *Magnetic-spiker excitation of gas-discharge lasers*, Appl. Phys. B **59**, 479–508 (1994).
- [8] **M. Makarov and Yu. Bychkov**, *The dynamics of XeCl discharge contraction*, J. Phys. D: Appl. Phys. **29**, 350–363 (1996).
- [9] **T. Müller**, *Zeitliche entwicklung und filamentierung von KrF\*-lasergasentladungen*, PhD thesis, Technische Hochschule Darmstadt, Darmstadt, Germany (1992). (In German).
- [10] **C.H. Fisher, M.J. Kushner, T.E. DeHart, J.P. McDaniel, R.A. Petr and J.J. Ewing**, *High efficiency XeCl laser with spiker and magnetic isolation*, Appl. Phys. Lett. **48** (23), 1574–1576 (1986).
- [11] **R.S. Taylor, K.E. Leopold and M. von Dadelszen**, *Magnetic-spiker electrical circuits for gas discharge lasers*, In: High-power gas and solid state lasers, M. Bohrer, T. Letardi, D. Schuöcker and H. Weber, eds., Proceedings of SPIE **2206**, 130–143 (1994).
- [12] **J.C.M. Timmermans, F.A. van Goor and W.J. Witteman**, *A new mode to excite a gas-discharge XeCl laser*, Appl. Phys. B **57**, 441–445 (1993).
- [13] **T.J. McKee, S.D. Hastie and R.W. Weeks**, *Performance of a novel injection-locked excimer laser*, J. Appl. Phys. **56** (7), 2170–2173 (1984).
- [14] **V.V. Borovkov, V.V. Voronin, S.L. Voronov, D.I. Zenkov, B.V. Lazhintsev, V.A. Nor-Arevyan, V.A. Tananakin, G.I. Fedorov and I.M. Yutkin**, *Three-electrode discharge laser with a middle control electrode*, Quantum Electron. **25** (5), 414–415 (1995). [Kvantovaya Elektron. **22** (5), 439–440 (1995)].

- [15] **S. Bollanti, P. di Lazzaro, F. Flora, G. Giordano, T. Letardi, G. Schina and C.E. Zheng**, *Ianus, the three-electrode excimer laser*, Appl. Phys. B **66**, 401-406 (1998).

## Chapter 5

# Short pulse operation of the laser with different excitation circuits

The published results of research on discharge pumped ArF lasers are focused on the properties of (the generation of) laser pulses with a pulse length of  $\lesssim 25$  ns (FWHM). Although  $\text{NF}_3$  has been used as a fluorine donor [1], the used gas mixtures usually consist of several mbar  $\text{F}_2$  and Ar in the buffer gases He and/or Ne at pressures ranging from 2 to 5 bar, e.g. see refs. [1–8]. It is known, e.g. from research on XeCl lasers, that for the generation of long laser pulses, and thus of highly stable discharges, the used gas mixtures should contain low concentrations of the active ingredients, especially of the halogen donor, e.g. see refs. [9–13]. However, since the properties of the ‘richer’ gas mixtures had been studied to a certain extent, we first studied the behaviour of the ArF laser with this type of gas mixture.

Following several studies [3, 8, 14–18], we also performed some experiments on KrF ( $\lambda = 248$  nm) for comparison.

Experimenting with KrF instead of with ArF has several advantages. Although the kinetic behaviour of both lasers is fairly similar, a discharge pumped KrF laser needs less pumping power to show lasing and it yields more output power than an ArF laser under identical circumstances. Therefore the KrF laser has been studied more extensively than the ArF laser. As a consequence, the details of the kinetic properties

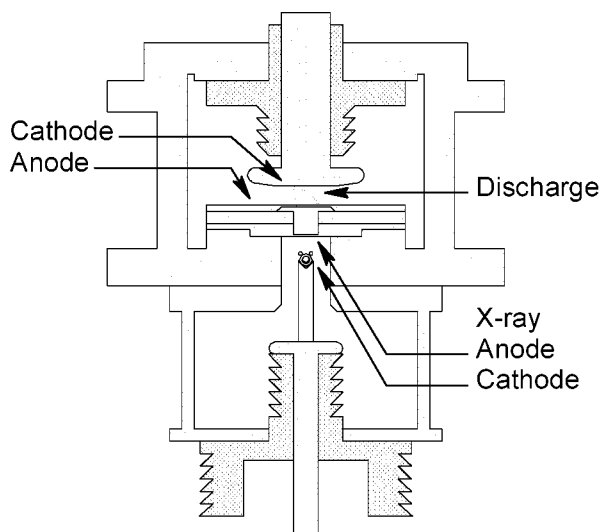


*Figure 5.1: A schematic overview of the laser chamber and the X-ray source. The discharge volume is pre-ionised through the laser anode. The X-ray source and the laser gas mixture are separated by the 1 mm thick aluminium pressure window annex X-ray anode. The discharge width is determined by the X-ray dose profile and the electrode profile.*

of the KrF laser are much better documented than those of the ArF laser.

In this chapter we present the results of a study of the laser performance using the different excitation modes treated in chapter 4. In the first part the electrical properties of the excitation circuits are discussed. In the next parts, the output energy and the pulse length of the laser pulse are used as indicators to determine the sensitivity of the laser to different variations in the experimental set-up.

## 5.1 Experimental set-up

The laser head consists of a rectangular stainless steel vessel, fitted at opposite sides with uncoated  $\text{MgF}_2$  windows. The approximately 95 mm wide laser cathode is of

the uniform field type [19], the grounded anode is flat (see Fig. 5.1). Both electrodes are made of nickel plated aluminium. The discharge volume is approximately  $60 \times 1.5 \times 1.2 \text{ cm}^3$  ( $l \times w \times h$ ).

The gas mixture of the ArF laser is 6 mbar  $\text{F}_2$ , 100 mbar Ar, 200 mbar Ne and 3.7 bar He. For the KrF laser the same gas mixture is used, with the argon replaced by an equal amount of krypton. The neon in the gas mixture is added to quench the self-starting atomic fluorine laser ( $\lambda = 713 \text{ nm}$ ). Although the atomic  $\text{F}_2$  laser has no known effects on the formation kinetics of the  $\text{ArF}^*$  molecules, its intensity is high enough to be measured by the photodiode behind the ArF and KrF laser line filters, possibly leading to erroneous results.

The gas mixture is pre-ionised by the X-ray source described in chapter 3, operated at a charging voltage of  $V_{\text{XP}} = 28 \text{ kV}$ . The X-ray pulse is then capable of generating an electron density of  $2.5 \cdot 10^9 \text{ cm}^{-3}$  in a gas mixture equal to the ArF laser gas mixture but without the fluorine, see figure 3.7. The pre-ionisation electron density in the KrF laser gas mixture is assumed to be of the same order of magnitude [20, 21].

The PFN and the peaking capacitors are mounted on top of the laser vessel, electrically separated by the rail gap or by the ferrites, see figure 5.2. The PFN capacitance is  $C_{\text{PFN}} = 324 \text{ nF}$ , built of 120 TDK ceramic capacitors of  $C_{\text{cap}} = 2.7 \text{ nF}$ . The PFN capacitors are fastened in pairs between copper strips in the form of 10 separate columns of 6 rows each. The peaking capacitance of  $C_{\text{P}} = 2.8 \text{ nF}$  consists of 4 TDK ceramic capacitors with  $C_{\text{cap}} = 0.7 \text{ nF}$ . The middle conductor is charged, the outer conductors are grounded on the laser vessel, which is grounded externally. All other electrical components of the set-up are grounded on the laser vessel as well.

The pre-pulse is generated by a mini-marx generator, equal to the the X-ray source driver, see appendix A. In the church mode the pre-pulse mini-marx is used for the voltage pulse on the trigger grid, see sections 4.2 and 5.2.1. Both mini-marx generators are pressurised with nitrogen, just higher than the critical pressure for spontaneous breakdown. The nitrogen is flowed at a rate of  $5 \text{ l/min}$ .

The PFN is pulse charged in a few  $\mu\text{s}$  from a separate circuit, consisting of a storage capacitor of  $C_{\text{MP}} = 300 \text{ nF}$  and an EEV CX1725 hydrogen-filled thyatron switch. In the rail gap switched circuits the PFN is charged above the rail gap, in the ferrite switched circuits the PFN is charged from the connectors underneath the switch, see figure 5.2. To obtain a high pumping power, the discharges are operated at much higher PFN voltages than required for operation under matched conditions. Unless stated otherwise, the charging voltages are: X-ray source mini-marx  $V_{\text{XP}} = 28 \text{ kV}$ , pre-pulse mini-marx  $V_{\text{PP}} = 20 \text{ kV}$ , PFN charging circuit  $V_{\text{MP}} = 24 \text{ kV}$ , yielding a

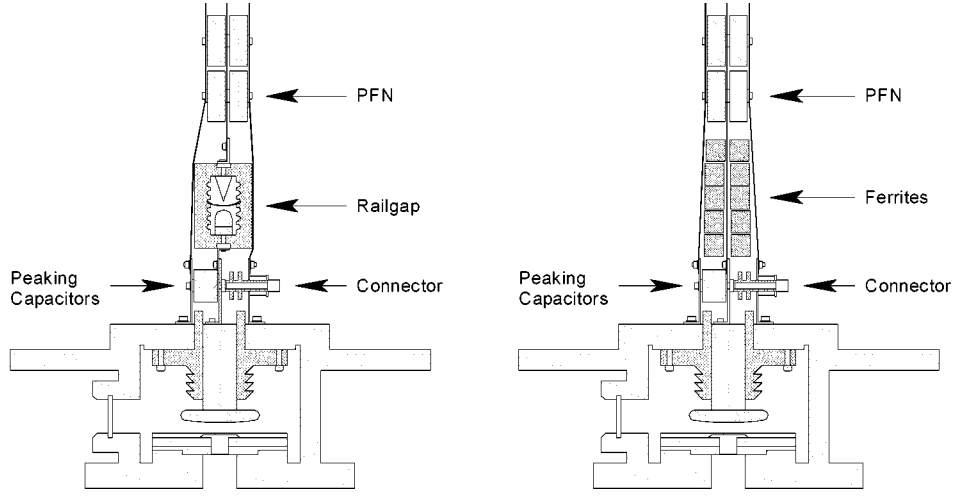


Figure 5.2: Cross sectional views of the experimental set-up, showing the construction of the rail gap (left) and the magnetic switch (right). The laser vessel is fitted with side windows, enabling the observation of the discharge transverse to the optical axis. The ‘wings’ of the laser vessel are needed for the structural integrity of the vessel at high pressures.

PFN voltage  $V_{\text{PFN}} = 28 \text{ kV}$ .

Two T&M resistive current probes are mounted in the main current returns on either side of the PFN, between the laser vessel and the peaking capacitors and the connectors. The measured current signal  $I_{\text{disch}}$  is the direct average of the signals of both probes. Home-built resistive voltage probes with  $R_{\text{probe}} \approx 25 \text{ k}\Omega$  are connected at several locations in the set-up. The main voltage probe is connected between the connection of the PFN to the high voltage feedthrough and the top of the laser vessel. The discharge voltage is calculated from this signal  $V_{\text{P}}$ , according to

$$V_{\text{disch}} = V_{\text{P}} - L_{\text{vess}} \frac{dI_{\text{disch}}}{dt} \quad (5.1)$$

with  $L_{\text{vess}} = 18 \text{ nH}$  being the self-inductance of the laser vessel. The PFN voltage is monitored by two resistive probes, one is connected directly across a capacitor in the



lowest row of the PFN. Another PFN-probe is connected between one of the lowest PFN capacitors and the top of the laser vessel. Both probes yield the same results. When using the rail gap the voltage on the trigger grid is measured between the high voltage feedthrough for the trigger pulse and the laser vessel. The X-ray cathode voltage is measured between the X-ray source cathode and the source-housing, which is directly connected to the laser vessel. The probes also serve to ground the different components between consecutive pulses.

All signals are measured using coaxial cables with a characteristic impedance of  $Z = 50 \Omega$ . The signals are measured with oscilloscopes, via home-built attenuators and commercial  $50 \Omega$  throughput terminators, inside a Faraday cage to minimise EM-noise. The oscilloscope traces are stored on a computer.

The voltage wave forms shown in this thesis are inverted in polarity for increased clarity. In the text the polarities of the voltages are treated accordingly. However, for the sake of a consistent terminology, the laser cathode has been consequently named just that, while the term ‘anode’ would have been more appropriate in view of the presentation of the voltage signals.

## 5.2 Electrical behaviour of the laser with different circuits

The electrical behaviour of the laser cannot be seen apart from the behaviour of the discharge, since the impedance of the gas evolves during the discharge. For instance, a glow-discharge implies the existence of steady state situation in which a very broad range of current densities can flow through the discharge at a near constant voltage, while the gas absorbs large amounts of electrical energy. One or more discrete arcs in the discharge volume represent a short-circuit, sustaining only a small voltage difference and absorbing very little energy. The number and the spatial distribution of the arcs also affect the self-inductance of the discharge and thus of the circuit.

However, in view of the differences and the similarities amongst the pulses and the theoretical expectations, a comparison between the electrical features of the used circuits is allowed.

It should be noted here that the pulses shown in this section all generated ArF laser pulses, with the exception of the X-ray triggered or charge transfer mode, see sections 4.1 and 5.2.4. The effects of the different pulses on the lasing properties of the gas are discussed in more detail in section 5.3.

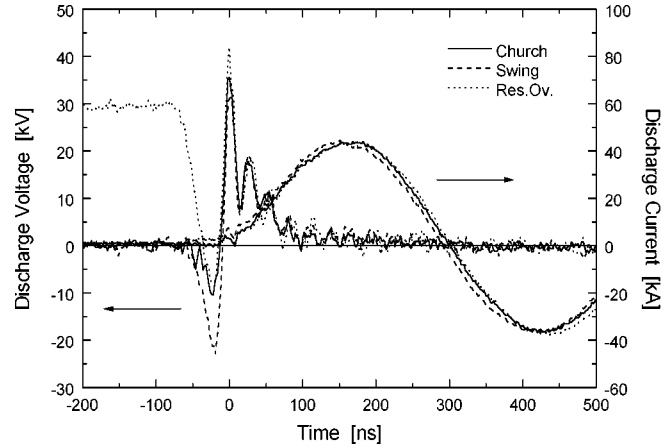


Figure 5.3: Typical current and voltage wave forms of the rail gap switched circuits.

### 5.2.1 Rail gap switched circuits

The rail gap is mounted between the peaking capacitors and the PFN capacitors, see figure 5.2. The rail gap consists of a sharp edged brass electrode and a round one, fitted inside a perspex tube which is profiled on the inside to increase the surface tracking length. The interelectrode gap is  $d_{RG} = 10$  mm. Between the electrodes a stainless steel trigger grid is mounted. The trigger grid is curved to reduce the disturbance of the electrical field inside the rail gap. Due to its parasitic capacitance the trigger grid is charged to the appropriate equipotential voltage during the charging of the PFN. The rail gap is pressurised to  $P_{RG} = 1.5$  bar with nitrogen which is continuously flowed at  $5 \ell/\text{min}$ .

In the swing mode, the breakdown voltage of the rail gap is lower than the breakdown voltage of the laser, but significantly higher than the expected steady state voltage  $V_{SS}$  of  $\sim 5$  kV [1–8].

The inductor  $L_{RG}$  that bridges the rail gap in the resonant overshoot mode is constructed in the form of two solenoids of  $L_{Sol} = 32 \mu\text{H}$  each, placed on either side of the

rail gap. With  $L_{\text{RG}} = 16 \mu\text{H}$  and  $C_{\text{P}} = 2.8 \text{ nF}$ , the  $RLC$ -time for a charge to leak away from the peaking capacitors to the PFN is  $\tau_{\text{P}} = \pi\sqrt{L_{\text{RG}}C_{\text{P}}} = 665 \text{ ns}$ . The charging of  $C_{\text{P}}$  by the mini-marx up to the breakdown of the rail gap takes approximately 50 ns, thus the pre-pulse is not affected significantly by the presence of  $L_{\text{RG}}$ . On the other hand, the charging of the PFN takes approximately 5  $\mu\text{s}$ , so that the PFN-charging voltage is indeed fully transferred to  $C_{\text{P}}$ .

An overview of the voltage and current wave forms of the rail gap triggered modes is given in figure 5.3. It can be seen from the figure that in the wave forms there is no steady state voltage discernible. After the first current pulse, in which the laser pulse is generated, the current continues to oscillate nearly undamped. The free current oscillation, without a corresponding large voltage oscillation, indicates the discharge being short circuited by arcs.

From the wave forms in figure 5.3 may be seen that the trigger pulse of the rail gap in the church mode (full line) causes a small charging pulse on the peaking capacitors and the laser electrodes, because the lower half of the rail gap breaks down first, before the upper half does. This pre-pulse may be avoided by lowering the voltage of the trigger pulse and the gas pressure inside the rail gap. However, this also causes a more erratic behaviour of the rail gap. Therefore it has been chosen to keep all parameters equal in the rail gap switched circuits, resulting in the small pre-pulse in the church mode.

The three modes exhibit the same pulse shape from the breakdown of the rail gap to the discharge breakdown. This is to be expected since the temporal behaviour of the voltage overshoot is determined solely by the circuit parameters, considering all voltages being equal. The similarity in the pulse shape after the breakdown of the laser indicates an equivalent behaviour of the discharge under these circumstances.

### 5.2.2 Magnetically-switched resonant overshoot mode

The properties of saturable inductors and the operation of the ferrite switched resonant overshoot mode have been explained in sections 4.5 and 4.6. In this section we discuss the effects of a variation of the amount of saturable magnetic material in the switch in some more detail.

The magnetic material used for the saturable inductor switch is CMD 5005 high frequency ferrite, see section 4.5, available in blocks with a cross section of 6  $\text{cm}^2$  each. The ferrites are mounted at the same location in the set-up as the rail gap, see figure 5.2. The construction of the laser allows zero to five ferrite blocks to be used

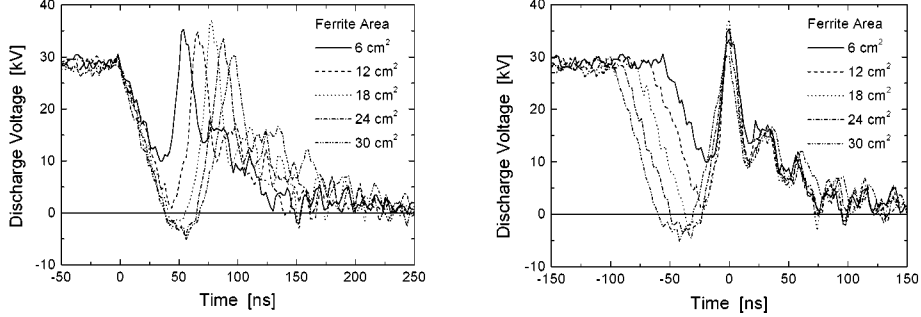


Figure 5.4: Typical voltage wave forms of the ferrite switched resonant overshoot mode with different amounts of ferrite in the switch. Both panels show the same voltage pulses, only shifted in time to let the onsets of the pre-pulses (left) or the breakdown voltages (right) coincide.

in the switch, thus 0 to 30 cm<sup>2</sup> ferrite. The geometrical self-inductance of the system remains the same during the experiments, independent of the number of ferrite blocks in the switch. Removing all ferrites from the system causes the laser to behave in a charge-transfer mode, see sections 4.1 and 5.2.4.

The effects of varying the ferrite area in the switch on the voltage and current signals are shown in figures 5.4 and 5.5. An increased amount of ferrites in the switch, thus a larger  $A_{\text{ferr}}$ , results in an increased voltage difference and time lapse  $V\Delta t$  needed to break down the switch, in accordance with equation 4.6 with  $N = 1$ , see figure 5.4;

$$V(t) \Delta t = \Delta B A. \quad (4.6')$$

The increased self-inductance of the circuit due to the larger ferrite area is evident from the increasing voltage rise time from the switching of the ferrites to the breakdown voltage in the overshoot. Furthermore, the switching of the ferrites can be seen to become slower as the ferrite area increases. The consequences of this effect for the operation of the laser will be discussed in section 5.3.

As in the case of the rail gap switched circuits, there is no steady state voltage found in the pulses in figures 5.4 and 5.5 and the current continues to oscillate after the

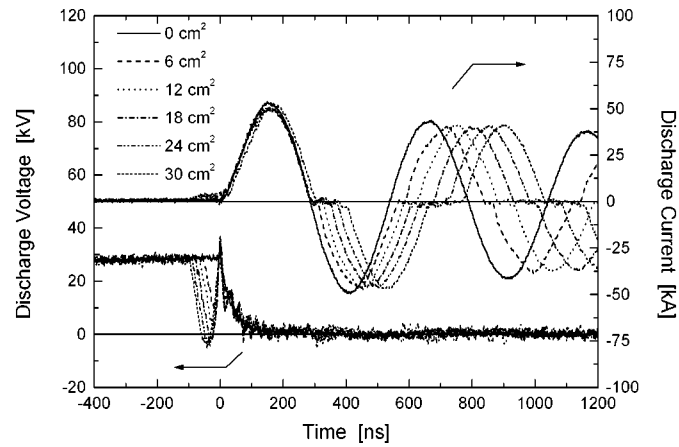


Figure 5.5: Typical voltage and current wave forms of the ferrite switched resonant overshoot mode with different amounts of ferrite in the switch, as well as the charge transfer mode ( $0 \text{ cm}^2$  ferrite), see also figure 5.4. The discharge breakdown occurs at the same time in all pulses.

first half sine wave, in which the laser pulse is generated. Thus we can conclude that the gas discharge volume is again completely short-circuited by arcs, with hardly any energy loss. The system loses energy primarily in the continuous setting and resetting of the ferrites that causes periods with near zero current after each voltage oscillation. The duration of these periods increases with increasing ferrite area, in accordance with equation 4.6. Of course, when using no ferrites (charge transfer mode) the current pulse does not show these regions and the current oscillations are nearly undamped.

### 5.2.3 Comparison of the resonant overshoot mode with different switches

Figure 5.6 shows a comparison between the current and voltage pulses of the resonant overshoot mode, both of the rail gap switched circuit [Fig. 5.3] and of the ferrite-

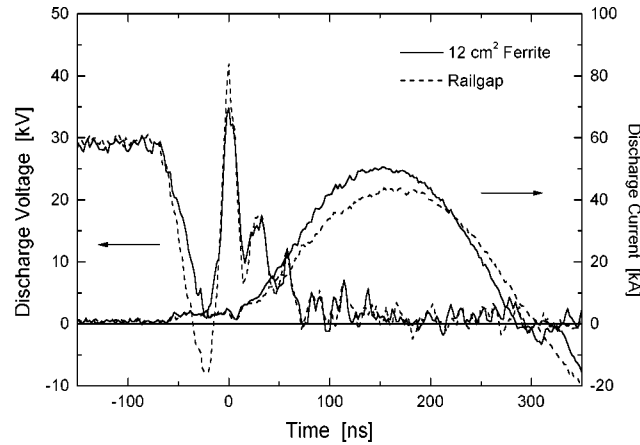


Figure 5.6: A comparison between typical voltage wave forms of the resonant overshoot mode, using a magnetic switch with  $12 \text{ cm}^2$  ferrite and using the rail gap.

switched circuit with  $12 \text{ cm}^2$  ferrite [Figs. 5.4, 5.5]. The capacitances and the charging voltages are equal in both cases.

From figure 5.6 can be seen that the rail gap switched pulse strongly resembles that of the magnetically switched pulse with  $12 \text{ cm}^2$  ferrite. The rail gap switched pulse can be made to fit the magnetically switched pulse more closely, when the gas pressure inside the rail gap is adjusted to cause a lower rail gap breakdown voltage. However, this results in a more erratic behaviour of the rail gap. The gas pressure is therefore kept at 1.5 bar.

Although the voltage pulses bear a striking resemblance, it is clear that the behaviour of the discharge current is different. The pulse from the magnetically switched circuit shows the ferrite-resetting time of near-zero current, which is of course absent in the rail gap switched pulse. In the ferrite switched case the peak current is higher and the current oscillation time is shorter.

The peak current and the current oscillation time (without taking into account the resetting time) do not change significantly as a function of the ferrite area in the magnetic switch, see figure 5.5. Therefore, this effect is not due to a difference in

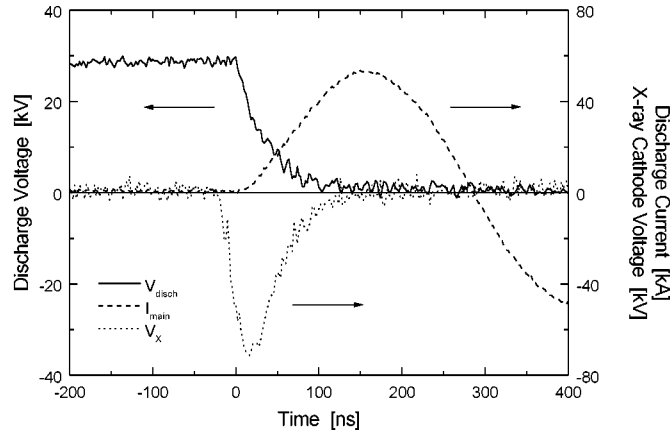


Figure 5.7: Typical wave forms of the X-ray triggered mode. Charging voltage:  $V_{\text{PFN}} = 28 \text{ kV}$ .

the self-inductance of the switches. The most likely cause of the difference in the current pulses is the fact that the closed rail gap switch constitutes a gas discharge in its own right, albeit one consisting of arcs. Thus, the rail gap discharge consumes part of the energy present on the PFN, which therefore cannot be transferred to the laser discharge. The energy absorption by the rail gap discharge is determined by the gas pressure  $P_{\text{RG}}$  and the electrode separation of the rail gap  $d_{\text{RG}}$ . The effects of variations in  $P_{\text{RG}}$  and  $d_{\text{RG}}$  can be large enough to be measurable in the laser performance, see section 6.2 and ref. [22]. It is therefore important to keep the rail gap properties the same throughout the experiments.

#### 5.2.4 X-ray triggered mode

This circuit is made by using the saturable inductor switched-set-up, without using ferrites. Thus the peaking capacitors and the PFN act as a single capacitor with  $C_{\text{stor}} = C_{\text{PFN}} + C_{\text{P}} = 328.8 \text{ nF}$ . The capacitor is pulse charged in approximately  $5 \mu\text{s}$ , after which the X-ray source is fired. The voltage collapse occurs within  $15 \text{ ns}$  from the onset of the X-ray pulse, see figure 5.7. The current strongly oscillates after the

breakdown, unhampered by loss factors, see also figure 5.5.

There is no steady state voltage discernible, and no lasing occurs. This is different from a similar set-up with a XeCl laser, in which a clear steady state is found and strong lasing occurs [12, 23].

The ArF gas discharge probably breaks down in arcs, because during the long period of the charging of the PFN electron avalanches already grow from free electrons that are present in the gas. The attachment of fluorine aggravates the resulting inhomogeneity, which the application of pre-ionisation cannot make up for. If no pre-ionisation is applied the gas breaks down spontaneously anywhere from 10 to 300 ns later than the time the X-ray pulse would have been fired, because of these coincidental avalanches. Raising the PFN voltage a little causes the discharge to break down spontaneously before the application of the X-ray pulse. In these cases there is no lasing either.

The spontaneous breakdown is also a limiting factor in the PFN charging voltage when the laser is operated with a magnetic switch or with the rail gap-switched resonant overshoot mode, since in these cases the PFN voltage is also present on the electrodes before the pre-ionisation or the pre-pulse have been applied. The effect of the charging time on the performance of the laser in the case of magnetic switching has not been studied extensively, although several researchers have noted the spontaneous breakdown during the charging of the PFN [11, 12, 22–25]. There have also been some studies to the effects of the voltage rise time in short pulse lasers with respect to the pre-ionisation efficiency in the charge transfer mode [24, 26–28].

### 5.2.5 Three-electrode circuit

The three-electrode circuit, or middle grid circuit, has been studied using a third electrode in the laser vessel, home-made of a stainless steel wire mesh (mesh area  $1 \text{ mm}^2$ , transparency ca. 50 %) which was spot-welded onto an aluminium frame of 1 mm thickness. The frame was mounted on four glass-fiber posts to keep the mesh electrode suspended between the laser electrodes. The non-ideal shape of the mesh electrode disturbed the otherwise homogeneous electrical field inside the discharge volume, which enhanced the chances of arcing. The trigger pulse was delivered to the mesh electrode by the same mini-marx that was used for the pre-pulse in the other circuits.

The set-up has been tested with pure He and mixtures of He : Ne, He : Ar and He : Ne : Ar. In all cases it proved possible to generate discharges that were homogeneous to the eye in one half-gap, but in all cases only arcing occurred in the other half-gap. In



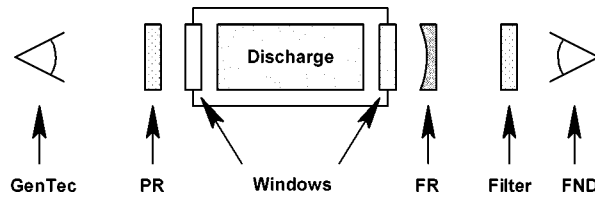


Figure 5.8: The optical set-up for the ArF experiments. GenTec: Energy meter. PR: Partial reflector, 70 % R/25 % T, flat. Windows:  $\text{MgF}_2$  windows, uncoated, plane parallel  $< 20^\circ$ . FR: Full reflector,  $\sim 98$  % R/0.5 % T, 6 m concave radius. Filter: Laser line filter ArF. FND: Photodiode.

which half-gap the homogeneous-appearing discharge could be made depended on the height of the mesh electrode between the two electrodes and the used voltages and polarities.

Since the discharge could not be made uniform in both half-gaps we did not pursue the matter further. However, it is our firm belief that it should be very interesting to investigate the use of this circuit, with appropriately shaped electrodes, for the discharge pumping of excimer lasers, since the need for a switch in the main circuit is removed.

### 5.3 Performance of the laser as a function of the pre-ionisation timing

We studied the performance of the laser as a function of the timing between the pre-ionisation and the breakdown of the discharge with the above described voltage pulses.

Throughout the experiments the resonator mirrors are placed outside the laser vessel, to avoid contact with the fluorine containing gas mixture. When studying the ArF laser a full reflecting mirror with a 10 m concave radius and a plane 70 % reflection outcoupler are used. The KrF laser resonator consists of a plane full reflector and a plane 47 % reflection outcoupler. The  $\text{MgF}_2$  windows are aligned with the mirrors, to minimise reflection losses.

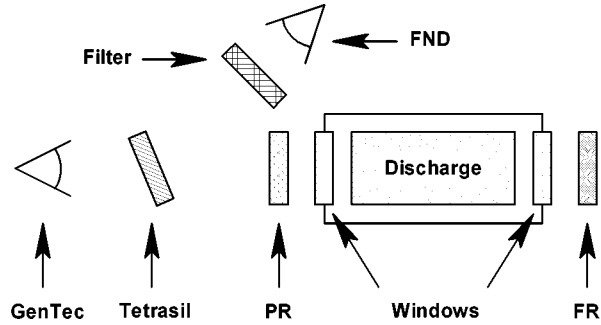


Figure 5.9: The optical set-up for the KrF experiments. GenTec: Energy meter. Tetrasil: Uncoated window, used as beam splitter. Filter: Laser line filter KrF. FND: Photodiode. PR: Partial reflector, 47 % R/48 % T, flat. Windows:  $MgF_2$  windows, uncoated. FR: Full reflector,  $\sim 98$  % R, flat.

The output energy  $E_{out}$  of the laser pulses is measured with a GenTec pyroelectric energy meter. The intensity of the laser pulses is monitored with a UV sensitive photodiode (FND100Q) through the rear laser mirror and a 193 nm in the case of the ArF laser, see figure 5.8.

The back side of the used full reflector of the KrF laser is opaque. Therefore the laser pulse intensity is monitored, through a 248 nm filter, by the reflectance of the laser beam on an uncoated 5 mm thick tetrasil window acting as a beam splitter. The tetrasil window is placed between the outcoupling mirror and the GenTec, see figure 5.9. The energy loss at the GenTec due to the beam splitter is approximately 13 %.

With each circuit a series of laser pulses is fired with different pre-ionisation delay times  $\Delta t_X = t_X - t_0$ , where  $t_X$  is the start of the X-ray pulse and  $t_0$  indicates the breakdown of the laser, see figure 5.10.

### 5.3.1 Rail gap switched circuits

The output energy as a function of  $\Delta t_X$  for the church mode, the swing mode and the rail gap switched resonant overshoot mode are shown in figure 5.11 for the ArF

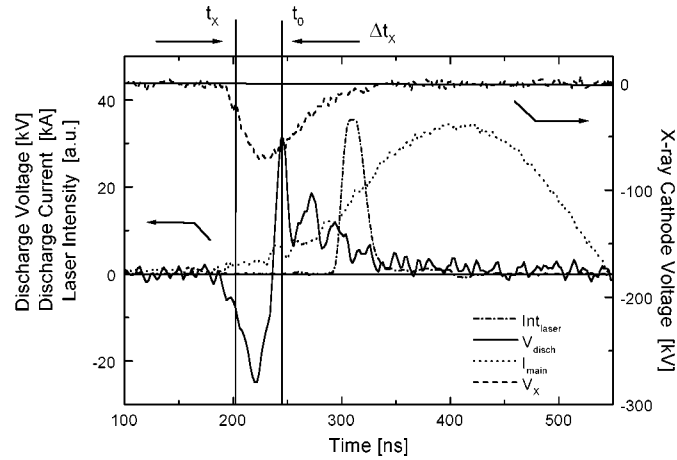


Figure 5.10: Typical wave forms of an ArF swing mode pulse and the definition of the pre-ionisation delay time  $\Delta t_x$ . Output energy: 34 mJ. Laser pulse length: 24 ns FWHM. Charging voltages:  $V_{\text{PFN}} = 22$  kV,  $V_{\text{PP}} = 20$  kV.  $\Delta t_x = -44$  ns.

laser. The results for the KrF laser are shown in figure 5.12.

The church mode and the resonant overshoot mode both exhibit a very short delay time window in which output can be generated, with the resonant overshoot mode yielding slightly more output than the church mode. With the swing mode longer pre-ionisation delay times can be allowed. The output then shows a clear maximum and a local minimum of near zero energy. With short delay times,  $\Delta t_x$  shorter than  $\sim 22$  ns, all three excitation modes show the same behaviour. The results are equal for both lasers.

The measured output of the KrF laser is higher than that of the ArF laser and the pre-ionisation delay windows for the different modes are slightly longer with KrF than with ArF. This is likely to be caused by the KrF laser having a higher gain. Similarly, when the pumping power of the ArF laser is decreased, by lowering the PFN voltage, the output energy per pulse drops and the pre-ionisation window gets smaller, see figure 5.13.

We can explain our results when the processes leading to the breakdown of the laser

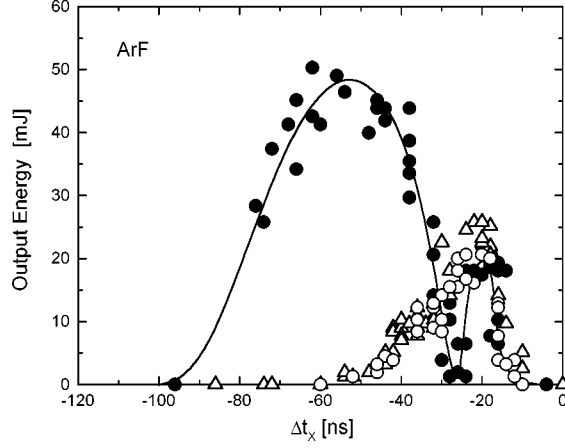


Figure 5.11: ArF laser output energy as a function of the pre-ionisation delay time  $\Delta t_x$  with different excitation circuits. ○: Church mode. ●: Swing mode. △: Resonant overshoot mode (rail gap). The curve is drawn to guide the eye.

gas mixture are taken into account, and the fact that a  $F_2$  containing discharge inherently gets unstable. Discharge instabilities are developed in a few ns from minor pre-ionisation inhomogeneities, electrode irregularities, cathode hot spots and/or local gas density fluctuations [9, 29–31]. Unstable discharges generate low or no laser output because pumping power is lost in the discharge streamers and because plasma filamentation disturbs the optical properties of the medium.

The fast growth of discharge instabilities is reflected in our results. In the church mode and in the resonant overshoot mode output energy is obtained only when the X-ray pulse overlaps the voltage pulse at  $V_{AC} > V_{SS}$ , prior to the breakdown, see figures 4.2, 4.4 and 5.10. When the X-ray pulse starts too close to the discharge breakdown, there is insufficient time for the multiplication process to generate a homogeneous electron density which is high enough for a homogeneous breakdown [11, 26]. When the X-ray pulse is applied too early, i.e. before  $V_{AC} > V_{SS}$ , pre-ionisation electrons will be lost due to the rapid attachment to  $F_2$ . Furthermore, the negative voltage on the cathode will push the present electrons away from it, leaving a depleted layer [10, 26]. These

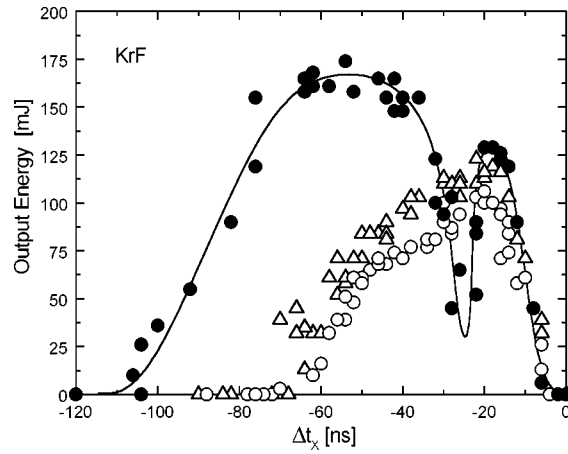


Figure 5.12: *KrF* laser output energy as a function of the pre-ionisation delay time  $\Delta t_x$  with different excitation circuits.  $\circ$ : Church mode.  $\bullet$ : Swing mode.  $\triangle$ : Resonant overshoot mode (rail gap). The curve is drawn to guide the eye.

processes lead to inhomogeneous electron densities during the discharge formation. Thus poor discharges with low output energies result.

Pre-ionisation of the gas mixture can also be performed by detaching electrons from  $F^-$ , as proposed by Hsia [32]. This process is approximately 0.03 % efficient, thus an initial electron density of  $n_{e0} \approx 3 \times 10^{10} \text{ cm}^{-3}$  is required during a long time [10,21]. In our set-up this pre-ionisation level cannot be reached. Furthermore, we observe no lasing at long pre-ionisation delays, which is the regime of the process. Therefore, we assume the effective pre-ionisation to be due to the directly generated electron density only.

In the swing mode the two time windows in which output is generated are probably caused by the electrode voltage being higher than  $V_{SS}$  both during the pre-pulse and during the overshoot, see figures 4.3, 5.3 and 5.10. The minimum in the output energy corresponds to the application of the maximum of the X-ray pulse during the voltage cross-over from  $-V_{SS}$  to  $+V_{SS}$  between the pre-pulse and the overshoot.

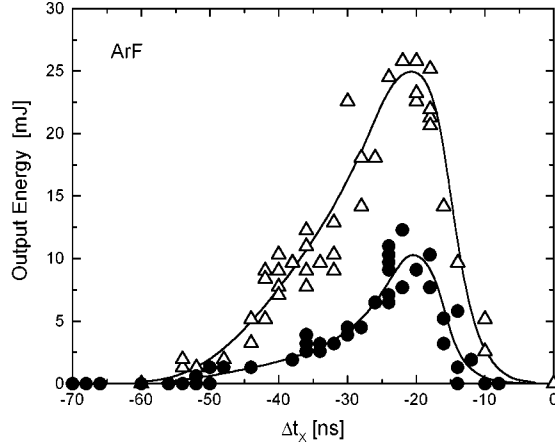


Figure 5.13: *ArF* laser output energy as a function of the pre-ionisation delay time  $\Delta t_x$  and of the PFN voltage  $V_{\text{PFN}}$ . Resonant overshoot mode (rail gap). The curves are drawn to guide the eye. Charging voltages:  $\Delta$ :  $V_{\text{PFN}} = 28$  kV.  $\bullet$ :  $V_{\text{PFN}} = 23$  kV.  $V_{\text{PP}} = 20$  kV.

In the resonant overshoot mode the electrodes are initially charged to the PFN voltage, which is well above  $V_{\text{SS}}$ . However, the voltage drops below  $V_{\text{SS}}$  for approximately 25 ns when the pre-pulse is applied, see figures 4.4 and 5.3. During this time the possible beneficial effects of the initial presence of a high voltage are cancelled. Pre-ionising during the PFN charging, before the application of the pre-pulse, results in an X-ray triggered discharge [Sec. 5.2.4], in which case there is no output generated.

The rise time of the voltage on the peaking capacitors is equal in all circuits, because it is primarily determined by the self-inductance of the circuit between the PFN and the peaking capacitors, see figure 5.3. This explains the similarity in the performance of all three excitation modes at low  $\Delta t_x$ .

The higher output energy when using the swing mode with longer pre-ionisation delay times is probably caused by the following effect: during the pre-pulse the electron multiplication due to  $V_{\text{AC}} > V_{\text{SS}}$  is very efficient because the electron attachment to fluorine is reduced at high  $E/N$  values [33]. Since the laser does not break down during the pre-pulse, it acts as an extra long pre-ionisation multiplication time.

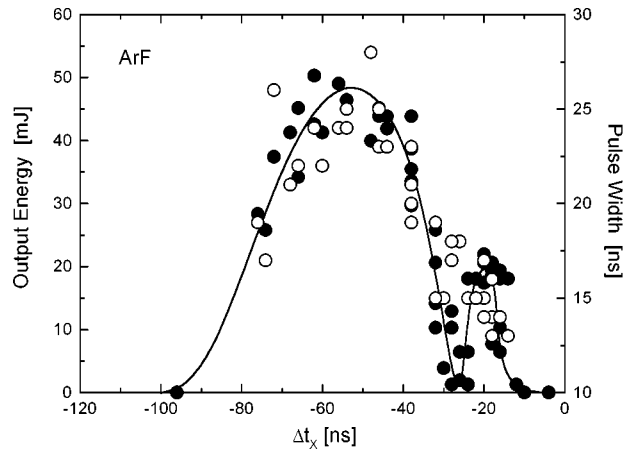


Figure 5.14: The output energy and the pulse width (FWHM) of the ArF laser in the swing mode. ●: Output energy. ○: Pulse width (FWHM intensity). The similarity in the behaviours is striking. The curve is drawn to guide the eye, see also figure 5.11.

In order to produce an initially uniform discharge it is necessary for individual avalanches to grow and overlap, perpendicular to the field, before they have reached a given size [26], see section 2.2. During the pre-pulse the heads of the individual electron avalanches grow radially while the tail extends towards the cathode. At the voltage reversal, before the actual breakdown, both the electrons in the head and those in the tail will reverse in direction. If the avalanche heads have grown to the critical size and have started to overlap at that time, this results in a more widely spread charge distribution at the breakdown than simple unipolar avalanches would. Thus it gives a better avalanche overlap and hence a better laser performance. If, on the other hand, the avalanche heads have not yet grown enough at the moment of the voltage reversal, the reversing electrons of the avalanche head will sense the lingering positive space charge field of the avalanche tail. This will decrease the further lateral growth of the avalanche heads, resulting in a very inhomogeneous charge distribution at the moment of breakdown. The resulting poor discharges are likely to cause the low output of the swing mode at  $\Delta t_x \approx -22$  ns. These effects may be further increased by the increased electron attachment to  $F_2$  at low electric fields.

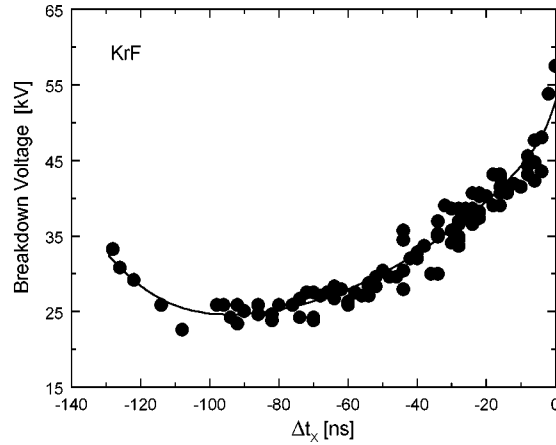


Figure 5.15: The breakdown voltage of the KrF laser gas mixture in the swing mode as a function of the pre-ionisation delay time  $\Delta t_X$ . The curve is drawn to guide the eye.

Another reason for a higher output energy when using the swing mode with longer  $\Delta t_X$  is probably that although during the pre-pulse a depleted cathode layer is formed, during the following voltage overshoot of the opposite polarity the present electrons are accelerated in the reverse direction, refilling the depleted area [34]. Therefore the subsequent breakdown starts from a much more homogeneous electron density. The result is a better discharge quality and a higher output energy.

The better discharge quality results in a longer laser pulse as well, see figure 5.14. In figure 5.14 the laser pulse length (FWHM) and the output energy are shown as a function of the pre-ionisation delay time in the swing mode voltage, see also figure 5.11. The behaviour of the pulse width closely resembles the output energy, indicating that the discharge quality varies with the pre-ionisation delay time according to the argument above.

With an increasing pre-ionisation delay the electron density at the start of the overshoot increases in the swing mode, due to the multiplication during the pre-pulse. A higher electron density at the start of the overshoot is translated into a lower breakdown voltage, see figure 5.15. From figure 5.15 it can be seen that the breakdown



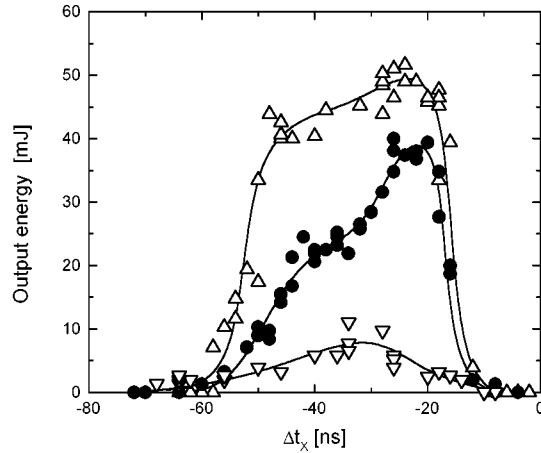


Figure 5.16: ArF laser output energy as a function of the pre-ionisation delay time  $\Delta t_X$  in the magnetically switched resonant overshoot mode.  $\Delta$ :  $6 \text{ cm}^2$  ferrite.  $\bullet$ :  $18 \text{ cm}^2$  ferrite.  $\nabla$ :  $30 \text{ cm}^2$  ferrite. The curves are drawn to guide the eye.

voltage of the KrF laser rises quickly at delays  $\Delta t_X$  longer than 100 ns, i.e. when the X-ray pulse is applied before  $V_{AC} > V_{SS}$ . This may again be related to the electron attachment of the fluorine, causing less free electrons to be present when  $V_{AC}$  increases over  $V_{SS}$ . At these long pre-ionisation delays the laser generates no output, caused by minor inhomogeneities growing into filaments during the pre-breakdown phase. This process of plasma filamentation during the pre-breakdown phase already affects the optical performance from  $\Delta t_X \approx -60$  ns.

### 5.3.2 Ferrite switched resonant overshoot mode

The dependency of the ArF laser output energy of the laser on the pre-ionisation timing has been studied for the magnetically switched resonant overshoot mode as well.

The results are shown in figure 5.16, for the case of a ferrite area of  $6 \text{ cm}^2$ , of  $18 \text{ cm}^2$  and of  $30 \text{ cm}^2$  (1, 3 or 5 bars of ferrite respectively). Typical voltage pulses of the

set-up with different amounts of ferrite in the switch are shown in figure 5.4 on page 66.

Figure 5.16 shows that ArF laser output energy is measured within a pre-ionisation time window ranging from  $\Delta t_X \approx -10$  ns to  $\Delta t_X \approx -60$  ns. When using  $\leq 24$  cm<sup>2</sup> ferrite the optimum output energy is obtained at a pre-ionisation delay of  $\Delta t_X \approx -20$  ns. With 30 cm<sup>2</sup> ferrite the pre-ionisation window extends to  $\Delta t_X \approx -70$  ns and the optimum pre-ionisation timing has shifted to  $\Delta t_X \approx -32$  ns.

The results show a “shoulder” at longer pre-ionisation delays, which becomes more pronounced with a decreasing ferrite area. When using 12 cm<sup>2</sup> ferrite the output lies between the results of 6 cm<sup>2</sup> and those of 18 cm<sup>2</sup>. With a peak output energy of  $\sim 34$  mJ the results of using 24 cm<sup>2</sup> ferrite are slightly lower than in the case of 18 cm<sup>2</sup>. However, the behaviour of the output energy with respect to the pre-ionisation timing is equivalent for the results of 18 and 24 cm<sup>2</sup>.

For the explanation of the results of the different resonant overshoot mode voltage pulses the same arguments hold as for the rail gap switched circuits. At short pre-ionisation delays there is insufficient time to generate a good homogeneous electron density, so that a poor discharge results and no output is generated. At long pre-ionisation delays small-scale inhomogeneities have had a chance to grow into streamers and arcs that prevent lasing. Applying the X-ray pulse during the charging of the PFN, before the start of the pre-pulse, causes a premature breakdown of the gas mixture which generates no lasing. The optimum output energy is obtained when the onset of the X-ray pulse coincides with the minimum voltage in the cases of 6 and 12 cm<sup>2</sup> ferrite. When using 18 or 24 cm<sup>2</sup> ferrite the optimum output energy is obtained if the X-ray pulse starts when the rising edge of the voltage crosses zero.

The appearance of a shoulder around  $\Delta t_X \approx 40$  ns on the output behaviour is probably caused by a decreased pre-pulse voltage with respect to the PFN voltage when using less ferrite. This means that the voltage across the laser electrodes remains higher, see figure 5.4. The result is a more efficient electron multiplication. Furthermore, with a lower amount of ferrite the voltage remains shorter below  $V_{SS}$  and the voltage rise time from the saturation of the ferrites to the breakdown of the gas mixture is decreased, which gives less time to inhomogeneities to develop into streamers, see figure 5.4. This can also explain the increased output energy with decreasing ferrite area.

When using 30 cm<sup>2</sup> ferrite in the switch the optimum output is found at a longer pre-ionisation delay than in the other cases. However, in this case the optimum output energy is also obtained when the onset of the X-ray pulse coincides with the rising edge of the voltage crossing zero. Because of the significantly longer voltage rise time

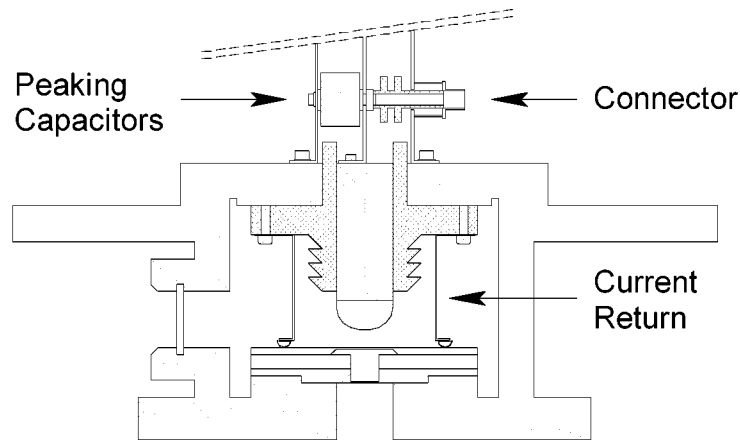


Figure 5.17: A cross section of the modified laser head, showing the R16 cathode and the current returns which reduce the self-inductance of the circuit.

in this case is than in the case of less ferrites, and the fact that  $\Delta t_X = 0$  is chosen to be at the breakdown of the discharge, a longer delay time is found.

## 5.4 Influence of the pumping power on the laser performance

The pumping power of the laser can be increased by increasing the current density in the discharge. One method is to decrease the discharge width, while maintaining the same electrode separation, thus keeping the same operating voltages. Another way to achieve a higher current density is by decreasing the self-inductance of the excitation circuit. Both methods have been tested in our set-up.

To investigate the effect of a decreased self-inductance the set-up is fitted with additional current returns inside the laser vessel, see figure 5.17. The laser cathode is replaced by a narrower cathode, made of nickel plated aluminium. The 62 cm long laser cathode has a flat centre area of 8 mm wide and rounded edges with a radius of

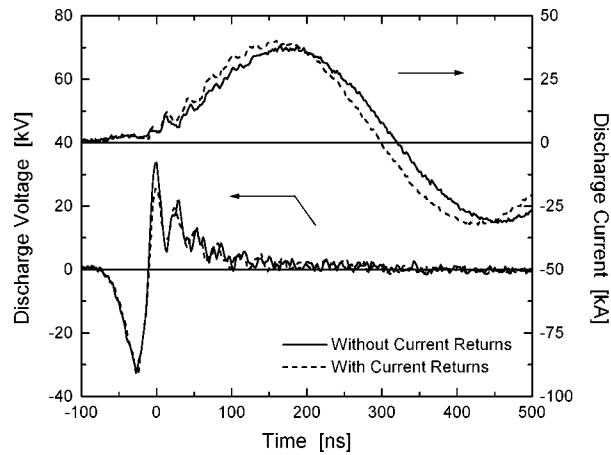


Figure 5.18: Typical wave forms of the laser, showing the effect of decreasing the self-inductance of the circuit with the 'R16' cathode.

curvature of 16 mm, hence it has been named the 'R16 cathode'. The laser electrode separation is kept at 12 mm, resulting in a reduced discharge width of approximately 11 mm.

The current returns are made of two copper plates on either side of the cathode along the discharge length. The plates are fastened inside the laser vessel via the bolts of the high voltage feedthrough and they are connected to the laser anode via elastic pressure contacts. The current returns reduce the self-inductance of the laser head from  $\sim 18$  nH to  $\sim 11$  nH.

The discharge current and voltage pulses for the set-ups with and without the additional current returns are shown in figure 5.18. In figure 5.18 can be seen that the peak current in the first half oscillation is increased when the current returns are used. In the following oscillations the peak currents of both situations are almost equal. The similarity of the voltage pulses and the difference in the current pulses indicate that more pumping power is transferred to the discharge in the first half oscillation when the current returns are used. After the discharge collapse in arcs the energy absorption is equal in both cases, shown by the equal value and decrement of the two current pulses. The shorter current oscillation time when using the current

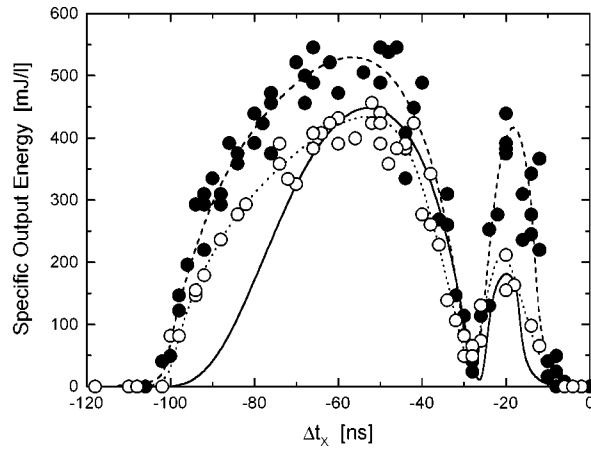


Figure 5.19: *ArF* laser output energy as a function of the pre-ionisation delay time  $\Delta t_x$  in the swing mode using different experimental configurations. Drawn line, no symbols: Ernst cathode (see figure 5.11).  $\circ$ : R16 cathode.  $\bullet$ : R16 cathode with additional current returns.

returns is caused by the decrease of the self-inductance.

The electric field gradients along the edges of the flat centre of the R16 cathode cause disturbances that can be seen in burn marks of the laser on thermofax paper. The discharge is also significantly brighter to the eye at the electrode edges. The field disturbance at the edges is further increased by a step edge of  $\sim 10 \mu\text{m}$  along the boundaries between the flat part of the electrode and the rounded edges, due to a small error in the fabrication of the electrode.

After prolonged operation of the laser with the R16 cathode two distinct traces of spark erosion became apparent on both electrodes. With the previously used uniform field cathode, or ‘Ernst’ cathode, traces of spark erosion were distributed evenly across the discharge area on both electrodes, without showing signs of a local increase of the number and/or severity of the arcing.

The output energy of the laser has been measured with the R16 cathode both with and without using the additional current returns in the same manner as described above.

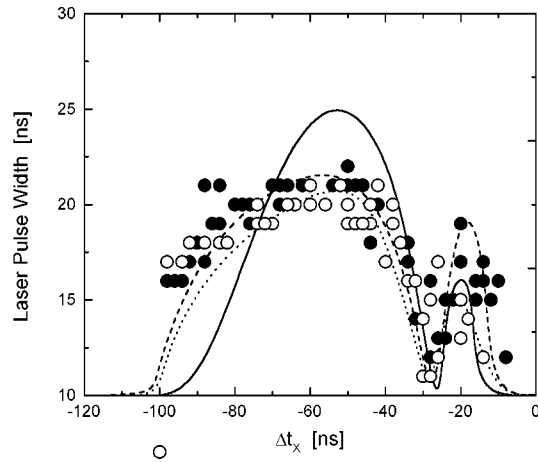


Figure 5.20: ArF laser pulse width (FWHM intensity) as a function of the pre-ionisation delay time  $\Delta t_x$  in the swing mode using different experimental configurations. Drawn line, no symbols: Ernst cathode (see figure 5.14).  $\circ$  and dotted line: R16 cathode.  $\bullet$  and broken line: R16 cathode with additional current returns. The curves through the results of the R16 cathode are the same as those in figure 5.19, scaled vertically to fit the results.

For an easier comparison with the earlier experiments the specific output energy of the laser pulses, defined as the output energy divided by the discharge volume, is shown in figure 5.19 when using the swing mode. It is clear that the overall behaviour of the output energy with respect to the pre-ionisation delay time  $\Delta t_x$  is equivalent in all cases.

Using the R16 cathode without the current returns results in a slightly higher specific output energy at short pre-ionisation delay times,  $\Delta t_x$  shorter than  $\sim 27$  ns. At delay times between  $\sim 27$  ns and  $\sim 65$  ns the specific output energy is a little less than in the case of the Ernst cathode, and at delay times longer than  $\sim 65$  ns a higher specific output is generated.

The increased output at short pre-ionisation delay times is probably caused by the increase in the specific input power, due to the lower discharge volume while operating the laser under otherwise unaltered circumstances. The lower specific output

power in the intermediate region is probably caused by a more severely decreased discharge quality compared to using the Ernst cathode, caused by the field disturbance along the electrode edges. At delays longer than 65 ns the increased gain due to the increased pumping power outweighs the optical losses of the decreased discharge quality, compared to the situation with the Ernst cathode in which case it is the other way round. The pulse widths show the same behaviour: for  $\Delta t_x$  between  $-27$  ns and  $-65$  ns the Ernst cathode yields longer pulses than the R16 cathode, in the other regimes the R16 cathode generates longer pulses, see figure 5.20.

Using the R16 cathode in combination with the current returns results in a significantly increased specific output energy, with respect to both situations. The laser pulse width is only slightly increased, compared to the case of the R16 cathode without the current returns. These effects indicate that the output energy of the laser is indeed heavily influenced by small changes in the self-inductance of the excitation circuit, but that the pulse length is more dependent of the quality of the electrodes.

## 5.5 Conclusions

The optical performance of the ArF laser has been studied using a number of different experimental set-ups. The combination of the pre-ionisation timing and the shape of the voltage pulse in the pre-breakdown phase is found to have a decisive influence on the output energy and the pulse length of the laser. The behaviour of the KrF laser proves to be equivalent under the same circumstances. The results are explained by considering the electron multiplication processes and the electron attachment of the fluorine in the gas mixture.

The optimum output energy and pulse length are obtained in the so-called swing mode when the pre-ionisation pulse coincides with the pre-pulse. In the swing mode the polarity of the pre-pulse is opposite to that of the main pulse, which causes a polarity reversal of the electrode voltage during the electron multiplication from the pre-ionisation electron density to the discharge breakdown level. The result is a more homogeneously spread charge distribution at the breakdown than a voltage pulse without polarity reversal. This causes a more stable and homogeneous discharge and hence a better laser performance.

Increasing the pumping power by decreasing the discharge volume is not found to be very effective. Decreasing the self-inductance of the laser vessel does result in a higher specific output and slightly longer laser pulses.

The results of these experiments may have been negatively influenced by the shape of the laser cathode, which causes a disturbance in the electric field of the discharge. These disturbances reduce the discharge homogeneity and decrease the laser performance.

## References

- [1] **Yu.A. Kudryavtsev and N.P. Kuzmina**, *Excimer gas-discharge tunable ArF laser*, Appl. Phys. **13**, 107–108 (1977).
- [2] **R. Burnham and N. Djeu**, *Ultraviolet-preionized discharge-pumped lasers in XeF, KrF and ArF*, Appl. Phys. Lett. **29** (11), 707–709 (1976).
- [3] **R.C. Sze and T.R. Loree**, *Experimental studies of a KrF and ArF discharge laser*, IEEE J. Quantum Electron. **14** (12), 944–950 (1978).
- [4] **J.E. Andrew, P.E. Dyer and P.J. Roebuck**, *Improved energy output from discharge pumped ArF and KrCl lasers*, Opt. Comm. **49** (3), 189–194 (1984).
- [5] **K. Miyazaki, T. Hasama, K. Yamada, T. Fukatsu, T. Eura and T. Sato**, *Efficiency of a capacitor-transfer-type discharge excimer laser with automatic preionization*, J. Appl. Phys. **60** (8), 2721–2728 (1986).
- [6] **V.K. Belyaev, K.S. Gochelashvili, V.P. Degtyareva, R.M. Zakirov, V.I. Klimov, V.T. Mikhkel'soo, A.M. Prokhorov and V.K. Chevokin**, *Investigation of the spatial-temporal dependence of the radiation pattern from an ArF laser*, Sov. J. Quantum Electron. **19** (2), 119–122 (1989). [Kvantovaya Elektron. **16**, 183–188 (1989)].
- [7] **S. Nagai, H. Furuhashi, Y. Uchida, J. Yamada, A. Kono and T. Goto**, *Formation dynamics of excited atoms in an ArF laser using He and Ne buffer gases*, J. Appl. Phys. **77** (7), 2906–2911 (1995).
- [8] **A.A. Zhupikov and A.M. Razhev**, *Excimer ArF laser with an output energy of 0.5 J and He buffer gas*, Quantum Electron. **27** (8), 665–669 (1997). [Kvantovaya Elektron. **24** (8), 683–687 (1997)].
- [9] **J. Coutts and C.E. Webb**, *Stability of transverse self-sustained discharge-excited long-pulse XeCl lasers*, J. Appl. Phys. **59** (3), 704–710 (1986).
- [10] **R.S. Taylor**, *Preionization and discharge stability study of long optical pulse duration UV-preionized XeCl lasers*, Appl. Phys. B **41**, 1–24 (1986).
- [11] **R.S. Taylor and K.E. Leopold**, *Magnetic-spiker excitation of gas-discharge lasers*, Appl. Phys. B **59**, 479–508 (1994).
- [12] **J.C.M. Timmermans**, *Double discharge XeCl-laser*, PhD thesis, University of Twente, Enschede, The Netherlands (1995).



- [13] **H.M.J. Bastiaens, S.J.M. Peeters, X. Renard, P.J.M. Peters and W.J. Witteman**, *Long pulse operation of an X-ray preionized molecular fluorine laser excited by a prepulse-main pulse system with a magnetic switch*, Appl. Phys. Lett. **72** (22), 2791–2793 (1998).
- [14] **W.J. Sarjeant, A.J. Alcock and K.E. Leopold**, *Constant E/N pumping of high-power rare-gas halide lasers*, IEEE J. Quantum Electron. **13**, 104D–106D (1977).
- [15] **A.E. Greene and C.A. Brau**, *Theoretical studies of UV-preionized transverse discharge KrF and ArF lasers*, IEEE J. Quantum Electron. **14** (12), 951–957 (1978).
- [16] **T.R. Loree, K.B. Butterfield and D.L. Barker**, *Spectral tuning of ArF and KrF discharge lasers*, Appl. Phys. Lett. **32** (3), 171–173 (1978).
- [17] **Ch.A. Brau**, *Rare gas halogen excimers*, In: Excimer lasers, Ch.K. Rhodes, ed., Topics in applied physics **30**, ch. 4, 87–137, Springer Verlag, Berlin, 2nd enlarged edition, (1984).
- [18] **A.A. Zhupikov and A.M. Razhev**, *Excimer KrF laser with He buffer gas, 0.8 J energy, and 2% efficiency*, Quantum Electron. **28** (8), 667–669 (1998). [Kvantovaya Elektron. **25** (8), 687–689 (1998)].
- [19] **G.J. Ernst**, *Uniform-field electrodes with minimum width*, Opt. Comm. **49** (4), 275–277 (1984).
- [20] **K. Midorikawa, M. Obara and T. Fujioka**, *X-ray preionization of rare-gas-halide lasers*, IEEE J. Quantum Electron. **20** (3), 198–205 (1984).
- [21] **M. Steyer and H. Voges**, *Parametric study of x-ray preionized high-pressure rare gas halide lasers*, Appl. Phys. B **42**, 155–160 (1987).
- [22] **J.W. Gerritsen**, *High-efficiency operation of an x-ray preionized avalanche discharge XeCl laser*, PhD thesis, University of Twente, Enschede, The Netherlands (1989).
- [23] **F.A. van Goor, W.J. Witteman, J.C.M. Timmermans, J. van Spijker and J. Couperus**, *High average power XeCl laser with x-ray pre-ionization and spiker-sustainer excitation*, In: High-power gas and solid state lasers, M. Bohrer, T. Letardi, D. Schuöcker and H. Weber, eds., Proceedings of SPIE **2206**, 30–40 (1994).
- [24] **H.M.J. Bastiaens**, Private communication.
- [25] **M. Trentelman**, *Gas discharge excited XeF laser*, PhD thesis, University of Twente, Enschede, The Netherlands (1993).
- [26] **J.I. Levatter and S.C. Lin**, *Necessary conditions for the homogeneous formation of pulsed avalanche discharges at high gas pressures*, J. Appl. Phys. **51** (1), 210–222 (1980).
- [27] **N. Brenning, I. Axnäs, J.O. Nilsson and J.E. Eninger**, *High-pressure pulsed avalanche discharges: formulas for required preionization density and rate for homogeneity*, IEEE Tr. Plasma Sci. **25** (1), 83–88 (1997).
- [28] **M. Makarov, J. Bonnet and D. Pigache**, *High efficiency discharge-pumped XeCl laser*, Appl. Phys. B **66**, 417–426 (1998).

- 
- [29] **M.R. Osborne**, *Rare-gas-halide discharge stability*, Appl. Phys. B **45**, 285–291 (1988).
- [30] **M.J. Kushner**, *Microarcs as a termination mechanism of optical pulses in electric-discharge-excited KrF excimer lasers*, IEEE Tr. Plasma Sci. **19** (2), 387–399 (1991).
- [31] **R. Dreiskemper and W. Bötticher**, *Current filamentation of strongly preionized high pressure glow discharges in Ne/Xe/HCl mixtures*, IEEE Tr. Plasma Sci. **23** (6), 987–995 (1995).
- [32] **J. Hsia**, *A model for UV preionization in electric-discharge-pumped XeF and KrF lasers*, Appl. Phys. Lett. **30** (2), 101–103 (1977).
- [33] **P.J. Chantry**, *Negative ion formation in gas lasers*, In: Applied Atomic Collision Physics, E.W. McDaniel and W.L. Nighan, eds., volume 3, Gas Lasers, 35–70, Academic Press, New York, NY, (1982).
- [34] **F.A. van Goor, J.C.M. Timmermans and W.J. Witteman**, *The influence of charge-mode operation of a XeCl laser on the beam profile*, Opt. Comm. **124**, 56–62 (1996).

## Chapter 6

# Intermediate pulse length operation and modelling of the laser, using a minimum self-inductance of the peaking circuit

In chapter 5 it has been shown that the self-inductance of the excitation circuit has a large influence on the laser performance. In our set-up the self-inductance of the main circuit cannot be reduced further than is done in section 5.4.

However, Bastiaens et al. have shown that a set-up with a minimum self-inductance of the peaking circuit can already yield considerably longer laser pulses than we were able to generate using the set-ups of chapter 5 [1,2].

A low self-inductance of the peaking circuit results in a short current rise time in the first stages of the discharge, which allows the peaking circuit to deliver energy to the discharge before the main current has reached any significant value. This decreases the start-up time of the laser pulse. A decrease of the current rise time also causes a denser cathode hot spot structure, which increases the homogeneity of the discharge and thus leads to a longer laser pulse [3–6].

By placing the peaking capacitors inside the laser vessel, next to the discharge, Bastiaens et al. obtained 45 ns (FWHM) ArF pulses from a gas mixture of 3 mbar F<sub>2</sub>, 250 mbar Ar in He at a total gas pressure of 5 bar. For the F<sub>2</sub> laser they even achieved pulse lengths of up to 70 ns in the same set-up [1, 2].

Following the successful research of Bastiaens et al. we modified our set-up in order to minimise the self-inductance of the peaking circuit.

In this chapter we present some experimental results obtained with the modified set-up. The second part of the chapter concerns the results of a numerical simulation of the laser. A short description of the model used is given in appendix B. In the third part of this chapter we discuss the results of the modelling, compared with the experimental results.

## 6.1 Experimental set-up

The modifications of the experimental set-up, as compared to the set-up described in chapter 5, may be seen in figures 6.1 and 6.2.

The laser cathode is a brass uniform field electrode [7], the nickel plated aluminium anode is flat. The interelectrode distance is 12 mm, resulting in a discharge volume of approximately  $60 \times 0.7 \times 1.2 \text{ cm}^3$  ( $l \times w \times h$ ). To reduce the self-inductance of the main circuit, the laser vessel is fitted with additional current returns. The current returns consist of aluminium rods, fastened to copper supports that are connected to the laser anode via elastic pressure contacts.

The peaking circuit is formed by 10 ceramic capacitors (MuRata DHS 461-Z-30) of  $C_{\text{cap}} = 460 \text{ pF}$  (at 0 V) mounted on the copper supports inside the laser vessel and connected to the laser cathode by copper leads. The peaking capacitors and the aluminium rods are distributed evenly along the cathode length, see figure 6.2. The high voltage sides of the peaking capacitors are fitted with corona rings to minimise the chance of arcing between the capacitors and the aluminium rods.

The laser resonator consists of a full reflector with a concave radius of 6 m and a plane 70 % reflection outcoupler. Both mirrors are placed outside the laser vessel, to avoid contact with the fluorine containing gas mixture. The MgF<sub>2</sub> windows in the laser vessel are aligned with the laser mirrors to minimise reflection losses.

The set-up is equipped with a liquid nitrogen gas purifier, operated at a temperature of the cold trap of 90 K. During the experiments the gas mixture is continuously

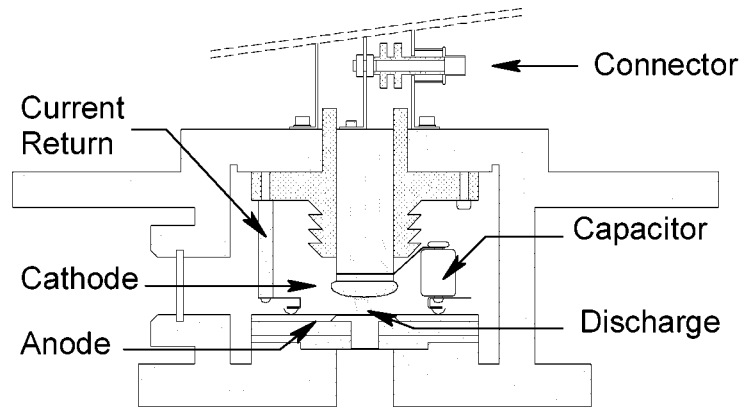


*Figure 6.1: A cross section of the modified laser head, showing the construction of the peaking capacitors and the current return rods which reduce the self-inductance of the circuit. The peaking capacitors and the current return rods are evenly spaced along the cathode length, see figure 6.2*

flowed through the purifier to freeze out impurities. This increases the operational lifetime of the gas and decreases contamination of the windows as well as absorption losses to impurities [8–10].

The positions of the current and voltage probes are left equal to the previous situation, see figure 6.3. There are no probes connected to the electrodes inside the laser vessel because the signal-to-noise ratio of probes inside the laser was found to be too high to yield reliable results. Furthermore, the probes, made with plastic-clad resistors or mylar insulation, deteriorate rapidly under the influence of the fluorine and the UV-radiation inside the laser vessel, severely contaminating the laser gas mixture in the process.

Since there are no probes connected directly to the electrodes the actual electrode voltage and discharge current remain unknown. Calculating the electrode voltage by a straightforward correction of the measured voltage  $V_P$  with respect to the self-inductance, as is done in chapter 5, is impossible due to the position of the peaking circuit within the measuring circuit. We therefore rely on the signals from the probes

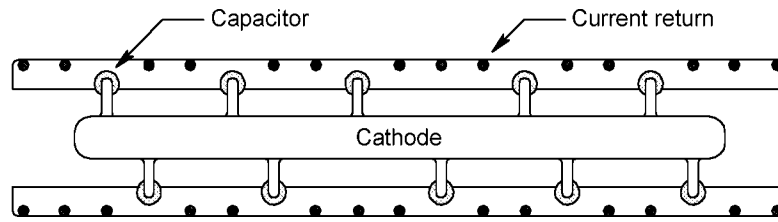


Figure 6.2: A bird's eye view of the construction of the modified laser head, showing the distribution of the peaking capacitors and the current return rods on the copper carriers along the cathode. The corona rings on the capacitors are not shown.

outside the laser vessel to obtain information on the behaviour of the discharge. Although the measured current  $I_{\text{main}}$  does not represent the actual discharge current, variations in the discharge impedance, such as the results of short-circuiting filaments and arcs can still be found quite clearly, see the results in chapter 7.

Nevertheless, from here onwards we only present the measured data, unless explicitly stated otherwise.

## 6.2 Experimental results

In order to investigate some of the qualities of the modified set-up for obtaining long laser pulses, we performed a few “quick-and-dirty” experiments<sup>1</sup> using the gas mixture Bastiaens et al. found to yield the best laser performance [11]. This gas mixture consists of 3 mbar  $F_2$ , 250 mbar Ar both in He and in Ne buffer gases at a total gas pressure of 5 bar [2].

The laser is operated in the swing mode [Sect. 4.3] with a pre-pulse charging voltage of  $V_{\text{PP}} = 30$  kV and a PFN voltage of  $V_{\text{PFN}} = 32$  kV. The X-ray source is charged to  $V_{\text{XP}} = 28$  kV, as in chapter 5. To decrease the electrode wear by arcing discharges the PFN-capacitance is reduced to  $C_{\text{PFN}} = 162$  nF.

Under these experimental circumstances a significant increase in the performance of the laser is found, compared with the results of chapter 5. The optimum laser pulse

<sup>1</sup>Measuring while changing the experimental parameters after every few shots in order to get a rough impression of the behaviour of the set-up, without attempting to obtain detailed information from series of results. However, each result was proven to be reproducible.

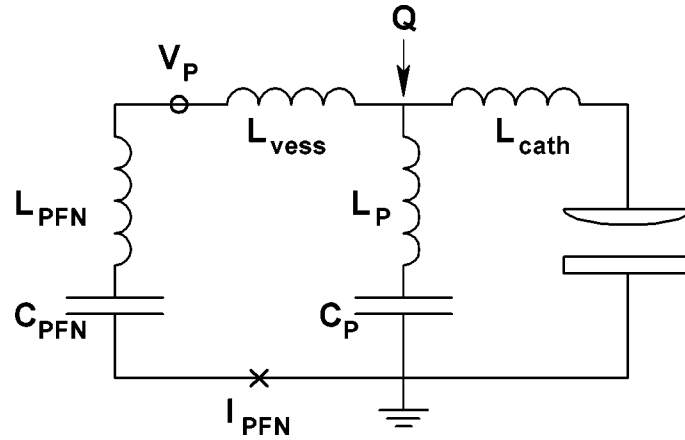


Figure 6.3: The equivalent circuit of the modified set-up, showing the locations of the different circuit components and of the measuring probes.  $C_{\text{PFN}}$ : PFN capacitance.  $L_{\text{PFN}}$ : Self-inductance of the PFN and of the main switch.  $V_{\text{P}}$ : Main voltage probe.  $I_{\text{main}}$ : Current probe.  $L_{\text{vess}}$ : Self-inductance of the laser vessel, up to the connection of the peaking circuit.  $L_{\text{P}}$ : Self-inductance of the peaking circuit, up to the connection of the peaking circuit.  $C_{\text{P}}$ : Peaking capacitance.  $L_{\text{cath}}$ : Self-inductance of the main circuit below the connection of the peaking capacitors. The connection of the peaking capacitors to the cathode is indicated with the letter  $Q$ .

length found in chapter 5 is approximately 26 ns [Fig. 5.14 on page 77] and the optimum specific output energy is 550 mJ/ℓ [Fig. 5.19 on page 83]. However, these results are found under different conditions.

When using He as the buffer gas in the modified set-up the laser pulse length is found to be increased to approximately 32 ns (FWHM), see figure 6.4. In this situation output energies of up to  $E_{\text{out}} = 97$  mJ/pulse, or 1.9 J/ℓ, are obtained. With the Ne-buffered gas mixture the measured pulse lengths are up to 48 ns (FWHM), see figure 6.5. The output energy in this case is even increased up to  $E_{\text{out}} = 181$  mJ/pulse, or 3.6 J/ℓ.

These values for the specific output energy are in the same range as the figures reported in the literature for short-pulse ArF lasers, between 2 J/ℓ and 5 J/ℓ. How-

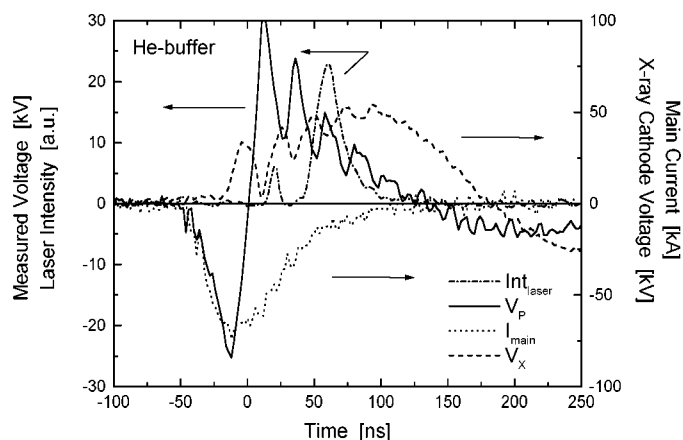


Figure 6.4: Typical measured wave forms of an ArF laser pulse using He for the buffer gas. Pulse length: 25 ns (FWHM). Output energy:  $E_{\text{out}} = 90 \text{ mJ}$  ( $1.8 \text{ J}/\ell$ ). The first peak in the optical signal originates from the red atomic fluorine laser ( $\lambda = 713 \text{ nm}$ ). Gas mixture: 5 bar,  $F_2 : Ar : He = 3 : 250 : \text{Rest}$  [mbar].

ever, the average laser pulse length in these papers is approximately 12 ns, e.g. see refs. [9, 12–14].

The optical signal in figure 6.4 may be seen to consist of a small pulse leading a larger pulse by approximately 25 ns. The first peak originates from the lasing of atomic fluorine ( $\lambda = 713 \text{ nm}$ ), the second peak is the ArF laser pulse proper. Although it is not known to have any effect on the kinetics of the ArF\* laser, the atomic F laser has a sufficient intensity to be measured by the photodiode behind the ArF laser line filter. Since the atomic F laser is efficiently quenched by Ne it is not observed when a few percents Ne are added to the gas mixture, e.g. see figure 5.10 on page 73 and figures 6.5 and 6.6.

Several authors have discussed the ideal buffer gas when optimising an ArF laser with respect to the output power or to the laser efficiency, i.e. He, Ne or a mixture of both gases [12, 14–18]. Generally speaking, it is claimed in the literature that there are no great differences in the laser performance when one buffer gas is replaced by the other. According to Nagai et al. [16] and Ohwa and Obara [17] this is due to the fact



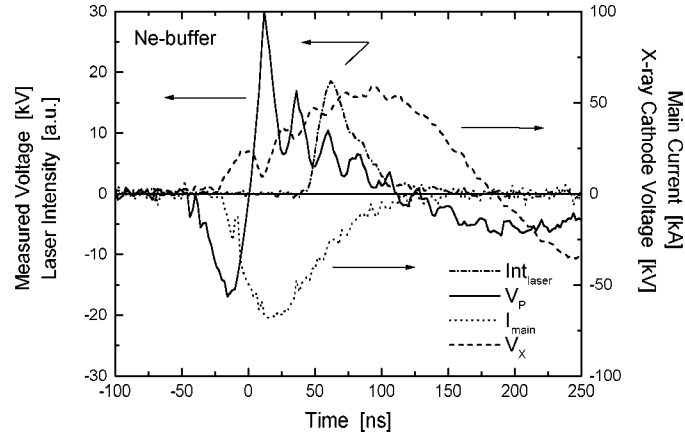


Figure 6.5: Typical measured wave forms of an ArF laser pulse using Ne for the buffer gas. Pulse length: 38 ns (FWHM). Output energy:  $E_{\text{out}} = 161 \text{ mJ}$  (3.2 J/l). Gas mixture: 5 bar,  $F_2 : \text{Ar} : \text{He} : \text{Ne} = 3 : 250 : 58 : \text{Rest}$  [mbar].

that when using Ne the formation of  $\text{ArF}^*$  molecules is twice as efficient as in He-buffered mixtures, while the optical extraction efficiency of the He-buffered mixture is almost twice as high as when using Ne. Thus, the intrinsic efficiencies of both cases are almost equivalent.

However, discharges in Ne-based gas mixtures are more stable than discharges in He-buffered gas mixtures [17, 19, 20]. Therefore longer laser pulses and thus higher output energies may be obtained when using Ne than when using He, see figures 6.4, 6.5 and 6.6.

In the case of the Ne-buffered gas mixture we found that the performance of the laser increases both with respect to the pulse length and to the output energy when the nitrogen pressure in the rail gap is decreased from 1.5 bar to 0.5 bar, see figure 6.6. This effect may be caused by a lower energy dissipation in the discharge inside the rail gap, so that a higher pumping power is transferred to the discharge [21]. The better performance may also be the result of the lower rail gap breakdown voltage. This results in a lower laser breakdown voltage [Sec. 4.3], which reduces the amplitude of the current and voltage oscillations across the discharge with respect to the main

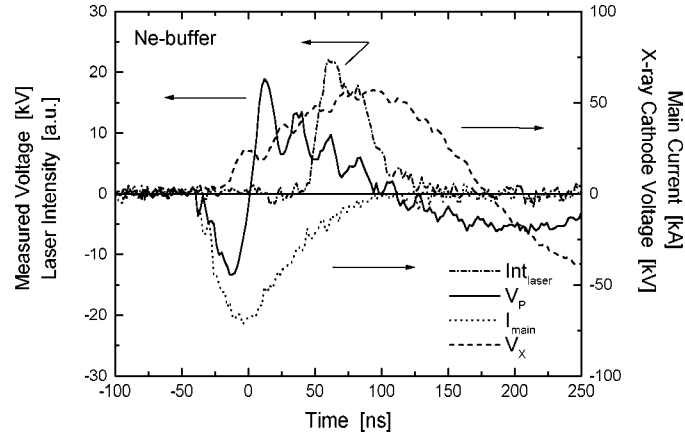


Figure 6.6: Typical measured wave forms of an ArF laser pulse using He for the buffer gas. Gas mixture: 5 bar,  $F_2 : Ar : He : Ne = 3 : 250 : 58 : Rest$  [mbar]. Pulse length: 43 ns (FWHM). Output energy:  $E_{out} = 177$  mJ (3.5 J/ℓ). Rail gap pressure:  $P_{RG} = 0.5$  bar, flowing at 5 ℓ/min. Compare with figure 6.5 in which  $P_{RG} = 1.5$  bar, 5 ℓ/min flow.

current and voltage pulse. Thus the discharge stability and the output energy are increased, see section 6.3 below.

### 6.3 Kinetic modelling

In order to study the behaviour of the gas discharge and of the laser performance, we used a kinetic model to calculate the behaviour of several characteristic features of the laser pulse when using He as the buffer gas. The results also served to determine the difference between the measured voltage and current signals and the actual values for the discharge.

The used kinetic model is developed in the group of prof. dr A.P. Napartovich by A.V. Demyanov and co-workers of the Troitsk Institute for Innovative and Thermonuclear Research (TRINITI), Troitsk, Moscow Province, Russia. The simulations were

performed in close cooperation with us.

A description of the kinetic model and an overview of the reactions considered during the calculations are given in appendix B. In this section we present some results of the modelling which are interesting for the experimental research. A more exhaustive account of the results of the calculations is given in ref. [22].

The model described in appendix B is used to simulate the operation of the laser for the experimental conditions of figure 6.4. The model yields the voltage across the discharge and the current flowing through it. In order to enable a comparison with the experimental results, the current and voltage at the locations of the probes  $V_P$  and  $I_{\text{main}}$  are calculated as well.

In the model the temporal variations of the number densities of all species of the considered reactions are calculated. Because of the division of the discharge volume in several parallel layers, the spatial distribution of the different species is obtained as well. Since the rate equations for the optical transitions are incorporated in the model, the spatial behaviour of the laser pulse may also be calculated [22].

In the parallel resistor model, see appendix B, all discharge layers are assumed to be uniform during the discharge pulse. However, in the experiments the discharge is observed to break down into filaments and arcs. This may be accounted for in the model by considering an additional layer ('the filament') with slightly different conditions than the other layers and performing the calculations for this filament-layer in parallel with those for the bulk of the discharge.

During the simulation of the ArF laser the filament-layer is incorporated like it was positioned on the optical axis of the discharge volume. The initial electric field strength and electron density in the filament are determined separately from the bulk of the discharge. The area occupied by the filament may be adjusted as well. A comparison of the results after each iteration step shows how the different conditions influence the discharge in the filament-layer in relation to the bulk of the discharge.

### 6.3.1 Calculated results

For the calculations of the behaviour of the laser the circuit of figure 6.3 is used. The values of the components of figure 6.3 are taken to be:  $L_{\text{PFN}} = 8 \text{ nH}$ ,  $L_{\text{vess}} = 15 \text{ nH}$ ,  $L_P = 2.4 \text{ nH}$ ,  $L_{\text{cath}} = 1.0 \text{ nH}$ ,  $C_{\text{PFN}} = 162 \text{ nF}$  and  $C_P = 4.6 \text{ nF}$ . The values of the self-inductances are best-fit values, adapted from estimates based on the geometry of the set-up. However, the combined value of  $L_{\text{PFN}} + L_{\text{vess}} + L_{\text{cath}} = 24 \text{ nH}$  is measured quite accurately from the oscillation time of the current from the PFN.

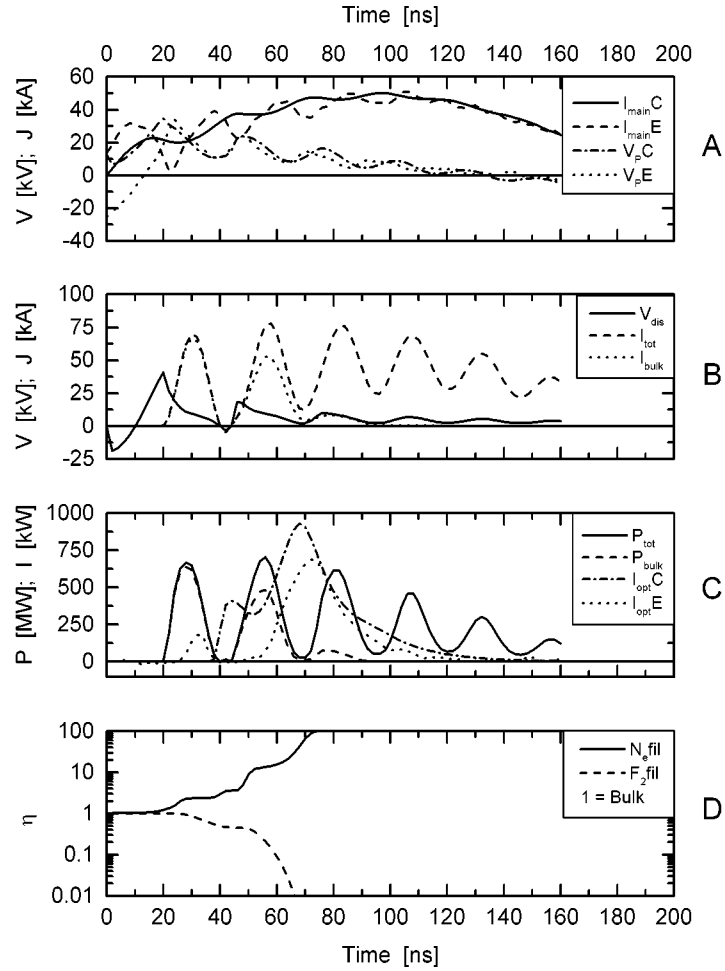


Figure 6.7: The result of the model calculations with the best-fit values for the experimental set-up. Calculated output energy  $E_{\text{out}} = 158 \text{ mJ}$ . See the text for the legend and the explanation of the curves.

The entire voltage pulse of the swing mode is rather difficult to simulate, because the voltage pulse strongly oscillates before the discharge is ignited, see section 4.3. Therefore, the calculations start at the moment the rail gap breaks down, i.e. at the lowest measured voltage  $V_P$ .

To simulate the growing filamentation of the discharge the electric field inside the filament-layer is increased over that of the bulk of the discharge. Assuming an initial reduction of the electric field strength of  $\Delta E_{\text{fil}}/E_{\text{bulk}} = 0.8\%$  and a filament area of  $1.1 \text{ cm}^2$  yields the best agreement with the experimental results. The area of the filament is an educated guess, based on pictures of the discharge and on values found in literature, e.g. see refs. [23, 24]. The electric field disturbance may be thought of as resulting from the appearance of hot spots on the cathode.

The discharge in the filament area does not contribute to the optical laser field, nor does it absorb or scatter the radiation in the model calculations. The former effect seems reasonable, however the latter may be a somewhat optimistic assumption, since the disturbing effects of filaments on the optical output are well known qualitatively [24] and imprints of the laser beam on thermofax paper clearly show disturbances of the laser beam due to filamentary structures. Additionally, even the presence of hot spots on the cathode can be seen in the near field of the laser beam of a long pulse XeCl laser [25].

The results of the calculations in the above described case are shown in figure 6.7. The calculated results are compared to the experimental results of figure 6.4. The curves in the figure are the following:

- $I_{\text{main}}\text{C}$ : Calculated current at the measuring probe  $I_{\text{main}}$ .
- $I_{\text{main}}\text{E}$ : Experimentally measured current.
- $V_P\text{C}$ : Calculated voltage at the measuring probe  $V_P$ .
- $V_P\text{E}$ : Experimentally measured voltage.
- $V_{\text{dis}}$ : Calculated discharge voltage (including the filament).
- $I_{\text{tot}}$ : Total calculated discharge current (including the filament).
- $I_{\text{bulk}}$ : Current through the homogeneous bulk of the discharge.
- $P_{\text{tot}}$ : Total calculated input power into the discharge.
- $P_{\text{bulk}}$ : Calculated input power into the homogeneous bulk of the discharge.
- $I_{\text{opt}}\text{C}$ : Calculated optical intensity.
- $I_{\text{opt}}\text{E}$ : Experimentally measured optical intensity (Note:  $I_{\text{opt}}\text{E}$  is presented in arbitrary units, not in [kW]).

$N_e$ fil: Calculated electron number density in the filament relative to that in the bulk of the discharge.

$F_2$ fil: Calculated  $F_2$  molecule number density in the filament relative to that in the bulk of the discharge.

In figure 6.7.A it may be seen that the calculated and the measured main current and voltage pulses overlap, indicating that the total self-inductance is a reasonable good fit. However, both in the current and the voltage pulse the frequency of the secondary oscillation is different between the calculated and the experimental wave forms.

In figures 6.7.B and C strong oscillations of the discharge voltage and the discharge current are clearly visible, which lead to a pulsed power input into the discharge. The result of this is that the optical output intensity also shows a fluctuation. The optical intensity is calculated with an estimated optical loss of 20 % per round trip in addition to the outcoupled fraction of the laser beam, in order to account for the absorption and scattering losses at the  $MgF_2$  windows and the non-pumped optical path length inside the resonator.

From figure 6.7.D it is clear that the electron and the fluorine number densities in the filament strongly deviate from the values in the (centre of the) bulk of the discharge. This indicates the formation of discharge filaments and arcs.

In figures 6.7.B and C the effects of the filaments are visible in the difference between the current and voltage pulses calculated for the total of the discharge and those calculated for the bulk of the discharge, since the latter pulses represent the homogeneous part of the discharge and the former results also incorporate the filament. It is clear that, as the discharge proceeds, the filamentation becomes worse and an increasing amount of energy is channeled away from the homogenous part of the discharge. Thus increasingly less power is available for the excitation of the laser causing the optical pulse to end prematurely.

The effects of the plasma filamentation become clearer when figure 6.7 is compared to the results of a discharge without filaments as shown in figure 6.8. Obviously, the values for the entire discharge and those for the homogeneous bulk are equal in this case. When there is no filamentation all available power is used in the discharge so that the calculated optical pulse is almost as long as the discharge pulse and the intensity and output energy are much higher than in the case of a discharge with filaments [Fig. 6.7]. The oscillations of the input power are clearly visible in the form of intensity fluctuations of the optical output pulse.

The calculated laser output energy is 158 mJ in the case of figure 6.7 while in the

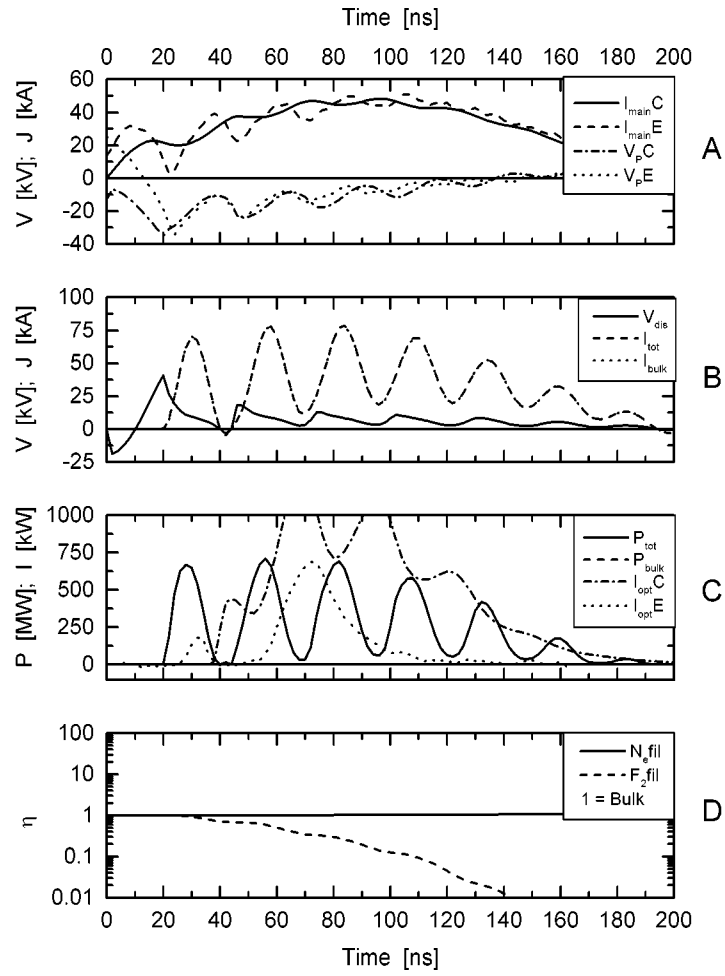


Figure 6.8: The result of the model calculations for the situation of figure 6.7 but without filamentation. Calculated output energy  $E_{out} = 381$  mJ.

case of no filamentation (figure 6.8) the calculated output is even up to 381 mJ. Both values are significantly higher than the experimental result of 90 mJ.

When the optical losses in the model are increased from 20 % in the case of figure 6.7 to 30 %, the calculated output decreases to 121 mJ, which is still higher than the experimental result. Increasing the optical losses even further is thought to be unrealistic.

The calculated optical output of a set-up with flat, parallel electrodes decreases when the filament area in the model is increased [22, 26]. However, for the case of profiled electrodes the filament should consist of several layers to account for the variation of the electric field due to the electrode-shape. This gives so much freedom in the choices of the parameters of the filament-layers, that a calculated result would be of little value.

From figures 6.7 and 6.8 we may see that the deviation of the electron number density and the fluorine depletion in the filament occur faster during an increase in the discharge current. It is therefore interesting to study the effect of an increased self-inductance of the peaking circuit. In figure 6.9 the results are shown of a simulation of the laser with a self-inductance of the peaking circuit that is twice the self-inductance of the experimental set-up,  $L'_P = 2L_P = 4.8$  nH. In figure 6.10 the results are shown of a simulation of the laser with a self-inductance of the peaking-circuit of zero,  $L''_P = 0$  nH. The calculated output energies of the cases of  $L'_P = 2L_P$  and  $L''_P = 0$  are 113 mJ and 219 mJ, respectively, compared to  $E_{\text{out}} = 158$  mJ in the case of figure 6.7.

A comparison between figures 6.7, 6.9 and 6.10 shows that the self-inductance of the peaking circuit has a profound effect on the behaviour of the laser. With a self-inductance of  $L''_P = 0$  nH the filamentation of the discharge is seen to proceed more slowly and evenly than when  $L_P = 2.4$  nH [Fig. 6.7].

The growth of the filamentation in the case of  $L'_P = 4.8$  nH [Fig. 6.9] shows a clear step-like behaviour at each current pulse through the discharge. The filamentation in this case proceeds at an average rate which is a little slower than that of the experimental set-up with  $L_P = 2.4$  nH [Fig. 6.7].

The total power deposition in the discharge is higher when the self-inductance of the peaking circuit is reduced. The fraction of the power delivered to the homogeneous bulk of the discharge, compared to the total deposited power, also decreases more rapidly in the case of a high self-inductance of the peaking circuit than in the situation of a low self-inductance. Furthermore, in the case of a high self-inductance the second power pulse of the pulse-train is delivered to the discharge at a time when the filaments already have developed to a degree that only a poor laser pulse may be generated.



A difference between zero self-inductance of the peaking circuit and a high self-inductance can clearly be seen in the optical pulse, which, of course, is of interest to us. In the case of zero self-inductance the laser pulse starts almost immediately after the discharge breakdown, having a pulse length of approximately 60 ns. In the case of a large self-inductance the optical signal starts approximately 15 ns later and the pulse length is reduced to approximately 40 ns. The shorter start-up time of the pulse in the case of a low self-inductance is caused by the faster and higher power deposition in the discharge. These results show once again that the self-inductance of the set-up has a decisive influence on the behaviour of the laser.

The effects of the current rise time on the formation, the growth and the distribution of cathode hot spots, unfortunately, cannot be calculated in the present model. However, it is clear that a low self-inductance of the peaking circuit causes an increase in the stability of the discharge in its own right.

## 6.4 Comparison between experimental and calculated results

Although we cannot measure the actual discharge voltage and current, or calculate it from the experimental results, we can calculate the voltage at the connection between the cathode and the peaking circuit by accounting for the presence of  $L_{\text{vess}}$  in the measuring circuit. Since the self-inductance  $L_{\text{cath}} \ll L_{\text{vess}}$  this is expected to give a reasonable approximation of the discharge voltage.

In figure 6.11 a comparison is made between the results of the simulation and the experimental results when the voltage is calculated by

$$V_{\text{calc}} = V_{\text{P}} - L_{\text{vess}} \frac{dI_{\text{main}}}{dt} \quad (6.1)$$

and taking  $L_{\text{vess}} = 15 \text{ nH}$ , as is done in the model calculations.

The layout of figure 6.11 is similar to that of figures 6.7 to 6.10:

$I_{\text{main}}\text{C}$ : Calculated current at the measuring probe  $I_{\text{main}}$ .

$I_{\text{main}}\text{E}$ : Experimentally measured current.

$V_{\text{P}}\text{C}$ : Calculated voltage at the measuring probe  $V_{\text{P}}$ .

$V_{\text{P}}\text{E}$ : Experimentally measured voltage.

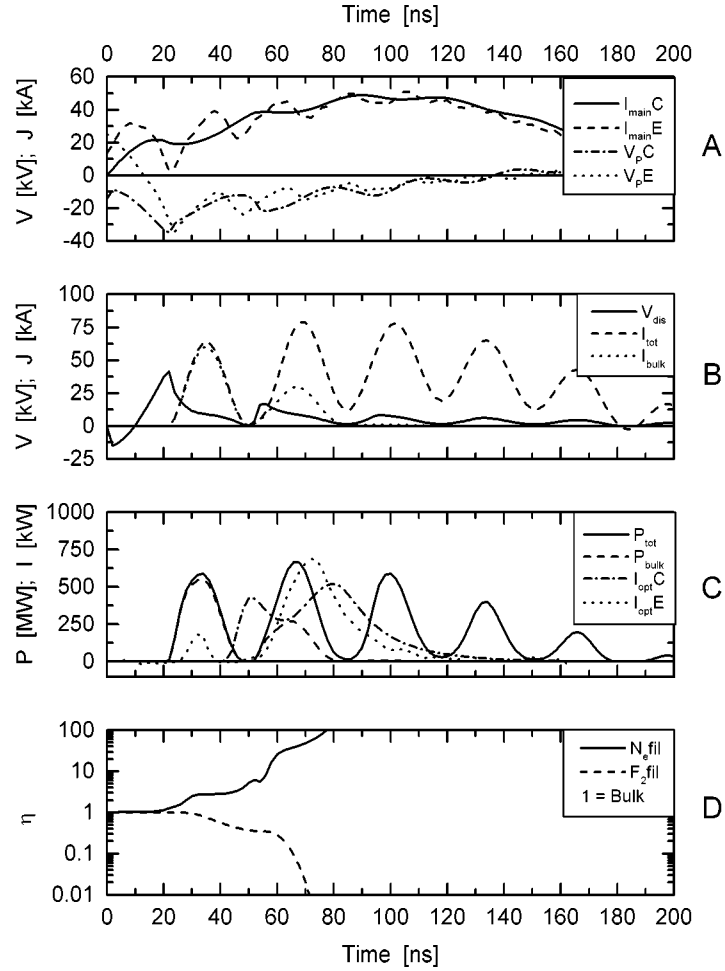


Figure 6.9: The result of the model calculations for the situation of figure 6.7 but with a twice as high self-induction of the peaking circuit,  $L_{\text{P}}^1 = 2L_{\text{P}} = 4.8 \text{ nH}$ . Calculated output energy  $E_{\text{out}} = 113 \text{ mJ}$ .

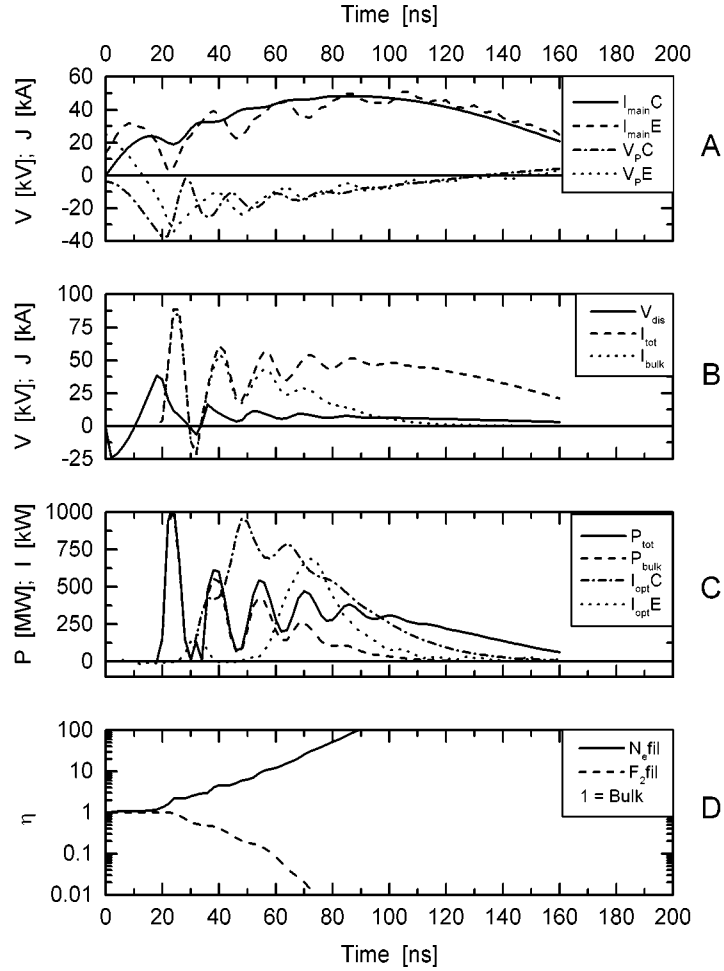


Figure 6.10: The result of the model calculations for the situation of figure 6.7 but with a self-induction of the peaking circuit of zero,  $L_P'' = 0$  nH. Calculated output energy  $E_{out} = 219$  mJ.

- $I_{\text{tot}}\text{C}$ : Total calculated discharge current (including filament).
- $I_{\text{main}}\text{E}$ : Experimental current at the measuring probe  $I_{\text{main}}$ .
- $V_{\text{dis}}\text{C}$ : Calculated discharge voltage (including filament).
- $V_{\text{calc}}\text{E}$ : Voltage at the connection between the cathode and the peaking circuit, calculated according to equation 6.1.
- $P_{\text{P}}\text{C}$ : Total calculated input power into the discharge, calculated at the location of the probe  $V_{\text{P}}$ ;  $P_{\text{P}}\text{C} = I_{\text{main}}\text{C} \times V_{\text{P}}\text{C}$ .
- $P_{\text{tot}}\text{C}$ : Total calculated input power into the discharge (including the filament).
- $I_{\text{opt}}\text{C}$ : Calculated optical intensity.
- $P_{\text{tot}}\text{E}$ : Total measured input power into the discharge, calculated by  $P_{\text{tot}}\text{E} = V_{\text{P}}\text{E} \times I_{\text{main}}\text{E}$ .
- $P_{\text{calc}}\text{E}$ : Total calculated input power into the discharge, calculated by  $P_{\text{calc}}\text{E} = V_{\text{calc}}\text{E} \times I_{\text{main}}\text{E}$ . Note the different vertical scales in panels C and D.
- $I_{\text{opt}}\text{E}$ : Measured optical intensity.

Figure 6.11 shows that the calculated discharge voltage  $V_{\text{calc}}$  exhibits strong oscillations similar to the result of the model. The fact that the input power  $P_{\text{calc}}\text{E}$  has large negative peaks proves that this simple approximation is not ideal. However, the optical signal  $I_{\text{opt}}\text{E}$  reaches a maximum after a peak in the input power and it shows has a very slight shoulder at the time of the next power peak.

The large negative peaks on  $P_{\text{calc}}\text{E}$  lead us to believe that the value taken for  $L_{\text{vess}}$  may be too large, although the approximation seems valid. A value of  $L_{\text{vess}} = 8 \text{ nH}$  is obtained by calculating the self-inductance from the geometry of the set-up. The current loop is calculated from the position of the probe to the connection of the peaking circuit to the cathode, while approximating the aluminium rods by a solid current return along the entire length of the electrodes, instead of taking a current path width of  $28 \times 1 \text{ cm}$ . When using  $L_{\text{vess}} = 8 \text{ nH}$ , the wave forms calculated from the experimental results are quite reasonable, see figure 6.12.

In figures 6.11 and 6.12 it may be seen that there is a difference between the oscillation times of the modelled discharge voltage and of  $V_{\text{calc}}\text{E}$ . This may have increased the discrepancies between the simulated optical pulse and the experimental result. The difference in the oscillation frequencies is probably caused by a small error in the estimates of the values of self-inductances of the peaking circuit.

A comparison between figures 6.11 and 6.12 shows that the modified voltage and power signals in figure 6.12 agree more to the simulated curves than those in figure 6.11. Especially the voltage  $V_{\text{calc}}E$  and the power  $P_{\text{calc}}E$  seem more realistic.

At the same time we may see in figures 6.11 and 6.12 that the behaviour of the experimentally found optical intensity quite closely follows the input power  $P_{\text{tot}}E$  which is calculated directly from the measured signals. The correspondence between the optical output and the calculated input power at the position of the probe  $V_P$  is less good in the results of the model calculations, which is probably caused by the initial values chosen for the current and voltage.

## 6.5 Conclusions

The modification of the experimental set-up, minimising the self-inductance of the peaking circuit, results in a large increase in the performance of the laser. The reasons for this success may lie in the fact that the current in the first stages of the discharge has a very short rise time, which results in a high pumping power density. An increased power density implies a higher production rate of  $\text{ArF}^*$  molecules, so that a higher degree of inversion is reached. This results in a larger fraction of the lasing molecules to be available for the generation of optical output. Hence more output energy is obtained. A short current rise time also favours the growth of a dense distribution of small hot spots, rather than a few large ones. This increases the discharge stability [3–6].

When using Ne as the buffer gas instead of He the laser performance increases dramatically, both with respect to the pulse length and with respect to the output energy. The probable cause of this is that Ne-buffered excimer discharges are more stable than He-buffered discharges, so that not only the output power can be generated during a longer pulse but at the same time the optical quality of the discharge remains higher. Thus the radiation field inside the resonator is disturbed less, which leads to a higher energy extraction.

The results of a kinetic model also show that a larger self-inductance leads to a lower laser performance. This is caused mainly by the growth of filaments.

This is mainly due to the fact that the oscillations of the peaking circuit are too long to generate a more or less continuous pumping power.

The strong oscillations of the voltage and the current from the peaking circuit across the discharge promote the growth of filaments, so that the discharge quality deteri-

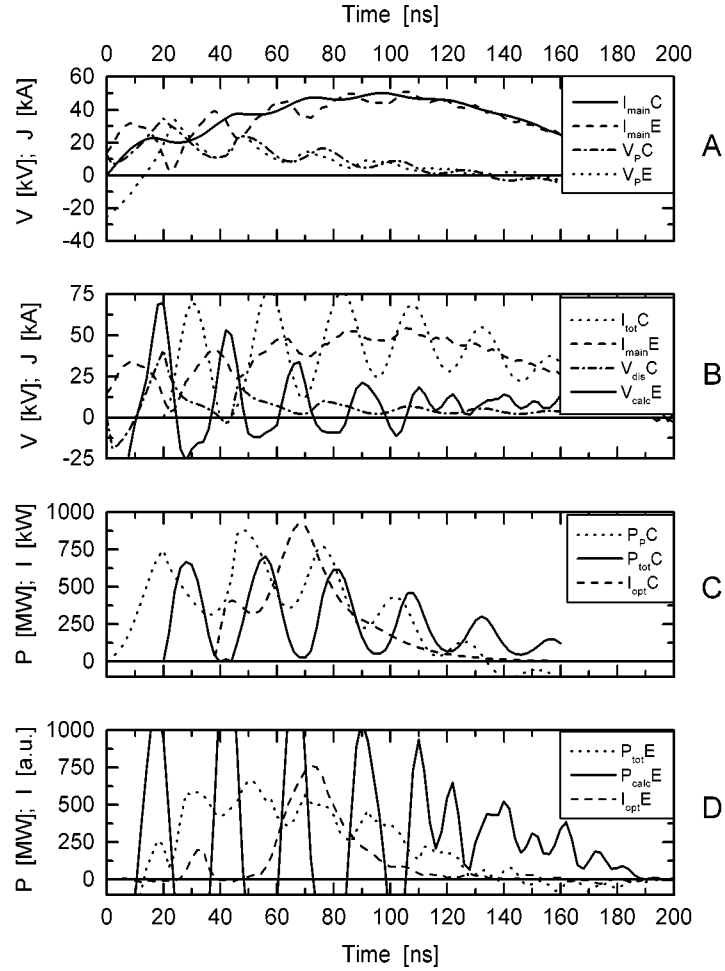


Figure 6.11: Comparison between the calculated results of figure 6.7 and the results of figure 6.4, with the experimental voltage corrected for  $L_{\text{vess}} dI_{\text{main}}/dt$  taking  $L_{\text{vess}} = 15 \text{ nH}$ . See the text for the legend and the explanation of the curves.

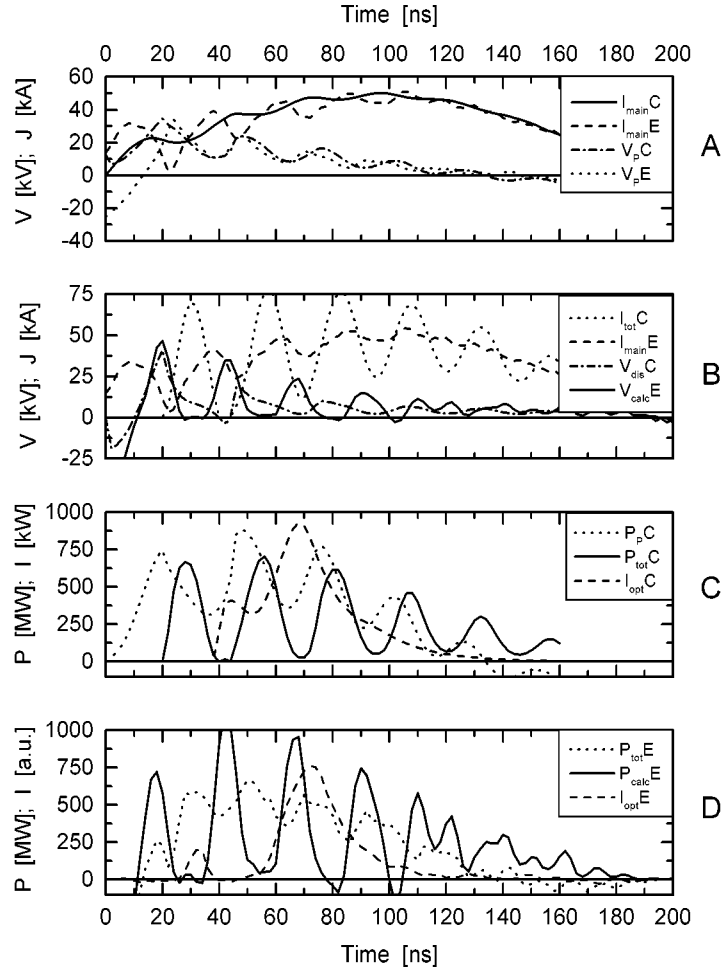


Figure 6.12: Comparison between the calculated results of figure 6.7 and the results of figure 6.4, with the experimental voltage corrected for  $L_{\text{vess}}dI_{\text{main}}/dt$  taking  $L_{\text{vess}} = 8 \text{ nH}$ .

orates. Decreasing the amplitude of the oscillations of the peaking circuit, e.g. by using lower breakdown voltages, may thus increase the discharge quality and hence the laser performance.

A comparison between the results of the model calculations and the experimental data shows that a straightforward ‘correction’ of the measured voltage with respect to the self-inductance of the laser vessel may be used to obtain a glimpse of the behaviour of the discharge voltage. Although the ‘corrected’ voltage yields no conclusive evidence, since the self-inductance of the laser vessel is not accurately known, the results may be used to explain the behaviour of the laser pulse.

## References

- [1] **H.M.J. Bastiaens, S.J.M. Peeters, X. Renard, P.J.M. Peters and W.J. Witteman**, *Long pulse operation of an X-ray preionized molecular fluorine laser excited by a prepulse-main pulse system with a magnetic switch*, Appl. Phys. Lett. **72** (22), 2791–2793 (1998).
- [2] **H.M.J. Bastiaens, S.J.M. Peeters, X. Renard, P.J.M. Peters and W.J. Witteman**, *Long pulse operation of a X-ray preionized F<sub>2</sub> and ArF laser excited by a prepulse-main pulse system with a magnetic switch*. Poster P38 at the 11th symposium Plasma Physics and Radiation Technology, Onderzoeksschool CPS and Section Plasma- and Gas Discharge Physics of the Netherlands Physical Society NNV, Lunteren, The Netherlands, (1998).
- [3] **R. Dreiskemper, G. Schröder and W. Böttcher**, *Light emission during cathode sheath formation in preionized high-pressure glow discharges*, IEEE Tr. Plasma Sci. **23** (2), 180–187 (1995).
- [4] **R. Dreiskemper and W. Böttcher**, *Current filamentation of strongly preionized high pressure glow discharges in Ne/Xe/HCl mixtures*, IEEE Tr. Plasma Sci. **23** (6), 987–995 (1995).
- [5] **M. Makarov**, *Effect of electrode processes on the spatial uniformity of the XeCl laser discharge*, J. Phys. D: Appl. Phys. **28**, 1083–1093 (1995).
- [6] **M. Makarov, J. Bonnet and D. Pigache**, *High efficiency discharge-pumped XeCl laser*, Appl. Phys. B **66**, 417–426 (1998).
- [7] **G.J. Ernst**, *Uniform-field electrodes with minimum width*, Opt. Comm. **49** (4), 275–277 (1984).
- [8] **S. Ito, T. Saito and A. Tada**, *A new gas purifier for ArF excimer lasers*, Rev. Sci. Instrum. **67** (3), 658–661 (1996).



- 
- [9] **T. Saito, S. Ito and A. Tada**, *Long lifetime operation of an ArF-excimer laser*, Appl. Phys. B **63**, 229–235 (1996).
- [10] **T. Saito and S. Ito**, *Gas contaminant effect in a discharge-excited ArF excimer laser*, Appl. Phys. B **66**, 579–583 (1998).
- [11] **H.M.J. Bastiaens**, Private communication.
- [12] **J.E. Andrew, P.E. Dyer and P.J. Roebuck**, *Improved energy output from discharge pumped ArF and KrCl lasers*, Opt. Comm. **49** (3), 189–194 (1984).
- [13] **K. Miyazaki, T. Hasama, K. Yamada, T. Fukatsu, T. Eura and T. Sato**, *Efficiency of a capacitor-transfer-type discharge excimer laser with automatic preionization*, J. Appl. Phys. **60** (8), 2721–2728 (1986).
- [14] **A.A. Zhupikov and A.M. Razhev**, *Excimer ArF laser with an output energy of 0.5 J and He buffer gas*, Quantum Electron. **27** (8), 665–669 (1997). [Kvantovaya Elektron. **24** (8), 683–687 (1997)].
- [15] **A.M. Bořchenko, V.I. Derzhiev, A.G. Zhidkov and S.I. Yakovlenko**, *Kinetic model of an ArF laser*, Sov. J. Quantum Electron. **22** (5), 444–448 (1992). [Kvantovaya Elektron. **19**, 486–491 (1992)].
- [16] **S. Nagai, H. Furuhashi, Y. Uchida, J. Yamada, A. Kono and T. Goto**, *Formation dynamics of excited atoms in an ArF laser using He and Ne buffer gases*, J. Appl. Phys. **77** (7), 2906–2911 (1995).
- [17] **M. Ohwa and M. Obara**, *Theoretical evaluation of the buffergas effects for a self-sustained discharge ArF laser*, J. Appl. Phys. **63** (5), 1306–1312 (1988).
- [18] **R.C. Sze and T.R. Loree**, *Experimental studies of a KrF and ArF discharge laser*, IEEE J. Quantum Electron. **14** (12), 944–950 (1978).
- [19] **D.C. Hoffman, R. Bruzese, A.J. Kearsley and C.E. Webb**, *Long pulse operation of discharge-excited XeCl\* lasers*, J. Phys. D: Appl. Phys. **14**, L157–L161 (1981).
- [20] **M.S. Pronko**, *Controlling output gain uniformity by spatial variation of the x-ray preionization in a large-aperture discharge-pumped KrF amplifier*, IEEE J. Quantum Electron. **30** (9), 2147–2156 (1994).
- [21] **J.W. Gerritsen**, *High-efficiency operation of an x-ray preionized avalanche discharge XeCl laser*, PhD thesis, University of Twente, Enschede, The Netherlands (1989).
- [22] **A.V. Demyanov, L. Feenstra, P.J.M. Peters, A.P. Napartovich and W.J. Witteman**, *Kinetic modelling of a discharge pumped ArF excimer laser*. Submitted to J. Phys. D: Appl. Phys.
- [23] **H. Akashi, Y. Sakai and H. Tagashira**, *Modelling of a micro-streamer initiation and development of ArF excimer laser discharges*, Aust. J. Phys. **50**, 655–669 (1997).
- [24] **M.J. Kushner**, *Microarcs as a termination mechanism of optical pulses in electric-discharge-excited KrF excimer lasers*, IEEE Tr. Plasma Sci. **19** (2), 387–399 (1991).

- [25] **R.M. Hofstra**, *On the optical performance of the long pulse XeCl\* excimer laser*, PhD thesis, University of Twente, Enschede, The Netherlands (1999).
- [26] **A.V. Demyanov**, Private communication.

## Chapter 7

# Long pulse operation

In order to obtain long laser pulses gas mixtures should contain only low concentrations of the active ingredients, especially of the halogen donor [1–8]. Typically, a ‘lean’ gas mixture for a long pulse XeCl laser contains only  $\sim 0.7$  mbar HCl and  $\sim 10$  mbar Xe in the buffer gas Ne at a total gas pressure of 5 bar [7, 9].

With the different experimental set-ups discussed in chapter 5 we could not obtain ArF lasing with a ‘lean’ gas mixture. However, a strongly reduced self-inductance of the peaking circuit turned out to be the crucial step; with the set-up described in chapter 6 laser pulse lengths of tens of ns proved possible.

In this chapter we present the results of a parametric study on the pulse length and the output energy of the long-pulse ArF laser. The results show that there is a clear trade-off between the laser gain and the discharge stability, and therefore between the output energy and the pulse length.

### 7.1 Experimental set-up

The general experimental set-up of the laser is equal to that of chapter 6, see figures 6.1, 6.2 and 6.3.

Throughout the experiments that are discussed in this chapter the resonator is formed by a high reflection mirror with a 6 m concave radius and a plane 90 % reflection outcoupler to obtain a high optical feedback. The laser mirrors are placed outside

the laser vessel, to prevent contact with the fluorine containing gas mixture. The brass laser cathode is of the uniform field type [10]. The grounded anode is flat and it is made of nickel plated aluminium. The discharge volume is approximately  $60 \times 0.7 \times 1.2 \text{ cm}^3$  ( $l \times w \times h$ ).

The standard gas mixture of the experiments consists of 1.0 mbar  $\text{F}_2$ , 19.1 mbar He and 50.0 mbar Ar. The buffer gas Ne is added to a total gas pressure of 5 bar, thus  $\text{F}_2 : \text{He} : \text{Ar} : \text{Ne} = 0.02 : 0.38 : 1.00 : 98.60$ . The He in the gas mixture is a consequence of the fluorine being supplied in the form of a mixture of 4.95 %  $\text{F}_2$  in He. Each gas mixture is freshly made before the experiment and it is thoroughly mixed by the flow of a liquid nitrogen gas-purifier (ca. 15  $\ell/\text{min}$ ) in approximately 20 min prior to the experiments. The gas mixture is constantly flowed through the laser vessel and through the purifier during the experiments.

The laser is operated in the ferrite switched resonant overshoot mode, using 18  $\text{cm}^2$  ferrite in the switch, see section 4.6. The PFN consists of 96 TDK ceramic capacitors of  $C_{\text{cap}} = 2.7 \text{ nF}$  each and 42 capacitors with  $C_{\text{cap}} = 4.0 \text{ nF}$ , resulting in a PFN capacitance of  $C_{\text{PFN}} = 427.2 \text{ nF}$ . To minimise the self-inductance of the PFN the capacitors are arranged in a hexagonal close-packed pattern between copper sheets. The distance between the ferrites and the lowest row of PFN capacitors is reduced to a few mm. The peaking capacitance  $C_{\text{P}}$  consists of ten MuRata DHS-460-Z-30 ceramic capacitors of 460 pF (at 0 V) each, mounted inside the laser vessel to minimise the self-inductance of the set-up in the first stages of the discharge, see figure 6.1.

The laser is operated at a PFN-voltage of 5.3 kV, which is slightly higher than the optimum value of twice the steady state voltage, in order to increase the pumping power. The charging voltage of the pre-pulse mini-marx is kept at  $V_{\text{PP}} = 20 \text{ kV}$  throughout the experiments. The X-ray source is operated at a mini-marx charging voltage of  $V_{\text{XP}} = 30 \text{ kV}$ .

The current and voltage signals are measured with resistive probes, see figure 6.3 and the discussion in section 6.1 on page 90. The optical signal is measured with an UV sensitive photodiode (FND 100Q) and a 193 nm filter, placed behind the high reflectivity mirror, which has a transmittance of approximately 0.5 %, see figure 5.8 on page 71.

Unless stated otherwise, the experimental conditions are kept the same throughout the experiments.

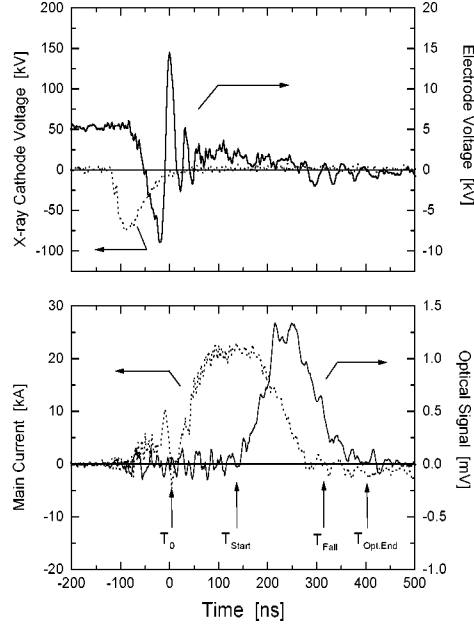


Figure 7.1: Typical wave forms of the laser pulse. Upper panel: X-ray source cathode voltage and calculated voltage  $V_{\text{calc}}$  (using  $L_{\text{vess}} = 8 \text{ nH}$ ). Lower panel: Main current  $I_{\text{main}}$  and laser intensity. The characteristic points used to describe the laser pulse are indicated (see text). Gas mixture: 5.0 bar,  $F_2 : \text{Ar} : \text{He} : \text{Ne} = 0.50 : 50.0 : 10.1 : \text{Rest}$  [mbar].

## 7.2 Experimental results and discussion

Figure 7.1 shows typical wave forms of the X-ray source cathode voltage, the ‘discharge voltage’, the discharge current and the laser intensity. The discharge voltage is calculated according to equation 6.1 [Sec. 6.1]:

$$V_{\text{calc}} = V_{\text{P}} - L_{\text{vess}} \frac{dI_{\text{main}}}{dt}. \quad (6.1)$$

with  $L_{\text{vess}} = 8 \text{ nH}$ . In figure 7.1 the discharge voltage is seen to show a steady state-like behaviour, which indicates that the discharge is very stable. This is also proven

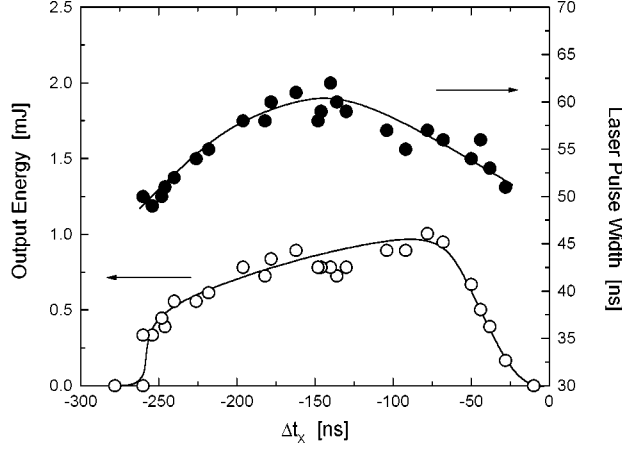


Figure 7.2: Laser pulse length (FWHM) and output energy versus the pre-ionisation delay time  $\Delta t_X$ . Gas mixture: 5.0 bar,  $F_2 : Ar : He : Ne = 1.0 : 50.0 : 19.1 : Rest$  [mbar].

by the fact that the laser pulse extends beyond the end of the current pulse.

In figure 7.1 the boundaries of several studied delay times, serving to characterise a number of properties of the pulses, are indicated with arrows: the optical start up time  $\Delta t_{\text{start}}$ , defined as the time delay between the discharge breakdown at  $t_0$  and the onset of the laser pulse at  $t_{\text{start}}$ ; the fall time  $\Delta t_{\text{fall}}$ , defined as the time between the the discharge start and the midpoint of the falling edge of the laser pulse at  $t_{\text{fall}}$ ; and the time delay  $\Delta t_{\text{opt.end}}$  to the end of the laser pulse at  $t_{\text{opt.end}}$ . The pre-ionisation delay time  $\Delta t_X$  is defined as the time delay between the onset of the X-ray pulse and the discharge breakdown, as is done in the discussions before [Ch. 5].

### 7.2.1 Dependency on the pre-ionisation timing

One of the most important parameters for obtaining a good discharge is the start of it, governed by the multiplication of the pre-ionisation electron density,  $N_e \approx 10^8 \text{ cm}^{-3}$ , to that of a fully developed discharge,  $N_e \approx 10^{15} \text{ cm}^{-3}$  [11], see also sections 2.2 and 5.3.1.

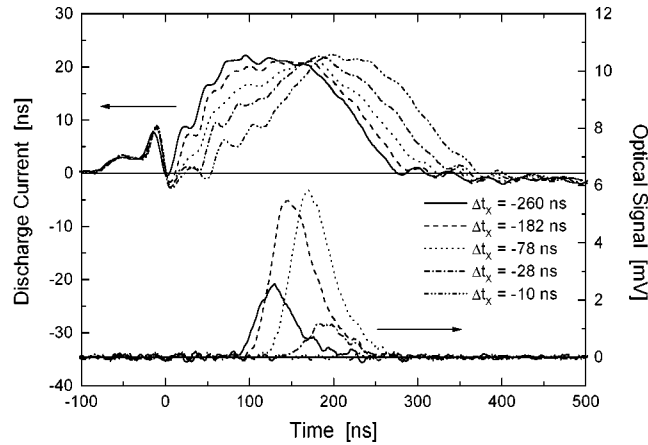


Figure 7.3: Typical current and photodiode signals with different pre-ionisation delay times. Gas mixture: 5.0 bar,  $F_2 : Ar : He : Ne = 1.0 : 50.0 : 19.1 : Rest$  [mbar].

An early pre-ionisation allows much time to the fluorine for attachment of the pre-ionisation electrons, causing small scale inhomogeneities in the electron density. Applying the pre-ionisation pulse late implies that there is very little time for the electron multiplication from the pre-ionisation electron density to the discharge level. In both cases an inhomogeneous discharge can occur, see chapter 5.

In figure 7.2 the laser pulse length (FWHM) and the optical output energy are shown as a function of the pre-ionisation delay time  $\Delta t_X$ . In the figure four different zones may be discerned in the optical performance with respect to the pre-ionisation delay time. In the first zone,  $\Delta t_X$  shorter than  $\sim 75$  ns, both the output power and the output energy increase with longer pre-ionisation delays. In the second zone,  $-75 \gtrsim \Delta t_X \gtrsim -150$  ns, the output energy decreases with longer delay times while the pulse length still increases. In the third zone,  $-150 \gtrsim \Delta t_X \gtrsim -260$  ns, the overall optical performance decreases with longer pre-ionisation delays. Finally, at pre-ionisation delay times longer than  $\Delta t_X \approx 260$  ns we found no lasing at all.

Typical wave forms of the current and the laser intensity at different pre-ionisation delay times are shown in figure 7.3. It is clear that the pre-ionisation timing has a strong influence on the laser performance. However, the effects are not as extreme as in

the previous experiments. This is probably the case because the fluorine concentration in the gas mixture is decreased by a factor of 7.5 in the present situation with respect to the conditions of chapter 5, so that the effects of the electron attachment to the  $F_2$  molecules on the total number of electrons are reduced. Furthermore, the gas mixture now consists mainly of neon instead of helium and the total gas pressure is increased from 4 bar to 5 bar. These changes increase the efficiency of X-ray pre-ionisation, so that the pre-ionisation electron density is expected to be much higher to start with than in the previous situation, see chapter 3 and refs. [12–14].

The optimum pulse length is found at a pre-ionisation delay time of  $\Delta t_X \approx -150$  ns, which means that the X-ray pulse reaches its maximum intensity before the onset of the pre-pulse. The optimum output energy, however, is found at a shorter pre-ionisation delay of  $\Delta t_X \approx -75$  ns, when the onsets of the X-ray pulse and of the pre-pulse coincide. In long pulse XeCl lasers, operated in the resonant overshoot mode, the optimum laser performance is also found when the X-ray pre-ionisation pulse is applied just ahead of the pre-pulse [6, 7]. In the case of the long pulse  $F_2$  laser the X-ray pre-ionisation is best applied during the start of the pre-pulse [8], which is closer to the results of chapter 5. This behaviour is probably caused by the increased amount of fluorine in the gas mixture in that case, as compared to the present ArF-laser configuration.

The results may be explained by considering the processes leading from the pre-ionisation to the discharge breakdown, see also section 5.3.1. At short pre-ionisation delays, the first zone in the above classification, there is too little time for a uniform multiplication of the pre-ionisation electron density. Thus the discharges start with a relatively low quality, resulting in a poor optical performance. The current signals in Fig. 7.3 reflect the difficult discharge start at very short pre-ionisation delay times. The growth of discharge instabilities and arcs can be seen from the sudden increase in the current, which denotes the collapse of the discharge impedance when small arcs are formed, partly short circuiting the discharge.

A longer pre-ionisation delay causes a better net electron density multiplication, and therefore a lower discharge impedance after the breakdown, which translates into a decreased current rise time, see Fig. 7.3. Thus, the discharge current in the early stages of the discharge is increased with longer pre-ionisation delays. This results in a better discharge quality, causing an earlier start up and a longer duration of the laser pulse.

The fact that the maximum output energy and the maximum pulse length are found at different values of  $\Delta t_X$  is probably caused by a difference in the electron density distribution in the discharge volume. The combination of the diffusion of pre-ionisation



electrons away from the centre of the pre-ionised region on one hand and the decreased electron attachment by  $F_2$  molecules at an increased electric field strength [15] on the other hand results in a wider discharge at long pre-ionisation delays [16]. This causes a lower current density, which in turn results in a lower specific pumping power and thus in a lower output energy, see also section 5.4.

However, at yet longer pre-ionisation delays, in the third zone, the electron density has had a chance to become inhomogeneous, yielding a worse discharge quality [Ch. 5]. Longer pre-ionisation delays also cause lower breakdown voltages, see figure 5.15 on page 78. This means that the peaking capacitors contain less energy at the breakdown of the discharge than at shorter pre-ionisation delays so that the initial discharge current is decreased, enhancing the decrease of the discharge quality.

At pre-ionisation delays longer than  $\sim 260$  ns, the gas mixture already breaks down on the pre-pulse, instead of being ignited by the overshoot. The resulting involuntary switch mode causes a reversal of the direction of the current during the first stages of the discharge, see section 4.7, which results in the appearance of hot spots on both electrodes [17,18]. The ensuing increased filamentation of the discharge inhibits lasing.

During the experiments the pre-ionisation is consistently applied approximately 20 ns before the onset of the pre-pulse, at  $\Delta t_X \approx 100$  ns.

## 7.2.2 Dependency on the gas composition

### $F_2$ concentration

The discharge stability of excimer lasers is strongly influenced by the concentration of the halogen donor in the gas mixture [1,8]. Therefore the sensitivity of the laser performance to the fluorine content is studied by varying the partial pressure of the fluorine in the gas mixture.

In figure 7.4 the pulse length (FWHM) and the output energy of the laser pulse are shown as a function of the fluorine partial pressure. The data points are the averages of series of shots with a fresh gas mixture. The error bars denote the standard deviation of the results of each series.

The average pulse length is seen to increase drastically with a decreasing fluorine pressure, from approximately 35 ns to 116 ns when the fluorine pressure is decreased from 2.0 mbar to 0.5 mbar  $F_2$ . The specific energy of the laser pulse is rather low

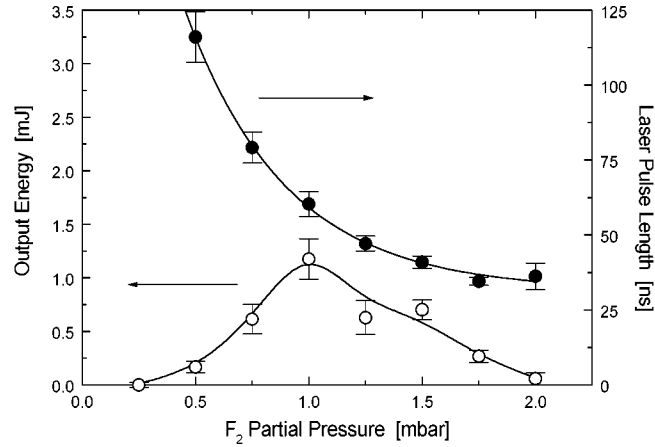


Figure 7.4: The laser pulse length (FWHM) and the output energy versus the  $F_2$  partial pressure. Gas mixture: 5.0 bar,  $F_2 : Ar : He : Ne = X : 50.0 : 20.2X : Rest$  [mbar].

at the longest pulses, 4 mJ/ℓ, which is probably caused by a low gain due to the low amount of fluorine, as well as the non-optimised construction of the main circuit of the laser. The optimum output energy of 25 mJ/ℓ is obtained with 1.0 mbar  $F_2$ , in a pulse of approximately 61 ns.

Figure 7.5 shows the discharge current and the laser intensity for a number of different fluorine pressures. In figure 7.6 the behaviour of the laser pulse is indicated in terms of the delay times  $\Delta t_{\text{start}}$ ,  $\Delta t_{\text{fall}}$  and  $\Delta t_{\text{opt.end}}$ . The curves in figure 7.6 are exponential fits to the data. It can be seen that the laser pulse occurs earlier in the discharge when the fluorine partial pressure is raised. The laser pulse length and amplitude decrease more rapidly than the start up time with an increasing  $F_2$  concentration.

We attribute the behaviour of the laser performance to a trade-off between the laser gain and the discharge stability. At higher fluorine partial pressures the formation of the  $ArF^*$  molecules is more efficient [11, 19–21], hence the lasers exhibits a higher gain. The result is a shorter start-up time of the optical pulse  $\Delta t_{\text{start}}$ , and more output energy.

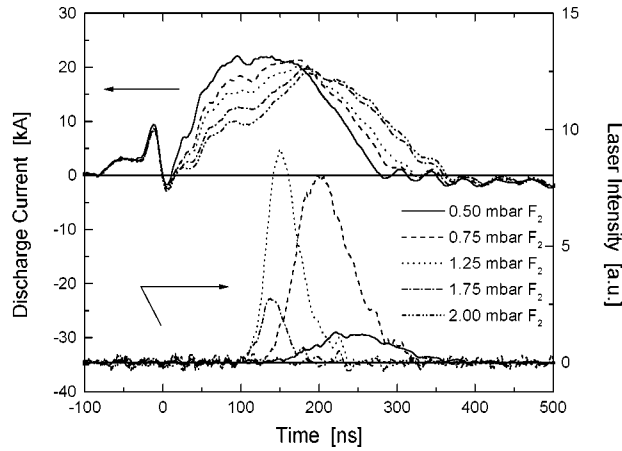


Figure 7.5: Typical current and photodiode signals with different  $F_2$  partial pressures. Gas mixture: 5.0 bar,  $F_2 : Ar : He : Ne = X : 50.0 : 19.1X : Rest$  [mbar].

However, at the same time, the higher  $F_2$  concentration leads to a worse discharge quality due to the fact that the inevitable discharge filamentation grows faster [2, 3]. This can be seen from the sudden current increase, which is caused by the impedance collapse of the discharge due to filamentation. The effect occurs increasingly early in the discharge as the fluorine concentration is raised, see figure 7.5. With a fluorine partial pressure of 1.75 mbar the discharge collapse coincides with the build-up of the laser pulse, which therefore is terminated almost immediately.

The starting quality of the discharge gets worse as well, because the effective pre-ionisation electron density is reduced by the increased electron attachment in the gas mixture by the present  $F_2$  molecules [3, 22]. This means that the voltage pre-pulse and overshoot have more difficulties generating an effective electron avalanche for a homogeneous breakdown, which results in a lower discharge homogeneity. The discharge also constitutes a higher impedance with an increasing halogen density so that the current pulse gets longer with an increasing  $F_2$  partial pressure, as is shown in figure 7.5.

The optical quality of the discharge is affected by the presence of filaments already before they bridge the discharge gap, because the radiation is scattered at the fila-

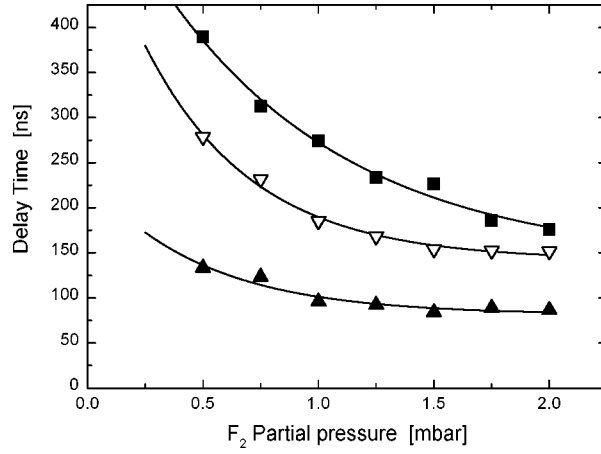


Figure 7.6: The delay time from the discharge start to the start of the optical signal  $\Delta t_{\text{start}}$  (▲), to the midpoint of the falling edge of the laser pulse intensity  $\Delta t_{\text{fall}}$  (▽) and to the end of the optical signal  $\Delta t_{\text{opt.end}}$  (■) versus the  $F_2$  partial pressure. Gas mixture: 5.0 bar,  $F_2 : Ar : He : Ne = X : 50.0 : 20.2X : \text{Rest}$  [mbar].

ments [22]. Other optical loss factors that increase with an higher  $F_2$  concentration are the absorption of the 193 nm radiation by  $F^-$  and  $F_2$  as well as the quenching of the  $ArF^*$  molecules by  $F_2$  molecules [19–21,23]. Nevertheless, we believe that the effects of these losses are outweighed by the growth of the discharge instabilities.

The stability of the discharge increases faster with a decreasing  $F_2$  concentration than the start-up time of the optical signal, see figure 7.6. Furthermore, we did not observe signs of a halogen burn-up at a fluorine pressure as low as 0.50 mbar, because the optical pulse extends beyond the pumping pulse, see figures 7.1 and 7.5. Thus, even longer  $ArF$  laser pulses can probably be generated, in which case the pumping power must be increased in order to overcome the lower laser gain because of the lower  $ArF^*$  formation efficiency.

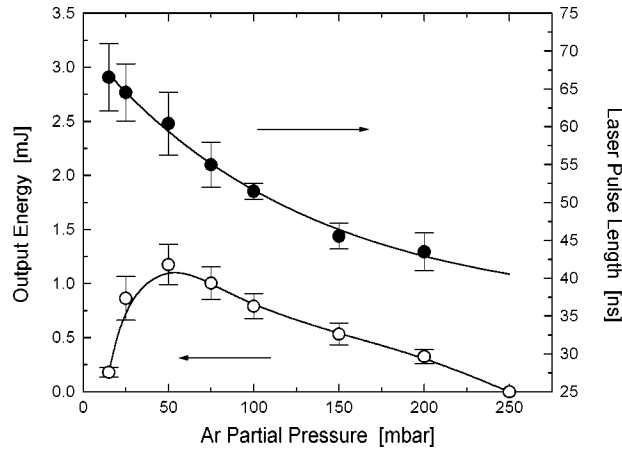


Figure 7.7: Laser pulse length (FWHM) and output energy versus Ar partial pressure. Gas mixture: 5.0 bar,  $F_2 : Ar : He : Ne = 1.0 : X : 19.1 : Rest$  [mbar].

### Ar concentration

The effect of a variation of the argon partial pressure on the performance of the laser was studied in the same manner as the fluorine dependency. The results are shown in figures 7.7, 7.8 and 7.9.

In these figures it may be seen that the laser pulse length decreases with an increasing Ar partial pressure, from 66 ns at 15 mbar Ar, to approximately 44 ns at 200 mbar Ar in the gas mixture. The optimum partial pressure for argon with respect to the output energy is found to be 50 mbar, with a pulse length of approximately 61 ns.

We find that the laser pulses occur earlier in the discharge with increasing argon pressure from 15 to 50 mbar, see figures 7.8 and 7.9. Between 50 and 100 mbar the pulses start at the same time in the discharge, but the intensity falls earlier. At argon pressures over 100 mbar the laser pulse intensity shows an overall decrease, while the pulse shape remains the same, see figure 7.8.

The behaviour indicates that the laser gain increases with augmenting Ar pressures, although loss mechanisms related to a higher Ar concentration eventually surpass

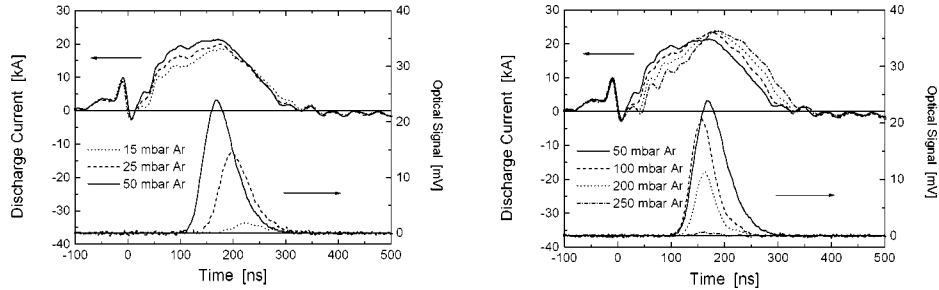


Figure 7.8: Typical current and photodiode signals with different Ar partial pressures, 15 – 50 mbar (left panel) and 50 – 250 mbar (right panel). Gas mixture: 5.0 bar,  $F_2 : Ar : He : Ne = 1.0 : X : 19.1 : Rest$  [mbar].

the gain increase. The increased gain is chiefly caused by a higher efficiency in the formation of the  $ArF^*$  molecule. The loss mechanisms, which are predominant at Ar partial pressures over  $\sim 100$  mbar, are caused by a number of processes: the absorption of the 193 nm radiation by  $Ar_2^*$  and  $Ar^{**}$ , and the quenching of  $ArF^*$  by Ar atoms [11, 19–21, 23]. The efficiency of these processes increases with a higher Ar concentration in the gas mixture. A higher Ar concentration also causes a higher electron density in the discharge [11], which in turn causes an increased quenching of the  $ArF^*$  molecules by electrons [11, 19–21].

The electrical qualities of the discharge are also affected by a variation in the Ar concentration in the gas mixture. Since Ar has a higher cross section for X-rays than the other components of the laser gas mixture [12, 13] the pre-ionisation becomes more effective with an increasing amount of Ar in the gas mixture [Sec. 3.3]. From the decreasing current rise time when the Ar pressure increases from 15 mbar to 50 mbar, see figure 7.8, we may see that the better pre-ionisation causes a faster breakdown, a better discharge quality and thus a better optical performance. However, increasing the amount of argon in the gas mixture causes the breakdown voltage of the gas mixture to rise, while the steady state voltage drops. This decreases the discharge stability. The higher difficulty in starting the discharge may be seen from the slower current rise in the signals in figure 7.8 at Ar pressures over 50 mbar. The increased

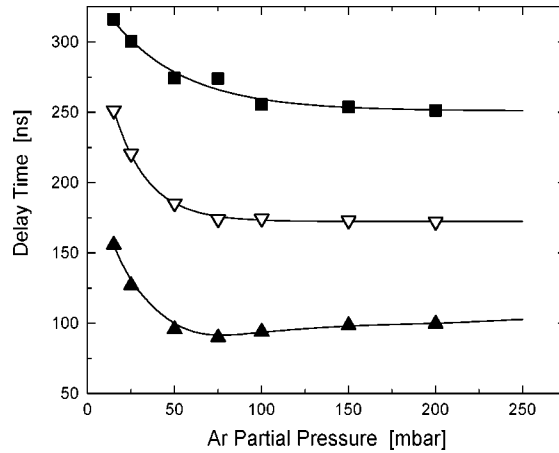


Figure 7.9: The delay time from the discharge start to the start of the optical signal  $\Delta t_{\text{start}}$  (▲), to the midpoint of the falling edge of the laser pulse intensity  $\Delta t_{\text{fall}}$  (▽) and to the end of the optical signal  $\Delta t_{\text{opt.end}}$  (■) versus the argon partial pressure. Gas mixture: 5.0 bar,  $F_2 : Ar : He : Ne = 1.0 : X : 19.1 : \text{Rest}$  [mbar].

instability can again be concluded from the sudden current increase during the discharge. The effect becomes clearer at higher Ar partial pressures. The growth of discharge instabilities at high Ar concentrations is probably further enhanced by the decrease in the mean electron energy, due to the lower steady state voltage at a higher Ar concentration. This favours the dissociative electron attachment of  $F_2$  [15,24], and thus the build-up of discharge instabilities.

### Total gas pressure

The performance of the laser as a function of the total gas pressure was studied by increasing the Ne pressure in a gas mixture containing 1.0 mbar  $F_2$ , 50.0 mbar Ar and 19.1 mbar He. Each gas mixture was freshly made. All other parameters were kept the same. The results are shown in figures 7.10, 7.11 and 7.12.

In figures 7.10 and 7.11 the length of the laser pulse can be seen to decrease steadily

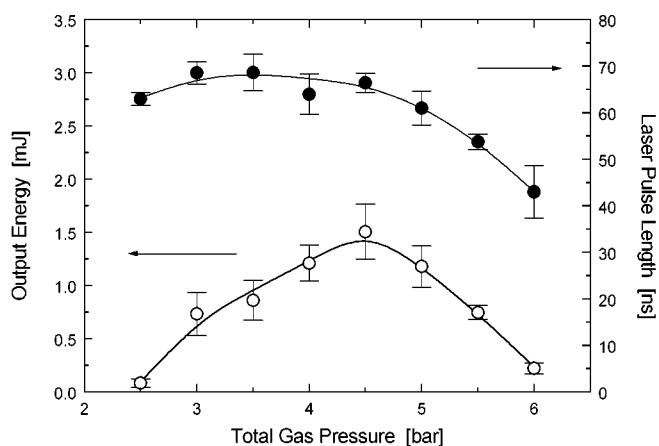


Figure 7.10: Laser pulse length (FWHM) and output energy versus Ar partial pressure. Gas mixture: 5.0 bar,  $F_2 : Ar : He : Ne = 1.0 : 50.0 : 19.1 : Rest$  [mbar].

when the pressure is increased over  $\sim 3.5$  bar, while the output energy clearly peaks at 4.5 bar. The laser pulse is found to start earlier in the discharge when the pressure goes up from 2.5 bar to 4.5 bar, see figure 7.12. When the pressure is raised over 4.5 bar the laser pulse starts increasingly late. The maximum laser intensity coincides with the current maximum [Fig. 7.11]. Both peaks shift to a later time in the discharge when the gas pressure rises. At gas pressures over 4.5 bar the laser intensity decreases uniformly.

This behaviour indicates an increasing gain in the laser up to a pressure of 4.5 bar, probably due to a higher efficiency in the formation of the  $ArF^*$  molecule as a result of three-body collisions [11, 19–21, 23, 25, 26] and an higher efficiency in the power deposition [27]. The intensity decrease at higher pressures may be caused by an increased quenching of the  $ArF^*$  molecules by Ne [11, 19–21, 23].

On the other hand, the electrical parameters of the discharge also change when the gas pressure is varied. Although the increased pressure causes a higher pre-ionisation density [12, 13], the breakdown voltage and the discharge impedance go up as well. This can clearly be seen in figure 7.11, which shows an increase of both the current rise time and the duration of the current pulse. The larger current rise time enhances



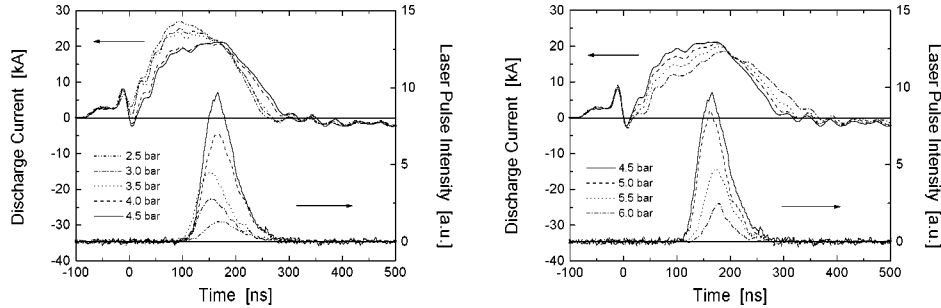


Figure 7.11: Typical current and photodiode signals with different total gas pressures, 2.5 – 4.5 bar (left panel) and 4.5 – 6 bar (right panel). Gas mixture:  $F_2 : Ar : He : Ne = 1.0 : 50.0 : 19.1 : Rest$  [mbar].

the growth of discharge instabilities, indicated by the increase in the current halfway during the pulse.

### He in the buffer gas

It is shown in chapter 6 that the use of Ne as the buffer gas yields longer laser pulses and higher output energies in a mixture containing 3.0 mbar  $F_2$  and 250 mbar Ar than when He is used.

To investigate this effect a little further the Ne buffer gas of the laser is replaced by a mixture of 1.0 bar He and 4.0 bar Ne, instead of pure Ne. When the laser is operated under the standard conditions it is found that the average pulse length at  $\Delta t_X = 125 \pm 10$  ns decreases from  $\sim 60$  ns to  $\sim 57$  ns and that the average output energy decreases from  $\sim 0.8$  mJ to  $\sim 0.6$  mJ.

Typical wave forms of a discharge with pure Ne as the buffer gas and those of a discharge with 1 bar He in the gas mixture are shown in figure 7.13. In figure 7.13 it may be seen that the breakdown voltage of the Ne-buffered gas mixture is slightly higher than that of the He:Ne-buffered gas mixture. The calculated steady state voltage of the Ne-buffered laser is a little lower than that of the gas mixture with the

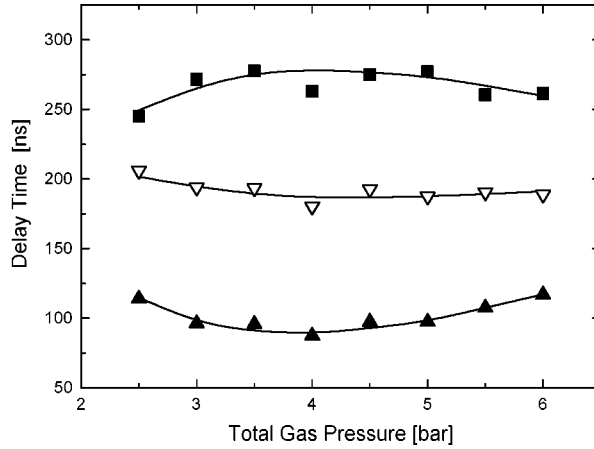


Figure 7.12: The delay time from the discharge start to the start of the optical signal  $\Delta t_{\text{start}}$  (▲), to the midpoint of the falling edge of the laser pulse intensity  $\Delta t_{\text{fall}}$  (▽) and to the end of the optical signal  $\Delta t_{\text{opt.end}}$  (■) versus the total gas pressure. Gas mixture:  $F_2 : Ar : He : Ne = 1.0 : 50.0 : 19.1 : \text{Rest}$  [mbar].

He:Ne buffer gas mixture. The main current in the Ne-buffered case remains higher than that of the He:Ne-buffered gas mixture for almost 200 ns. The calculated input powers into the discharges are equivalent.

Although the laser pulses start at the same time in the discharge, the laser intensity is seen to increase faster and to become higher in the case of the Ne-buffered gas mixture. The intensity of both laser pulses falls after approximately the same time in the discharge, probably caused by the growth of discharge filaments due to the amount of fluorine in the gas mixtures (see above).

The faster rise of the laser intensity in the case of the Ne buffer gas may be due to the fact that in Ne-buffered gas mixtures the spontaneous emission is found to start earlier in the discharge because the formation of the  $ArF^*$  excimer is more efficient in these discharges than in the case of He-buffering [19,28]. However, it is found that the gain of Ne-buffered gas mixtures is lower than for He-buffered gas mixtures [19]. This means that the optimum optical feedback for Ne-buffered gas mixtures is higher than when He is used for the buffer gas. The very high optical feedback of approximately

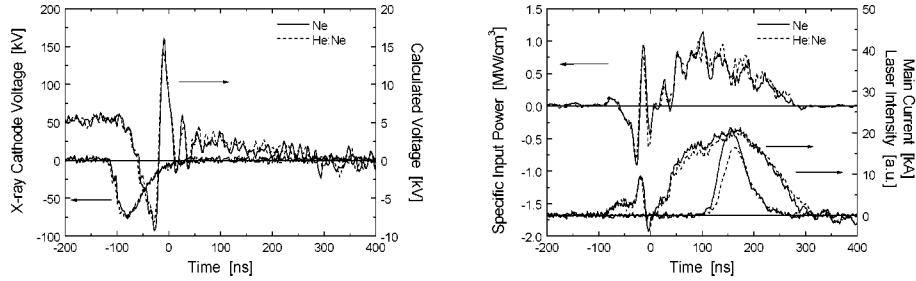


Figure 7.13: Comparison of the typical wave forms of gas discharges with pure Ne and a mixture of He and Ne for the buffer gas. Left panel: X-ray cathode voltage and calculated voltage  $V_{\text{calc}}$ . Right panel: Main current  $I_{\text{main}}$ , laser intensity and calculated input power into the discharge  $P_{\text{calc}}$ . Gas mixture: 5.0 bar,  $F_2 : \text{Ar} : \text{Buffer gas} = 1.0 : 50.0 : \text{Rest}$  [mbar]. Buffer gas: pure Ne (Drawn line) or He : Ne = 1.0 : 4.0 [bar] (Dashed line).

87 % of our set-up may have exploited this effect, causing the higher output power for Ne-buffered gas mixtures.

### 7.2.3 Dependency on the pumping power

The dependency of the laser performance on the pumping power is studied by varying the charging voltage of the pulse forming network  $V_{\text{PFN}}$ , while using the standard gas mixture and keeping all other parameters constant.

Figures 7.14 and 7.15 show that the pulse length increases from approximately 55 ns to 80 ns FWHM when the energy on the PFN is varied from 3.7 J to 13.2 J, which corresponds to PFN-voltages from 4.1 kV to 7.9 kV. The growth rate of the pulse length decreases somewhat with higher voltages. The output energy increase, from 0.2 mJ (4 mJ/ℓ) to 3.0 mJ (60 mJ/ℓ), shows the same behaviour, although the growth rate decreases more strongly. In figures 7.15 and 7.16 the optical pulse can be seen to start earlier in the discharge when the energy stored on the PFN is increased. The maximum laser intensity coincides with the current maximum, which occurs

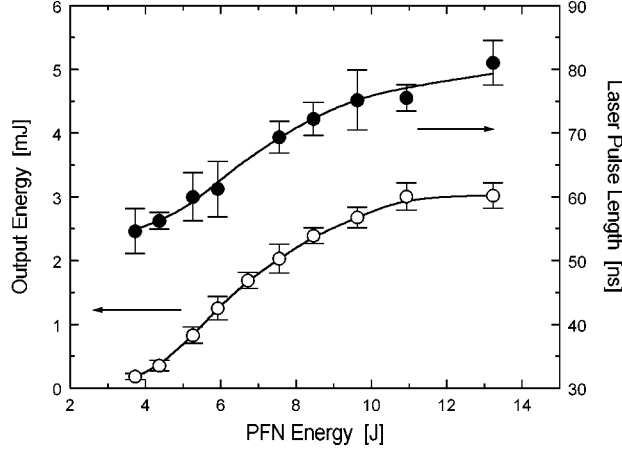


Figure 7.14: Laser pulse length (FWHM) and output energy versus the energy stored on the PFN. Gas mixture: 5.0 bar,  $F_2$ :Ar:He:Ne = 1.0:50.0:19.1:Rest [mbar].

increasingly early in the discharge when the PFN voltage is raised.

At a PFN voltage of  $V_{\text{PFN}} \gtrsim 8$  kV ( $E_{\text{PFN}} \gtrsim 13.7$  J) the laser breaks down spontaneously during the charging of the PFN, before the pre-ionisation and the pre-pulse have been applied. Under these conditions there is no homogeneous discharge and therefore no lasing.

The behaviour indicates that the laser gain increases when a higher pumping power is applied. The increase of the laser performance with an increasing PFN voltage wears off at higher PFN voltages. This may be caused by a stronger electron quenching of the  $\text{ArF}^*$  molecules due to an increased electron density at higher voltages [11,19–21].

Theory predicts that the discharge collapses faster at an increased current density in the discharge due to a faster halogen depletion [2,3]. This has indeed been observed in other fluorine-containing lasers [3,8].

In spite of the fact that we find an increase in the discharge current which we attribute to the formation of arcs in the discharge, in our set-up the discharge is not found to collapse increasingly early with a higher discharge current. Furthermore, in figures 7.15 and 7.16 we may see that the optical signal does not deteriorate when

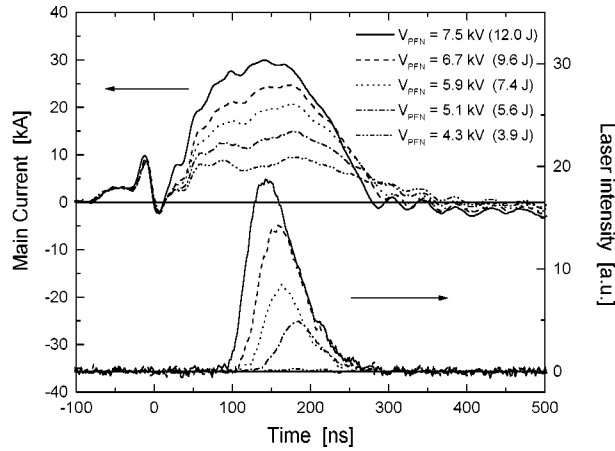


Figure 7.15: Typical current and photodiode signals with different PFN voltage  $V_{\text{PFN}} = 4.3 - 7.5$  kV. Gas mixture: 5.0 bar,  $F_2 : \text{Ar} : \text{He} : \text{Ne} = 1.0 : 50.0 : 19.1 : \text{Rest}$  [mbar].

the current is increased, although the increase in the pulse length is reduced at higher charging voltages.

The effects of an increase in the halogen depletion are probably attenuated by the fact that the cathode in our set-up is shaped in an Ernst-profile [10], see figure 6.1, which allows the discharge to become wider when higher voltages are used. Thus, the current density decreases while the total discharge current increases. The reduced current density leads to a lower specific pumping power and thus to a lower output energy. This accounts for the effect that the growth rate of the output energy decreases faster than that of the pulse length with increasing PFN voltage.

### 7.3 Conclusions

We have shown that laser pulses with a length of up to 120 ns may be obtained from a discharge pumped ArF excimer laser, operated under nearly voltage matched conditions. The discharges are very stable, due to the use of on the one hand a gas

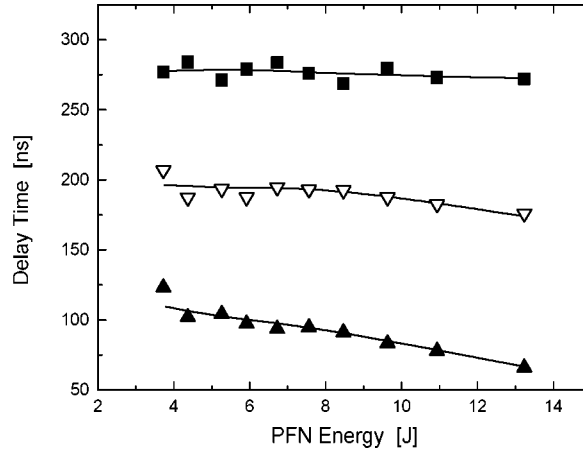


Figure 7.16: The delay time from the discharge start to the start of the optical signal  $\Delta t_{\text{start}}$  (▲), to the midpoint of the falling edge of the laser pulse intensity  $\Delta t_{\text{fall}}$  (▽) and to the end of the optical signal  $\Delta t_{\text{opt.end}}$  (■) versus the energy stored on the PFN. Gas mixture: 5.0 bar,  $F_2 : Ar : He : Ne = 1.0 : 50.0 : 19.1 : \text{Rest}$  [mbar].

mixture with very low amounts of  $F_2$  and Ar and on the other hand an experimental set-up with a uniform field electrode and a very short current rise time during the formation of the discharge.

The laser pulse length is shown to be determined in the first place by discharge instabilities, which grow into filaments and arcs. The growth of instabilities depends primarily on the fluorine concentration of the gas mixture. Decreasing the partial pressures of  $F_2$  and Ar increases the pulse length without an apparent maximum, until of course the concentrations become too low to sustain lasing. However, there is a maximum pulse length found when the total gas pressure is varied from 2 to 6 bar

Since a decreased concentration of the active ingredients also causes a lower laser gain, the optimum pulse length and the optimum pulse energy are found with different gas mixtures. The optimum output energy at voltage matched conditions is 30 mJ/ℓ at a pulse length of approximately 67 ns, found when using a gas mixture consisting of 1.0 mbar  $F_2$  50.0 mbar Ar, 19.1 mbar He in the buffer gas Ne at 4.5 bar total pressure. The optimum pulse length of  $116 \pm 8$  ns is obtained with a gas mixture consisting of

0.50 mbar F<sub>2</sub>, 50.0 mbar Ar, 9.6 mbar He in the buffer gas Ne at 5 bar total pressure. Both the optical pulse length and the output energy are found to increase with an increasing pumping power.

## References

- [1] **R.S. Taylor and K.E. Leopold**, *Microsecond duration optical pulses from a UV-preionized XeCl laser*, Appl. Phys. Lett. **47** (2), 81–83 (1985).
- [2] **J. Coutts and C.E. Webb**, *Stability of transverse self-sustained discharge-excited long-pulse XeCl lasers*, J. Appl. Phys. **59** (3), 704–710 (1986).
- [3] **R.S. Taylor**, *Preionization and discharge stability study of long optical pulse duration UV-preionized XeCl lasers*, Appl. Phys. B **41**, 1–24 (1986).
- [4] **R.S. Taylor and K.E. Leopold**, *Ultralong optical-pulse corona preionized XeCl laser*, J. Appl. Phys. **65** (1), 22–29 (1989).
- [5] **J.-M. Hueber, B.L. Fontaine, N. Bernard, B.M. Forestier, M.L. Sentis and Ph.C. Delaporte**, *Long pulse KrCl excimer laser at 222 nm*, Appl. Phys. Lett. **61** (19), 2269–2271 (1992).
- [6] **R.S. Taylor and K.E. Leopold**, *Magnetic-spiker excitation of gas-discharge lasers*, Appl. Phys. B **59**, 479–508 (1994).
- [7] **J.C.M. Timmermans**, *Double discharge XeCl-laser*, PhD thesis, University of Twente, Enschede, The Netherlands (1995).
- [8] **H.M.J. Bastiaens, S.J.M. Peeters, X. Renard, P.J.M. Peters and W.J. Witteman**, *Long pulse operation of an X-ray preionized molecular fluorine laser excited by a prepulse-main pulse system with a magnetic switch*, Appl. Phys. Lett. **72** (22), 2791–2793 (1998).
- [9] **R.M. Hofstra**, *On the optical performance of the long pulse XeCl\* excimer laser*, PhD thesis, University of Twente, Enschede, The Netherlands (1999).
- [10] **G.J. Ernst**, *Uniform-field electrodes with minimum width*, Opt. Comm. **49** (4), 275–277 (1984).
- [11] **S. Nagai, H. Furuhashi, A. Kono, Y. Uchida and T. Goto**, *Measurement of temporal behaviour of electron density in a discharge-pumped ArF excimer laser*, IEEE J. Quantum Electron. **34** (8), 942–948 (1998).
- [12] **K. Midorikawa, M. Obara and T. Fujioka**, *X-ray preionization of rare-gas-halide lasers*, IEEE J. Quantum Electron. **20** (3), 198–205 (1984).
- [13] **J.W. Gerritsen**, *High-efficiency operation of an x-ray preionized avalanche discharge XeCl laser*, PhD thesis, University of Twente, Enschede, The Netherlands (1989).

- [14] **M. Trentelman**, *Gas discharge excited XeF laser*, PhD thesis, University of Twente, Enschede, The Netherlands (1993).
- [15] **P.J. Chantry**, *Negative ion formation in gas lasers*, In: Applied Atomic Collision Physics, E.W. McDaniel and W.L. Nighan, eds., volume 3, Gas Lasers, 35–70, Academic Press, New York, NY, (1982).
- [16] **F.A. van Goor, J.C.M. Timmermans and W.J. Witteman**, *The influence of charge-mode operation of a XeCl laser on the beam profile*, Opt. Comm. **124**, 56–62 (1996).
- [17] **M. Makarov and Yu. Bychkov**, *The dynamics of XeCl discharge contraction*, J. Phys. D: Appl. Phys. **29**, 350–363 (1996).
- [18] **T. Müller**, *Zeitliche Entwicklung und Filamentierung von KrF<sup>\*</sup>-Lasergasentladungen*, PhD thesis, Technische Hochschule Darmstadt, Darmstadt, Germany (1992). (In German).
- [19] **M. Ohwa and M. Obara**, *Theoretical evaluation of the buffergas effects for a self-sustained discharge ArF laser*, J. Appl. Phys. **63** (5), 1306–1312 (1988).
- [20] **A.M. Boichenko, V.I. Derzhiev, A.G. Zhidkov and S.I. Yakovlenko**, *Kinetic model of an ArF laser*, Sov. J. Quantum Electron. **22** (5), 444–448 (1992). [Kvantovaya Elektron. **19**, 486–491 (1992)].
- [21] **D. Lo, A.I. Shchedrin and A.V. Ryabtsev**, *The upper energy limit of a self-sustained discharge-pumped ArF laser*, J. Phys. D: Appl. Phys. **29**, 43–49 (1996).
- [22] **M.J. Kushner**, *Microarcs as a termination mechanism of optical pulses in electric-discharge-excited KrF excimer lasers*, IEEE Tr. Plasma Sci. **19** (2), 387–399 (1991).
- [23] **A.V. Demyanov, L. Feenstra, P.J.M. Peters, A.P. Napartovich and W.J. Witteman**, *Kinetic modelling of a discharge pumped ArF excimer laser*. Submitted to J. Phys. D: Appl. Phys.
- [24] **S. Nagai, M. Sakai, H. Furuhashi, A. Kono, T. Goto and Y. Uchida**, *Effects of F<sup>-</sup> ions and F<sub>2</sub> molecules on the oscillation process of a discharge-pumped ArF excimer laser*, IEEE J. Quantum Electron. **34** (1), 40–46 (1998).
- [25] **H. Akashi, Y. Sakai and H. Tagashira**, *Modelling of a self-sustained discharge-excited ArF excimer laser*, J. Phys. D: Appl. Phys. **27**, 1097–1106 (1994).
- [26] **M. Maeda, T. Nishitarumizu and Y. Miyazoe**, *Formation and quenching of excimers in low-pressure rare-gas/halogen mixtures by e-beam excitation*, Jpn. J. Appl. Phys. **18** (3), 439–445 (1979).
- [27] **A. Garscadden, M.J. Kushner and J.G. Eden**, *Plasma physics issues in gas discharge laser development*, IEEE Tr. Plasma Sci. **19** (6), 1013–1031 (1991).
- [28] **S. Nagai, H. Furuhashi, Y. Uchida, J. Yamada, A. Kono and T. Goto**, *Formation dynamics of excited atoms in an ArF laser using He and Ne buffer gases*, J. Appl. Phys. **77** (7), 2906–2911 (1995).



## Chapter 8

# Design considerations for future devices

From the experiments, reported in this thesis, several conclusions may be drawn that may serve as advice in the design of new, optimised laser devices. This chapter is divided into two; one part is devoted to the design parameters that need some extra attention, the other part focuses on topics which should be studied better to grasp the properties of the laser and the discharge at a more fundamental level.

### 8.1 Design parameters

- The discharge region must have a homogeneous electrical field density.
- The self-inductance of the entire system should be as low as possible.
- The self-inductance of the laser head, containing the peaking capacitors, should get even more attention.
- The pre-ionisation pulse should have a rise time as short as possible.
- The pre-ionisation must be homogeneous and yield an electron density of at least  $10^9 \text{ cm}^{-3}$

- In the case of X-ray pre-ionisation, the X-ray window should either be much larger than the intended discharge area, in which case the electrode shape should dictate the discharge dimensions, or it should be much smaller than the electrodes, in which case the discharge volume is determined by the boundaries of the pre-ionisation electron distribution. An overlap of the two boundaries must be prevented: in that case the discharge gets unstable earlier in the discharge because the two (inherent) causes of inhomogeneities add up.
- The spiker-pulse should have a rise time of approximately 20 ns, the pre-pulse-rise time may be somewhat longer.
- The pre-pulse should be higher than the steady-state voltage in order to have it contribute to the electron multiplication.
- The timing of the pre-ionisation and the pre-pulse should be variable, and accurately adjustable.
- The shot-to-shot reproducibility of the system should be as high as possible.
- The peaking capacitance should be as evenly spread-out along the discharge or the electrodes as possible, to minimise plasma density fluctuations due to small variations in the inductance between the peaking capacitors and the discharge along the electrodes.
- The peaking capacitors should be readily accessible and replaceable in order to enable the optimisation of the set-up.
- The laser yields more output power at higher pumping powers. A possible way to increase the pumping power is to increase the PFN-capacitance. However, the PFN charging time must be short, to prevent premature breakdown.
- The main voltage probes should be connected across the electrodes, or at least in a position where a reliable correction for the remaining self-inductance can be performed.
- A current probe should be incorporated in such a manner that it measures the actual discharge current.
- The laser should be equipped with some form of gas purification.
- The mirrors should be inside the gas mixture in order to eliminate windows and other loss-mechanisms as much as possible.

- In order to be able to change the laser mirrors quickly without having to clean, purge and re-passify the laser chamber the mirror-holders should be equipped with valves to the laser vessel.
- The mirrors should be alignable from the outside and they should be insensitive to pressure variations of the laser.

## 8.2 Further study

The influence of the following properties on the discharge quality should be studied in greater detail.

- The rise time of the PFN-voltage.
- The self-inductance of the main circuit.
- The self-inductance of the peaking circuit.
- The pre-ionisation pulse length and rise time.
- The pre-ionisation timing dependency of the laser operating in the resonant overshoot mode.
- The composition of the buffer gas with respect to the pulse length and the output energy of the laser.
- The scattering of the laser beam on discharge filaments.
- The variation of the discharge width during the discharge pulse.



## Appendix A

# The mini-marx generator

The operation of a marx generator is based on charging a number of capacitors in parallel, and discharging them while they are connected in series. The resulting voltage is the voltage per stage, multiplied by the number of stages in the generator.

The mini-marx generator, used in our set-up for the operation of the X-ray source as well as for the delivery of the pre-pulse, consists of six equal stages of  $C_s = 3.6$  nF per stage. The capacitors are charged continuously via charging resistors of  $R_{ch} = 100$  k $\Omega$ . The equivalent circuit of the mini-marx is shown in figure A.1. The switches between the stages are spark gaps, made of stainless steel balls. The first spark gap is triggered by means of a tungsten spark pin inside the sphere, see figure A.1.

Once the first spark gap is triggered, the voltage across the first capacitor reverses from its initially charged voltage  $V_{ch}$  to  $-V_{ch}$ . Therefore the voltage difference across the second spark gap suddenly increases from  $V_{ch}$  to  $2V_{ch}$ , which causes it to break down as well. The voltage on the next capacitor then drops from  $+V$  to  $-2V$ , triggering the third spark gap. This process is repeated until the last spark gap is triggered and a high voltage pulse of  $6V_{ch}$  is generated with a very short rise time. The voltage rise of the pulse at the exit of the mini-marx is less than 2 ns. We have not succeeded in measuring accurately the actual rise time of the device [1]. The rise time of the voltage in our set-up is therefore mainly determined by the circuit to which the mini-marx is connected.

The body of the mini-marx generator is mounted inside a perspex cylinder, inside a copper cylinder, resulting in a coaxial geometry. The capacitors are mounted on one

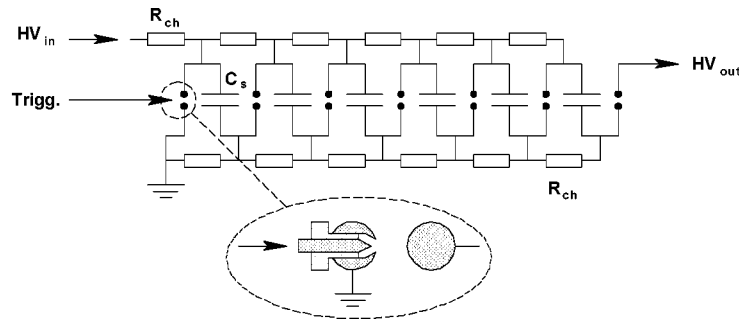


Figure A.1: The equivalent circuit of the mini-marx generator, used for the generation of the pre-pulse and for the operation of the X-ray source. All capacitors are  $C_s = 3.6 \text{ nF}$ , the charging resistors are  $R_{ch} = 100 \text{ k}\Omega$ . The construction of the first, triggerable, spark gap is shown enlarged.

side of a PVC base-plate, the spark gaps are mounted on the other side. Between the spark gap electrodes two grooves are machined in the base plate, to increase the creeping distance between the gaps. The interelectrode distance of the spark gaps can be adjusted.

The spark gaps are mounted transverse to the axis of the mini-marx, in order to pre-ionise the next gap by the UV radiation of the spark. Thus the cascade-triggering of the generator gaps is very fast. The entire mini-marx generator can be pressurised up to 3 bar with nitrogen. The nitrogen is continuously flowed along the gaps, to blow away possible debris from the electrodes or from the PVC-base-plate.

The trigger pulse is delivered to the mini-marx in several stages: a 5 V TTL pulse, generated by a commercially available pulse generator, triggers a home-built solid state pulser, which delivers a 400 V pulse to trigger a small thyatron circuit. The capacitor of the thyatron circuit is charged to +7 kV in the case of the X-ray source. For the pre-pulse a “floating” thyatron is used, charged to -15 kV. The thyatrons deliver high voltage pulses to the trigger pins inside the mini-marx generators. These trigger pulses have the opposite polarity to charging polarity of the thyatron capacitors.

The mini-marx generators are usually charged to  $V_{XP} = -30 \text{ kV}$  and  $V_{PP} = 25 \text{ kV}$ , respectively. The interelectrode distance of the spark gaps and the pressure and flow

rate of the nitrogen in each mini-marx are adjusted slightly higher than the critical values for self-breakdown. This decreases the time jitter of the mini-marxes, although it causes self-breakdown to occur occasionally, since the generators are charged continuously.

The time jitter of the mini-marx itself is defined as the variation in the time delay between the moment the trigger pulse is applied to the first spark gap of the mini-marx and the onset of the output voltage pulse. The jitter of the mini-marx depends on the polarity of the charging and that of the trigger pulse. The X-ray source mini-marx, charged negatively and triggered with a positive pulse, can have a time jitter as low as approximately 5 ns, although the mean jitter is  $\sim 12$  ns. The mini-marx that is used for the pre-pulse is positively charged and it is triggered by a negative trigger pulse. Its time jitter is up to 50 ns.

When the two mini-marx generators were exchanged, the difference between the amount of jittering proved to be a consequence of the used charging polarities, not of the generators themselves.

Since the two jitters add up, the time jitter between both mini-marx pulses was generally  $\sim 50$  ns.

## References

- [1] **J. Couperus**, *Onderzoek naar het effect van de sustainer van een door een elektronenbundel onderhouden gasontlading op de output van een Ar:Xe laser*, Master's thesis, University of Twente (1990). (In Dutch).





## Appendix B

# A kinetic model of a discharge pumped ArF excimer laser

The kinetic model used to describe the operation of the laser is developed by A.V. Demyanov and co-workers of the Troitsk Institute for Innovative and Thermonuclear Research (TRINITI), Troitsk, Moscow Province, Russia, under the guidance of prof. dr A.P. Napartovich, in cooperation with the Quantum Electronics Group of the University of Twente, Enschede, the Netherlands.

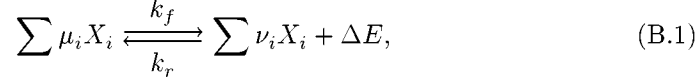
The one-dimensional model basically consists of two parts:

- The ‘master’ equation, which incorporates the population densities of all particles considered in the discharge.
- The set of equations describing the electrical circuit.

The description of the model in this appendix is based on more elaborate reports by Demyanov [1] and Fischer [2]. In this description we attempt to give a very concise overview of some aspects of the model. In the first section we derive the ‘master’ equation which describes the rate of change of the particle densities of the various considered species. Next the solving of the Boltzmann equation for the electron energy distribution is discussed. In the third part the parallel resistor model is introduced. In the last section the rate equations incorporated in the model are stated.

## B.1 Kinetic model

Reactions in an excimer laser discharge involving the species  $X_1, \dots, X_n$  may generally be written in the form of



where  $k_f$  and  $k_r$  are the forward and reverse rate constants (in  $\text{s}^{-1}$ ,  $\text{cm}^3/\text{s}$ ,  $\text{cm}^6/\text{s}$ , etc.) and  $\mu_i$  and  $\nu_i$  are nonnegative integer coefficients.

The energy balance of the reactions of equation B.1 is given by

$$\sum \mu_i E_i \rightleftharpoons \sum \nu_i E_i + \Delta E, \quad (\text{B.2})$$

with  $E_i$  the total energy of the species  $i$  with respect to the decomposition of the species into neutral atoms.  $\Delta E$  is the energy defect of the reverse reaction of equation B.1.

The net rate  $R$  for the reaction of equation B.1 is given by

$$R = R_f - R_r \quad (\text{B.3})$$

where  $R_f = k_f \prod_i [X_i]^{\mu_i}$  and  $R_r = k_r \prod_i [X_i]^{\nu_i}$  with  $[X_i]$  being the population density (in  $\text{cm}^{-3}$ ) of the species  $X_i$ . Thus, the contribution of the reaction B.1 to the production or loss of a species  $X_i$  is

$$\frac{d}{dt} [X_i] = (\nu_i - \mu_i) R. \quad (\text{B.4})$$

For an arbitrary reaction scheme, which contains several different collision processes, labeled by  $k$ , the full ‘master’ equation for the system becomes:

$$\frac{d}{dt} [X_i] = \sum_k (\nu_{i_k} - \mu_{i_k}) R_k, \quad \text{for } i = 1, \dots, n. \quad (\text{B.5})$$

The corresponding energy conservation equation is:

$$\frac{d}{dt} \sum_i E_i [X_i] = - \sum_k \Delta E_k, \quad \text{for } i = 1, \dots, n. \quad (\text{B.6})$$

with  $\Delta E_k = \sum_k (\nu_{i_k} - \mu_{i_k}) E_i$  being the net energy change of the system due to reaction  $k$ .

Since during the calculation of a discharge the discharge parameters, and thus the rate constants, may vary over several orders of magnitude, the master equations B.5 and B.6 often become a rigid set of differential equations. During the simulation equations B.5 and B.6 are calculated using a multi-step technique, which automatically adjusts the integration step size during the calculation, so that the required accuracy conditions are maintained.

The model is developed with a maximum flexibility in mind. The program consists of several separate subroutines that check for the generation of new species and then implements them in the main executive program to allow for a single, self-contained coupled analysis, based on the specified reaction scheme. At various points in the program checks are performed against zero-results.

The kinetic computer model can be used both for the simulation of a discharge pumped system and for an e-beam pumped system, since the equations for both cases are programmed in subroutines that can be switched on or off.

## B.2 Solving the Boltzmann equation

For the master equations B.5 and B.6 to be accurate, the energies of all considered particles must be known. Since the energy is pumped into the gas by means of an electrical discharge the most important part is the electron energy distribution function  $f(\vec{r}, \vec{v}, t)$ , which can be calculated from the Boltzmann equation.

In its basic form the Boltzmann equation is given by:

$$\left( \frac{\partial}{\partial t} + \vec{v} \cdot \nabla_{\vec{r}} + \frac{\vec{F}}{m} \cdot \nabla_{\vec{v}} \right) f(\vec{r}, \vec{v}, t) = \left( \frac{\delta f}{\delta t} \right)_{\text{coll}} \quad (\text{B.7})$$

where  $\vec{r}, \vec{v}$  are the place and velocity vectors,  $\vec{F}$  is the force term and  $m$  is the electron mass. The right hand side of the equation is the collision term; the change in the distribution function by collisions between electrons and other gas components.

The usual approach for solving the Boltzmann equation is by expanding the electron energy distribution function into Legendre polynomials. Taking only the first two

terms into account a rather good approximation is already obtained:

$$f(\vec{v}) = f_0(v) + \frac{\vec{v}}{|v|} \vec{f}_1(v), \quad |\vec{f}_1| \ll |f_0| \quad (\text{B.8})$$

The functions  $f_0$  and  $\vec{f}_1$  then only depend on the electron velocity.  $f_0$  is the normalised distribution function of an initial guess. The vectorial aspect of  $\vec{f}_1$  is determined by  $\vec{F} = -e\vec{E}$ . The distribution function  $f(\vec{v})$  is normalised in velocity space:

$$\int_{-\infty}^{\infty} f(\vec{v}) d^3v = 1 \quad (\text{B.9})$$

When neglecting spatial gradients in the discharge ( $\vec{v} \nabla_{\vec{r}} f := 0$ ) and start-up effects ( $\frac{\partial f}{\partial t}(t_0) := 0$ ) equation B.7 may be split into separate scalar and a vectorial equations.

The above approximation is called the two-term quasi-steady Boltzmann equation. The two-term approximation is correct when the drift velocity of the electrons is much smaller than the random thermal velocity.

In the model the two-term Boltzmann equation is written in the form of contributions of several processes:

- The net creation or loss of electrons on the time scale of interest (the interpolation interval).
- The electron flux in energy space, driven by the applied electric field.
- Elastic scattering collisions.
- Electron-electron collisions.
- Inelastic collisions.
- External sources of electrons.

From the solution of the Boltzmann equation in energy space  $f_0(u)$  all forward and reverse electron excitation rates, electrical power partitioning as well as plasma parameters such as drift velocity, mobility, average and characteristic energies, effective temperature etc.) may be obtained. Furthermore, the energy-integral of the Boltzmann equation yields an expression for the conservation of the electron number density

$$\frac{dn_e}{dt} = n_e(\alpha_2 - \beta) - \gamma n_e^2 \quad (\text{B.10})$$

with  $\alpha_2$  being the total secondary ionisation,  $\beta$  is the electron attachment frequency and  $\gamma$  is the rate constant for ionic recombination.

The Boltzmann equation is solved numerically by using the so-called integro-interpolation method. This method is an iterative technique which starts with an initial guess  $f^0$  and subsequently generates a series of increasingly accurate approximations  $f^S$ . An acceptable approximation to the Boltzmann equation is assumed to have been attained when a predefined convergence criterion between  $f^S$  and  $f^{S+1}$  is satisfied.

The electron density equation  $dn_e/dt$  [Eq. B.10] is a parameter in the process. Since the actual value of  $dn_e/dt$  is known only after the Boltzmann equation has been solved, a self-consistent iterative method is used, starting with an initial estimate. Using this estimate the Boltzmann equation is solved recursively until the convergence criterion is met. The result is then used to obtain a better approximation of  $\alpha_2$ ,  $\beta$  and  $\gamma$  to use in equation B.10, which then yields a more accurate result for  $dn_e/dt$ . The result of equation B.10 is subsequently implemented as a new initial guess for the solving procedure of the Boltzmann equation. This procedure is repeated until the values of  $dn_e/dt$  converge to a predefined level.

### B.3 Parallel resistor model of a gas discharge

Using the above described kinetic model the behaviour of the discharge is calculated according to the parallel resistor model [2–4]. In this model the discharge is divided into a number of parallel layers, along the optical axis and transverse to the electrodes, see figure B.1.

For each layer a different set of initial conditions may be chosen, such as the initial electron density, corresponding to a fluctuation in the pre-ionisation density, or a different electric fields to account for the shape or the alignment of the electrodes [3].

During the calculation the properties of all layers are assumed to be uniform within each layer and the exchange of particles and energy between different layers is neglected by taking the layers thicker than the electron diffusion length. In order to be able to observe Large Spatial Scale Non-uniformities (LSSNs) the number of layers has to be high enough. In the model a number of 20 layers is used.

The electric field strength in each layer is calculated from the applied voltage and the average interelectrode separation across the layer thickness. Since in the experimental set-up the cathode is profiled while the anode is flat, the interelectrode distance

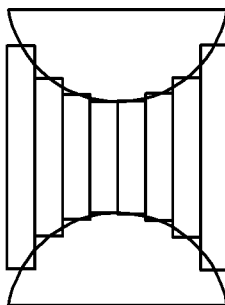


*Figure B.1: Schematic drawing of the parallel resistor model. The discharge is divided into several parallel layers which are oriented along the optical axis (transversal to the plane of the page) and transverse to the electrodes. Each layer can be assigned specific initial values. The model equations are solved for each layer concurrently.*

increases from the centre of discharge outwards, leading to a decrease in the electric field strength from one layer to another.

The electric currents through each layer are combined in the description of the electrical behaviour of the electric circuit, controlling the relation between the total discharge current and the discharge voltage.

## B.4 Rate equations

The reactions taken into account in the modelling are given in tables B.1 and B.2. In table B.1 the considered reactions are shown for which the rate coefficients are determined by solving the Boltzmann equation. In table B.2 the considered rate equations are shown for which the rate constants were taken from literature.

Reaction
$\text{Ar} + e \rightarrow \text{Ar}^+ + e + e$
$\text{Ar} + e \rightarrow \text{Ar}^* + e$
$\text{Ar} + e \rightarrow \text{Ar}^{**} + e$
$\text{Ar}^* + e \rightarrow \text{Ar}^{**} + e$
$\text{Ar}^* + e \rightarrow \text{Ar}^+ + e + e$
$\text{Ar}^{**} + e \rightarrow \text{Ar}^+ + e + e$
$\text{Ar}_2^+ + e \rightarrow \text{Ar}^{**} + \text{Ar}$
$\text{F}_2 + e \rightarrow \text{F}^- + \text{F}$
$\text{F}_2^{vib} + e \rightarrow \text{F}^- + \text{F}$
$\text{F}_2 + e \rightarrow \text{F}_2^{vib} + e$
$\text{He} + e \rightarrow \text{He}^+ + e + e$
$\text{He} + e \rightarrow \text{He}^* + e$
$\text{He} + e \rightarrow \text{He}^{**} + e$
$\text{He}^* + e \rightarrow \text{He}^{**} + e$
$\text{He}^* + e \rightarrow \text{He}^+ + e + e$
$\text{He}^{**} + e \rightarrow \text{He}^+ + e + e$
$\text{He}_2^+ + e \rightarrow \text{He}^{**} + \text{He}$

Table B.1: The rate equations governed by the discharge. The rate coefficients are derived from solving the Boltzmann equation. Taken from Demyanov et al., ref. [5].

Reaction	Rate ( $\cdot 10^X$ )	Ref.
$\text{He}^+ + \text{He} + \text{He} \rightarrow \text{He}_2^+ + \text{He}$	1.0 (-31)	[6]
$\text{Ar}^+ + \text{Ar} + \text{Ar} \rightarrow \text{Ar}_2^+ + \text{Ar}$	2.5 (-31)	[7]
$\text{Ar}^+ + \text{Ar} + \text{He} \rightarrow \text{Ar}_2^+ + \text{He}$	1.0 (-32)	[8]
$\text{Ar}^* + \text{F}_2 \rightarrow \text{ArF}^* + \text{F}$	4.0 (-10)	[9]
$\text{Ar}^+ + \text{F}^- \rightarrow \text{ArF}^*$	9.1 (-7)	[10]
$\text{Ar}_2^+ + \text{F}^- \rightarrow \text{ArF}^* + \text{Ar}$	9.26 (-7)	[10]
$\text{He}^+ + \text{F}^- \rightarrow \text{F}^* + \text{He}$	6.94 (-6)	[10]
$\text{He}_2^+ + \text{F}^- \rightarrow \text{F}^* + \text{He} + \text{He}$	5.08 (-6)	[10]
$\text{Ar}^{**} \rightarrow \text{Ar}^* + \text{Phot}$	1.4 (+7)	[11]
$\text{He}^{**} \rightarrow \text{He}^* + \text{Phot}$	1.0 (+8)	Estimate
$\text{ArF}^* \rightarrow \text{Ar} + \text{F} + h\nu$	2.38 (+8)	[12]
$\text{ArF}^* + \text{Rad} \rightarrow \text{Ar} + \text{F} + \text{Rad}$	2.7 (-16)	[12]
$\text{Ar}^{**} + \text{Rad} \rightarrow \text{Ar}^+ + \text{e}$	3.0 (-18)	[13]
$\text{F}_2 + \text{Rad} \rightarrow \text{F} + \text{F}$	1.5 (-21)	[13]
$\text{F}^- + \text{Rad} \rightarrow \text{F} + \text{e}$	9.7 (-18)	[14]
$\text{Ar}_2\text{F}^* + \text{Rad} \rightarrow \text{ArF}^* + \text{Ar}$	1.0 (-18)	[15]
$\text{Ar}_2^* + \text{Rad} \rightarrow \text{Ar}_2^+ + \text{e}$	4.0 (-18)	[14]
$\text{ArF}^* + \text{e} \rightarrow \text{Ar} + \text{F} + \text{e}$	2.0 (-7)	[14]
$\text{ArF}^* + \text{F}_2 \rightarrow \text{Ar} + \text{F} + \text{F} + \text{F}$	1.900 (-9)	[14]
$\text{ArF}^* + \text{Ar} \rightarrow \text{Ar} + \text{Ar} + \text{F}$	9.000 (-12)	[14]
$\text{ArF}^* + \text{He} \rightarrow \text{He} + \text{Ar} + \text{F}$	1.000 (-12)	[15]
$\text{ArF}^* + \text{He} + \text{Ar} \rightarrow \text{Ar}_2\text{F}^* + \text{He}$	1.000 (-31)	[15]
$\text{Ar}^* + \text{Ar}^* \rightarrow \text{Ar}^+ + \text{e} + \text{Ar}$	5.000 (-10)	[14]
$\text{Ar}_2\text{F}^* + \text{He} \rightarrow \text{Ar} + \text{Ar} + \text{F} + \text{He}$	1.000 (-12)	[14]
$\text{Ar}^* + \text{Ar} + \text{Ar} \rightarrow \text{Ar}_2^* + \text{Ar}$	2.500 (-32)	[16]
$\text{Ar}^* + \text{Ar} + \text{He} \rightarrow \text{Ar}_2^* + \text{He}$	8.000 (-33)	Estimate
$\text{Ar}_2^* \rightarrow \text{Ar} + \text{Ar}$	2.380 (+8)	[16]
$\text{F}^* \rightarrow \text{F} + \text{Phot}$	2.700 (+8)	Estimate

Table B.2: The rate equations and rate coefficients used in the numerical model. The rate constants are taken from the literature. The rate coefficients are stated in units of  $\text{cm}^3/\text{s}$ ,  $\text{cm}^6/\text{s}$  or  $\text{s}^{-1}$ . Rad: Radiation field at  $\lambda = 193 \text{ nm}$ . Phot: Photon at a different wavelength than  $\lambda = 193 \text{ nm}$ . Taken from Demyanov et al., ref. [5].



## References

- [1] **A.V. Demyanov**, Private communication.
- [2] **T. Fischer**, *Ortsaufgelöste Untersuchungen zur Stabilität von KrF<sup>\*</sup>-Laserentladungen*, PhD thesis, Technische Hochschule Darmstadt, Darmstadt, Germany (1992). (In German).
- [3] **M.J. Kushner**, *Microarcs as a termination mechanism of optical pulses in electric-discharge-excited KrF excimer lasers*, IEEE Tr. Plasma Sci. **19** (2), 387–399 (1991).
- [4] **A.V. Dem'yanov**, **I.V. Kotchetov**, **A.P. Napartovich**, **S. Longo** and **M. Capitelli**, *Theoretical studies on microscopic and macroscopic nonuniformities in electric-discharge-excited XeCl lasers*, Plasma Chem. and Plasma Proc. **16** (1), 121–140 (1996).
- [5] **A.V. Demyanov**, **L. Feenstra**, **P.J.M. Peters**, **A.P. Napartovich** and **W.J. Witteman**, *Kinetic modelling of a discharge pumped ArF excimer laser*. Submitted to Journal of Physics D: Applied Physics.
- [6] **E.C. Beaty** and **P.L. Peterson**, Phys. Rev. **137**, A364 (1965).
- [7] **D. Smith** and **P.R. Cromey**, J. Phys. B **1**, 638 (1968).
- [8] **D.K. Bohme**, **D.B. Dunkin**, **F.C. Fehsenfeld** and **E.E. Ferguson**, *Flowing afterglow studies of ion-molecule association reactions*, J. Chem. Phys. **51** (3), 863–872 (1969).
- [9] **J.H. Kolts** and **D.W. Setser**, *Rate constants for ArF<sup>\*</sup> formation from reactions of Ar (<sup>3</sup>P<sub>2</sub>) with fluorine containing molecules and the pressure dependence of the C to B state ratios for ArF<sup>\*</sup>, KrF<sup>\*</sup>, and XeF<sup>\*</sup>*, J.Phys. Chem. **82** (15), 1766–1768 (1978).
- [10] **A.V. Demyanov**. Calculated using the equations of Flannery and Yang, ref. [17].
- [11] **J.W. Keto** and **Ch.Yu. Kuo**, *Cascade production of Ar(3p <sup>5</sup>4p) following electron bombardment*, J. Chem. Phys. **74** (11), 6188–96 (1981).
- [12] **M. Ohwa** and **M. Obara**, *Theoretical evaluation of the buffergas effects for a self-sustained discharge ArF laser*, J. Appl. Phys. **63** (5), 1306–1312 (1988).
- [13] **S. Nagai**, **M. Sakai**, **H. Furuhashi**, **A. Kono**, **T. Goto** and **Y. Uchida**, *Effects of F<sup>-</sup> ions and F<sub>2</sub> molecules on the oscillation process of a discharge-pumped ArF excimer laser*, IEEE J. Quantum Electron. **34** (1), 40–46 (1998).
- [14] **D. Lo**, **A.I. Shchedrin** and **A.V. Ryabtsev**, *The upper energy limit of a self-sustained discharge-pumped ArF laser*, J. Phys. D: Appl. Phys. **29**, 43–49 (1996).
- [15] **A.M. Boïchenko**, **V.I. Derzhiev**, **A.G. Zhidkov** and **S.I. Yakovlenko**, *Kinetic model of an ArF laser*, Sov. J. Quantum Electron. **22** (5), 444–448 (1992). [Kvantovaya Elektron. **19**, 486–491 (1992)].

- [16] **Ch.A. Brau**, *Rare gas halogen excimers*, In: Excimer lasers, Ch.K. Rhodes, ed., Topics in applied physics **30**, ch. 4, 87–137, Springer Verlag, Berlin, 2nd enlarged edition, (1984).
- [17] **M.R. Flannery and T.P. Yang**, *Ionic recombination of rare-gas atomic ions  $X^+$  with  $F^-$  in a dense gas X*, Appl. Phys. Lett. **32** (5), 327–329 (1978).

# Summary

The goal of our research is the realisation of a gas discharge pumped argon-fluoride laser with a long pulse length ( $\tau_{\text{pulse}} \gtrsim 100$  ns) with a high pulse energy ( $E_{\text{pulse}} \gtrsim 100$  ns), preferably capable of operating at a high pulse repetition rate (Rep.Rate up to 1 kHz). The wavelength of this laser is  $\lambda = 193$  nm, deep ultra violet. Applications of this laser are nano-lithography and applications of a bio-physical nature such as surgery and the in vivo study of bacteria.

In comparison with short-pulse lasers ( $\tau_{\text{pulse}} \lesssim 20$  ns) long pulses are much more efficient, because applications such as cutting and drilling go faster and because the lower peak power of the pulse, at the same total pulse energy, reduces the damaging of optics. In principle long pulse lasers may be operated also at a higher energy efficiency than short pulse lasers.

The studied laser operates by an electric discharge in a gas mixture. The discharge must be homogeneous throughout the discharge volume ( $\text{Vol}_{\text{disch}} \sim 100 \text{ cm}^3$ ) in order to obtain laser operation. This means that the discharge should not break down into separate arcs.

The laser gas mixture consists of a few percents of fluorine and argon in helium and/or neon at a total pressure of several bar. Gas discharges in mixtures containing fluorine are less stable than in gas mixtures without fluorine. The scientific side of this thesis is therefore to study the discharge stability as required for a good laser performance. This has resulted in a better understanding and new concepts. The engineering side is to develop the technology to fulfil as good as possible the theoretical requirements. The realised set-ups have shown a much longer discharge stability and a much better laser performance than reported before.

During the research several electric circuits have been designed and tested to pump the gas discharge. The results show that the operation characteristics of the ArF laser

primarily depend on the stability of the gas discharge, specifically on the homogeneity of the pre-ionisation and the connected starting quality of the discharge. The more homogeneous and stable the discharge is, the longer is the maximum available laser pulse length. The starting quality of the discharge is determined by the height and the rise time of the applied voltage pulse and by the rise time of the current in the very first moments after the discharge is ignited. However, after the starting of the discharge its stability is mainly dependent on the fluorine concentration of the gas mixture. The higher the fluorine concentration is, the faster the discharge deteriorates into arcs.

The ArF laser has been studied in two ‘regimes’:

1. A regime with ‘regular’ fluorine and argon concentrations ( $[F_2] = 0.15\%$ ,  $[Ar] = 2.50\%$ ), helium as the buffer gas (at a total gas pressure of  $P_{tot} = 4$  bar) and high charging voltages ( $V_{charge} \sim 30$  kV).  
This results in short pulses ( $\tau_{pulse} \sim 25$  ns) and high specific output energies ( $E_{out} \sim 1.9$  J/ℓ).
2. A regime with low fluorine and argon concentrations ( $[F_2] \sim 0.02\%$ ,  $[Ar] \sim 1.00\%$ ), neon as the buffer gas (at a total gas pressure of  $P_{tot} = 5$  bar) and low charging voltages ( $V_{charge} \sim 7.5$  kV).  
This results in the sought-after long pulses ( $\tau_{pulse}$  up to  $\sim 120$  ns) and low specific output energies ( $E_{out} \sim 20$  mJ/ℓ).

*Ad 1:* The different electric circuits have been tested under identical circumstances in order to investigate the results of differently shaped voltage pulses for the excitation of the gas mixture.

It appears that the combination of the pre-ionisation timing and the shape of the voltage pulse has a large influence on the performance of the laser. Variations of a few ns in the timing of the pre-ionisation pulse with respect to the voltage pulse can cause differences of tens of percents in the output energy and the pulse length of the laser. The explanation for this effect is found in the way the pre-ionisation electron density is multiplied to that of the discharge breakdown. The optimum laser performance is obtained when the polarity of the voltage across the electrodes is reversed during the electron density multiplication, but prior to the discharge breakdown.

The reduction of the self-inductance of the peaking circuit, resulting in an increase of the applied input power in the very first moments of the discharge, turns out to be of a crucial importance for the generation of high output powers and long laser pulses. The laser performance is increased by using neon as the buffer gas instead of

helium, which is mainly due to the higher discharge stability of the neon-buffered gas discharge.

*Ad 2:* The laser performance has been studied parametrically with respect to the pre-ionisation timing, the input power and the composition and the total pressure of the gas mixture.

The optimum gas composition with respect to the output power of the laser turns out to be 1 mbar F<sub>2</sub>, 50 mbar Ar in the buffer gas Ne at a total gas pressure of  $P_{\text{tot}} = 4.5$  bar. This gas mixture is similar to the optimum gas mixture of the well-known long pulse XeCl excimer laser. The laser pulse length increases rapidly with a decreasing concentration of the active ingredients, fluorine and argon, in the gas mixture. The difference in the optimum conditions with respect to the pulse length and the output energy is caused by a trade-off between the laser gain and the discharge stability.

The laser performance is less sensitive to variations of the pre-ionisation timing than in the short pulse regime, probably because of the lower fluorine concentration and a higher pre-ionisation electron density. Both the output energy and the pulse length increase when the input power is raised, although the output energy seems to saturate at high input powers.

The present studies have been evaluated in view of the next generation ArF excimer lasers. In addition to several considerations for constructing gas discharge pumped excimer lasers the relevant parameters for the optimisation of the discharge quality and of the laser have been found.



# Samenvatting

Het doel van het onderzoek is de realisatie van een gasontladings-gepompte argon-fluoride laser met een lange puls ( $\tau_{\text{puls}} \gtrsim 100$  ns) en met een hoog vermogen ( $E_{\text{puls}} \gtrsim 100$  mJ), bij voorkeur geschikt voor hoge puls-herhalingsfrequenties (Rep.Rate tot 1 kHz). De golflengte van deze laser is  $\lambda = 193$  nm, diep ultra violet. Doelstellingen voor het gebruik van deze laser liggen in de nano-lithografie en in biofysische bewerkingen, onder andere chirurgie en het onderzoek aan bacteriën in vivo.

Vergeleken met de huidige korte-pulslasers ( $\tau_{\text{puls}} \sim 20$  ns) zijn lange laserpulsen voor veel bewerkingen efficiënter doordat bewerkingen sneller blijken te kunnen worden uitgevoerd en omdat een lager piekvermogen van de puls de kans op beschadiging van de gebruikte optiek vermindert. In principe kan een lange-pulslaser ook worden bedreven met een hoger energetisch rendement dan een korte-pulslaser.

De bestudeerde laser werkt door middel van een elektrische ontlading in een gasmengsel. Om laserwerking te kunnen vertonen moet de ontlading homogeen zijn in het gehele ontladingsvolume (ca.  $100 \text{ cm}^3$ ), dat wil zeggen: de ontlading mag niet ontaarden in afzonderlijke vonken.

Het gasmengsel bestaat uit een paar procent fluor en argon in helium en/of neon bij een totaaldruk van een paar bar. In fluor-bevattende gasmengsels kunnen ontladingen minder lang homogeen gehouden worden dan in een gasmengsel zonder fluor. Het wetenschappelijke karakter van het onderzoek is daarom het bestuderen van de ontladingsstabiliteit in relatie tot de laserwerking. De resultaten hiervan zijn een beter begrip en nieuwe concepten. De technische kant van het onderzoek is gelegen in de ontwikkeling van technologieën die zo goed mogelijk aan de theoretische eisen voldoen. De gebouwde opstellingen hebben geresulteerd in een veel langere ontladingsstabiliteit en een betere laserwerking dan voorheen beschreven.

Tijdens het onderzoek zijn verschillende elektrische circuits ontworpen en getest voor

het pompen van de ontlading. De resultaten tonen aan dat de werking van de ArF laser primair afhankelijk is van de stabiliteit van de gasontlading; met name de homogeniteit van de voorionisatie en de daarmee samenhangende startkwaliteit van de ontlading. Hoe homogener en stabielere de ontlading is, des te langer de laserpuls kan zijn. De startkwaliteit van de ontlading wordt enerzijds bepaald door de hoogte en de stijgtijd van de aangelegde spanningspuls en anderzijds door de stijgtijd van de stroom direct na de ontsteking van het gas. Echter, na de ontsteking van de ontlading is de ontladingsstabiliteit vooral afhankelijk van de fluorconcentratie in het gas. Hoe hoger de fluorconcentratie is, des te sneller de ontlading tot vonken desintegreert.

De ArF laser is in twee ‘gebieden’ bestudeerd:

1. Een gebied met een ‘gebruikelijke’ fluor- en argon concentratie ( $[F_2] = 0.15 \%$ ,  $[Ar] = 2.50 \%$ ), helium als buffergas (bij een totale gasdruk van  $P_{tot} = 4$  bar) en laadspanningen van  $\sim 30$  kV.  
Dit resulteert in korte pulsen ( $\tau_{puls} \sim 25$  ns FWHM) en hoge soortelijke energieopbrengsten ( $E_{out} \sim 1.9$  J/ $\ell$ ).
2. Een gebied met een zeer lage fluor- en argonconcentratie ( $[F_2] \sim 0.02 \%$ ,  $[Ar] \sim 1.00 \%$ ), neon als buffergas (bij een totale gasdruk van  $P_{tot} = 5$  bar) en laadspanningen van  $\sim 5$  kV.  
Hierbij zijn de gewenste zeer lange laser pulsen ( $\tau_{puls}$  tot  $\sim 120$  ns FWHM) gerealiseerd. De soortelijke energieopbrengsten liggen rond ( $E_{out} \sim 20$  mJ/ $\ell$ ).

*Ad 1:* De verschillende circuits zijn getest onder gelijke omstandigheden zodat de resultaten van de verschillende spanningspulsvormen voor het pompen van de gasontlading met elkaar vergeleken konden worden.

Het blijkt dat de combinatie van de voorionisatie-timing en de spanningsvorm een grote invloed heeft op het gedrag van de laser. Variaties in de timing van de voorionisatie van enkele ns kunnen verschillen van tientallen procenten in de pulsenergie en de pulslengte veroorzaken. De verklaring hiervoor ligt in de manier waarop de electronendichtheid van de voorionisatie wordt vermenigvuldigd tot de ontladingsstart. De optimale output blijkt te worden gegenereerd wanneer de polariteit van de spanning over de elektroden omkeert tijdens de vermenigvuldiging van de electronendichtheid, maar voordat de ontlading start.

Het verlagen van de zelfinductie van het peaking circuit, zodat het initiële pompvermogen wordt verhoogd, blijkt van cruciaal belang te zijn voor het genereren van hoge vermogens en lange laserpulsen. Zowel de pulslengte als de outputenergie van de laser



---

worden verbeterd door het gebruik van neon als buffergas, in plaats van helium. Dit is voornamelijk het gevolg van een hogere stabiliteit van de ontlading met neon.

*Ad 2:* Het gedrag van de laser is parametrisch bestudeerd met betrekking tot de voorionisatie-timing, het aangelegde pompvermogen, de gassamenstelling en de totale gasdruk.

In het onderzoek naar het effect van de gassamenstelling blijkt een -voor de output-optimale gassamenstelling voor onze opstelling van 1 mbar  $F_2$  en 50 mbar Ar in 4.5 bar Ne. Dit gasmengsel ligt dicht bij het optimale recept voor de welbekende lange-puls XeCl excimeer lasers. De laserpulslengete neemt snel toe wanneer de concentratie actieve ingrediënten ( $F_2$  en Ar) in het gas afneemt. Het verschil in de optimale condities voor de pulslengte en de energieopbrengst van de laser wordt veroorzaakt door een negatieve correlatie tussen de lasergain en de ontladingsstabiliteit.

Het gedrag van de laser is minder sterk afhankelijk van de timing van de voorionisatie dan in het korte-pulsregime, waarschijnlijk door de lagere fluorconcentratie en een hogere voorionisatie-electronendichtheid. Zowel de pulslengte als de energieopbrengst nemen toe wanneer het pompvermogen wordt vergroot, hoewel de energieopbrengst lijkt te vezadigen bij hoge pompvermogens.

Het onderzoek is geëvalueerd met het oog op de volgende generatie ArF excimeer lasers. Naast enkele zaken die betrekking hebben op de constructie van gasontladingsgepompte excimeerlasers zijn de relevante parameters voor de optimalisatie van de ontladingskwaliteit en van de laser zelf gevonden.



# Curriculum vitae

van Louw Feenstra,  
geboren op 2 december 1970 te Groningen.

In 1989 behaalde hij het eindexamen aan het Stedelijk Gymnasium Haarlem en begon hij met de studie Natuurkunde aan de Rijksuniversiteit Leiden. Zijn afstudeeronderzoek begon in oktober 1993 bij de werkgroep Quantum Vloeistoffen I, onder leiding van prof. dr R. de Bruyn Ouboter aan het Kamerlingh Onnes Laboratorium. Onder leiding van drs M.C. Koops werd onderzoek verricht aan de superstroom-fase relaties en stroom-spanning karakteristieken van supergeleidende puntcontacten van atomaire afmetingen met behulp van de zogenaamde ‘Mechanically Controllable Break-junction’ (MCB) techniek. In april 1995 studeerde hij af op dit onderwerp.

Aansluitend trad hij in dienst van de Stichting voor de Technische Wetenschappen (STW) om als Onderzoeker in Opleiding zijn promotieonderzoek te verrichten bij de vakgroep Quantum Electronica van de faculteit Technische Natuurkunde van de Universiteit Twente, onder leiding van prof. dr ir W.J. Witteman en dr P.J.M. Peters. De resultaten van dat onderzoek vormen de basis van dit proefschrift.

Naast zijn promotieonderzoek assisteerde hij bij practica voor 1e jaars studenten Technische Natuurkunde en werd er door hem een 3e-jaars student Vliegtuigbouwkunde van de Technische Universiteit Delft begeleid bij zijn stage (die een groot deel van het materiaal voor hoofdstuk 5 van dit proefschrift opleverde).

Na zijn promotie zal hij als post-doc onderzoeker in dienst treden van de Stichting voor Fundamenteel Onderzoek der Materie (FOM) om onderzoek te verrichten aan lithografie met metastabiele He-atomen bij de vakgroep Atoom- en Laserfysica van de Vrije Universiteit Amsterdam onder leiding van prof. dr W. Hogervorst.



# List of publications

1. **M.C. Kooops, L. Feenstra, B.J. Vleeming, A.N. Omelyanchouk and R. de Bruyn Ouboter**, *The current-phase relation of a mechanically controllable breakjunction*, *Physica B* **218** (1-4), 145-147 (1996).
2. **L. Feenstra, O.B. Hoekstra, P.J.M. Peters and W.J. Witteman**, *An X-ray preionised discharge pumped ArF-laser*, in: Proceedings 1997 IEEE/LEOS Symposium Benelux Chapter, F. Karouta, J.E.M. Haverkort, J. Kennis and A.P. Peeters, eds., Technology Foundation STW, Utrecht, The Netherlands, 161-164 (1997).
3. **L. Feenstra, O.B. Hoekstra, P.J.M. Peters and W.J. Witteman**, *On the timing of the X-ray preionisation of a discharge pumped ArF excimer laser with different excitation circuits*, in: XII International Symposium on Gas Flow and Chemical Lasers and High-Power Laser Conference, A.S. Boreisho and G.A. Baranov, Eds, Proceedings of SPIE **3574**, 67-73 (1998).
4. **L. Feenstra, O.B. Hoekstra, P.J.M. Peters and W.J. Witteman**, *On the performance of an ArF and a KrF laser as a function of the preionisation timing and the excitation mode*, *Applied Physics B: Lasers and Optics*, in print.
5. **L. Feenstra, H.M.J. Bastiaens, P.J.M. Peters and W.J. Witteman**, *On the long pulse operation of an X-ray preionized, gas discharge pumped ArF excimer laser*, *Applied Physics Letters*, in print.
6. **L. Feenstra, H.M.J. Bastiaens, P.J.M. Peters and W.J. Witteman**, *On the extension of the pulse length of a discharge excited ArF excimer laser*, *Laser Physics*, in print.
7. **L. Feenstra, H.M.J. Bastiaens, P.J.M. Peters and W.J. Witteman**, *A long pulse discharge excited ArF laser*, Submitted to: IEEE Journal of Selected Topics in Quantum Electronics on Short Wavelength Lasers and Applications.
8. **A.V. Demyanov, L. Feenstra, P.J.M. Peters A.P. Napartovich and W.J. Witteman**, *Modelling of a discharge excited ArF excimer laser*, Submitted to: Journal of Physics D: Applied Physics.



## Errata

in the thesis

### On the long pulse operation of a discharge pumped ArF excimer laser

of

Louw Feenstra

P.94-96, Figs.6.4-6.6: The legends should read:  $\cdots\cdots$   $I_{\text{laser}}$   $\text{---}$   $V_{\text{p}}$   $\text{---}$   $I_{\text{main}}$   
 $\cdots\cdots$   $V_{\text{x}}$

P.99, Par.2, Ln.2-5: "Assuming ... results." Replace "reduction" with "increase" and  
" $\Delta E_{\text{fil}}/E_{\text{bulk}} = 0.8 \%$ " with " $\Delta E_{\text{fil}}/E_{\text{bulk}} = 0.7 \%$ "

P.106, Item  $P_{\text{calc}}$ E: Remove the sentence: "Note the different ..."

P.144, Ln.1 below Eq.B.3: Replace definitions of  $R_f$  and  $R_r$  with  $R_f = k_f \prod_i [X_i] \nu_i$   
and  $R_r = k_r \prod_i [X_i] \nu_i$